UNIVERSITÀ
degli STUDI
di CATANIA

Dipartimento
di Fisica
e Astronomia
"Ettore Majorana"

PhD programme in physics

Salvatore Calabrese

The ^{116}Cd(^{20}Ne, ^{20}O)^{116}Sn Double Charge Exchange reaction mechanism at 15.3 AMeV addressed by a multiple channel approach in the context of the NUMEN project

PhD thesis

Supervisor:
Chiar.mo Prof. Francesco Cappuzzello

---

academic year 2018/2019

PhD Fellowship funded by
Laboratori Nazionali del Sud
Istituto Nazionale di Fisica Nucleare

Research project developed within the NUMEN collaboration

Co-Advisors:
Dr. Diana Carbone
Dr. Manuela Cavallaro

Contents

List of Figures

Introduction

Neutrinoless double beta decay is a fascinating process, proposed eighty years ago but still not observed, which could be related to many outstanding issues of modern Physics such as the Dirac or Majorana nature of neutrinos as well as their absolute mass values. Due to such important implications, a prodigious activity is already in progress in the attempt to detect the first of such events. From the theoretical point of view, many different scenarios have been proposed and can be adopted to make deduction on the neutrino properties. Although the models are very different one to each other, all rely on the same quantity for their predictions, the Nuclear Matrix Elements (NME) of the process. The latter can be calculated adopting different theoretical nuclear structure models which however return not fully consistent results, thus representing the major uncertainty in the description of the neutrinoless double beta decay.
In Chapter 1, the neutrinoless double beta decay NME and the limits of the calculations are presented and discussed.
In Chapter 2, some example of the experimental nuclear tools useful to constrain the NME theoretical results are discussed, with particular reference to the Charge Exchange nuclear reactions. In fact, under specific experimental conditions, Single Charge Exchange reactions present an established connection with the weak NME of single beta decay. However, moving to double beta processes and in particular considering the neutrinoless double beta decay, closer similarities emerge with the heavy-ion Double Charge Exchange reactions. The latter are rare and poorly understood nuclear processes, challenging from both experimental and

theoretical side. A systematic study of their properties and the possible connection with neutrinoless double beta decay represent the main goals of the NUMEN project. In the present Thesis, the (^{20}Ne,^{20}O) Double Charge Exchange reaction at 306 MeV on the neutrinoless double beta decay candidate nucleus ^{116}Cd is investigated along with the competitive reaction channels.
In Chapter 3, the set-up arranged for the experiment and the MAGNEX spectrometer are described. The latter, implementing specific software and hardware solutions, guarantees high performance resulting effective even in measurements characterized by very low yields like the Double Charge Exchange one. Moreover, due to its large acceptance in momentum, it allows to simultaneously detect the competing Single Charge Exchange and nucleon transfer reaction channels.
In Chapter 4, the experimental analysis of all the measured reaction channels is presented. The differential cross section distributions in energy are deduced for the Double Charge Exchange, Single Charge Exchange, One-Proton Transfer and Two-Proton Transfer. The angular distributions of selected single and multiple transitions are also extracted. A sensitivity study of the MAGNEX spectrometer is conceived for the first time and applied to the Double Charge Exchange reaction data. Such analysis confirms the high significance of the extracted experimental results since the estimated signal to noise ratio results remarkable high.
In Chapter 5, the One- and Two-nucleon transfer differential cross sections are theoretically investigated within Distorted Wave Born Approximation, Coupled Channel Born Approximation and Coupled Reaction Channels frameworks. The satisfying results obtained for the measured reaction channels have paved the way to a systematic investigations of the complete transfer paths in competition with Single and Double Charge Exchange channels. The results reported indicate a small contributions to the Single Charge Exchange channel and a negligible one for the Double Charge Exchange reaction.

Chapter 1

Double Beta Decay

Nuclear double beta decays represents a crucial topic in modern Physics, being able to open new possible scenarios beyond the Standard Model (SM). In the past years, in fact, neutrino oscillation experiments have proved that neutrino flavors mix each verifying that they have finite masses unlike the SM predictions. On the other hand, such experiments did not settle all aspects of the neutrino matter, leaving unsolved the question about the Dirac or Majorana nature of such particles and their mass absolute values.
Nowadays, it is common ground that the most promising process to address such points is represented by the neutrinoless double-beta ($0\nu\beta\beta$) decay. Its discovery would establish their Majorana particle nature providing additional information on the neutrino mass scale and ordering. Moreover, $0\nu\beta\beta$ observation would be of the utmost importance for many others Physics sectors. First of all, it would show the existence of a process violating the conservation of the total lepton and thus the baryon$-$lepton number which represent a fundamental symmetry of the SM. In addiction, it would open the way to many other possible scenarios. The see-saw mechanism to name but one - which predicts the existence of Majorana neutrinos - would offer a solution to the intriguing problem of the smallness of neutrino masses also providing an explanation for one of the biggest cosmological puzzle, the observed matter-antimatter asymmetry of the Universe via the leptogenesis mechanism.

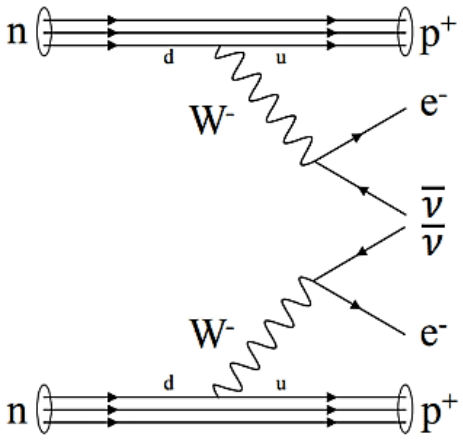

Figure 1.1: Feynman diagrams for $2\nu\beta^-\beta^-$ decay

All these fundamental implications justify the worldwide prodigious activities in the search of experimental evidences and theoretical underpinning of the process.

1.1 $2\nu\beta\beta$ and $0\nu\beta\beta$

The two-neutrino double-beta ($2\nu\beta\beta$) decay mode is a rare known nuclear process. Described by Maria Goeppert-Mayer in 1935 [1], it is a transition between isobaric nuclei in which, considering the $\beta^-\beta^-$ mode, two neutrons simultaneously decay into protons emitting two electrons and two (anti)neutrinos

$$(A, Z) \rightarrow (A, Z+2) + 2e^- + 2\bar{\nu} \tag{1.1}$$

see Fig. 1.1 for its corresponding Feynman diagram. Such transitions are extremely rare decays, observable only in those isotopes in which single beta decay is energetically forbidden. In fact, in principle a nucleus (A, Z) can undergo a double beta decay as long as the nucleus (A, Z + 2) is lighter. However, if it can also decay by single beta decay, (A, Z + 1), the branching ratio for the $\beta\beta$ will be too difficult to be observed due to the overwhelming background rate from the single beta process. Therefore, candidate isotopes for detecting the $\beta\beta$ are even-even nuclei that, due to

the nuclear pairing force, are lighter than the odd-odd (A, Z + 1) nucleus, making single beta decay kinematically forbidden. Nuclei satisfying such conditions are only few tens. Being a second-order weak-interaction process, it is strongly suppressed and at the moment it has been observed in 11 atomic nuclei with typical half-lives ranging from 10^{18} to 10^{24} yr [2]. It is worth noting that, since the $\beta\beta$ candidates are even-even systems, it follows immediately that their grounds state (g.s.) spin is always zero and thus transitions $0^+ \rightarrow 0^+$ are expected in all cases. In particular, Fermi-type transition contributes only through mixing of high-lying 0^+ isobaric analogue states, so that it is generally very small and thus it is sufficient to retain Gamow-Teller transitions. The intermediate states are, therefore, limited to 1^+ which thus play a particularly important role in $2\nu\beta\beta$. The final state can be 0^+, 1^+, 2^+ but the decay rates towards 1^+ and 2^+ as well as transition to a 0^+ excited states are expected to be kinematically suppressed [3]. Such reason justifies the main interest for $0^+_{gs} \rightarrow 0^+_{gs}$ transitions even if recent evidences [4] revealed some interesting exceptions.
The idea of neutrinoless double-beta decay mode was introduced by Wendell Furry in 1939 [5] as a transition between isobaric nuclei in which two neutrons simultaneously decay into protons without neutrinos emission. Considering the $0\nu\beta^-\beta^-$ mode[1], it can be expressed as

$$(A, Z) \rightarrow (A, Z + 2) + 2e^- \tag{1.2}$$

As for $2\nu\beta\beta$ also $0\nu\beta\beta$ could be observed if single β decay is prohibited. Despite there are 35 isotopes in nature fulfilling such requirement, realistically only nine of them emerge as interesting candidates - realizing the best compromises between natural abundance, reasonably priced enrichment, Q-values and phase-space factors - and are under investigation in competitive experiments: ^{48}Ca, ^{76}Ge, ^{82}Se, ^{96}Zr, ^{100}Mo, ^{116}Cd, ^{130}Te, ^{136}Xe and ^{150}Nd (see Tab 1.1).

To describe such phenomenon several possible mechanisms have been proposed [16]. However, it was proven that, whatever mechanism is responsible for $0\nu\beta\beta$ decay, it would provide a model-independent proof that neutrinos are Majorana fermions [17]. Among the proposed ones the

[1]The other various mass modes of neutrinoless double beta decays - the positron emission together with electron capture ($0\nu\beta^+EC$ decay) and the double electron capture ($0\nu ECEC$ decay) - will not be explored in the present discussions.

Table 1.1: Non-exhaustive list of past and present $0\nu\beta\beta$ searching experiments distinguished for isotopes and sorted by mass number. Their best present limits on $0\nu\beta\beta$ decay rate ($T^{0\nu}_{1/2}$) at 90% confidence limit are reported. The corresponding $m_{\beta\beta}$ values are calculated adopting the most update NME [6].

Isotope	Experiment	Location	$T^{0\nu}_{1/2}$	$m_{\beta\beta}$
^{48}Ca	CANDLES [7]	Japan	>6.2×10^{22} yr	<3.1-15.4 eV
^{76}Ge	GERDA [8]	Italy	>5.8×10^{25} yr	<0.14-0.37 eV
^{82}Se	CUPID-0 [9]	Italy	>2.4×10^{24} yr	<0.4-0.8 eV
^{96}Zr	NEMO-3 [10]	France	>9.2×10^{21} yr	<3.6-10.4 eV
^{100}Mo	NEMO-3 [11]	France	>1.1×10^{24} yr	<0.33-0.62 eV
^{116}Cd	AURORA [12]	Italy	>2.2×10^{23} yr	<1.0-1.7 eV
^{130}Te	CUORE [13]	Italy	>1.5×10^{25} yr	<0.11-0.52 eV
^{136}Xe	KamLAND-Zen [14]	Japan	>5.6×10^{25} yr	<0.08-0.23 eV
^{150}Nd	NEMO-3 [15]	France	>2.0×10^{22} yr	<1.6-5.3 eV

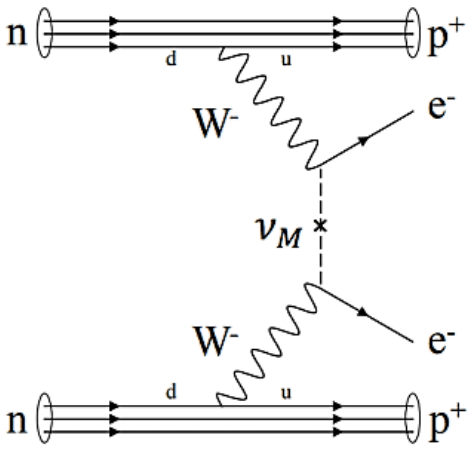

Figure 1.2: Feynman diagrams for $0\nu\beta^-\beta^-$ decay mediated by light Majorana neutrino ν_M exchange. Two neutrons (n) decay into two protons (p), emitting two electrons (e^-).

exchange of light Majorana neutrino is up to now the most appealing, mainly due to the fact that experiments point out the existence of three light massive neutrinos as well as it requires minimal extension of the SM, does not requiring new particles or interactions. The Feynman diagram of the process is shown in Fig. 1.2.
In such scenario, the $0\nu\beta\beta$ half-life can be factorized as

$$[T_{1/2}]^{-1} = G_{0\nu} \left| M_{0\nu} \right|^2 \left| \frac{m_{\beta\beta}}{m_e} \right|^2 \tag{1.3}$$

being $G_{0\nu}$ the lepton phase-space integral that can be determined analytically providing an accurate relativistic description of the nuclear Coulomb field, the electron screening and the finite nuclear size [3]. $M_{0\nu}$ is the nuclear matrix element (NME) describing the probability of the nuclear transition, which will be discussed in more details in the next Section. Finally, $m_{\beta\beta}$ represents the so-called effective Majorana mass defined as

$$m_{\beta\beta} = \left| \sum_{i=1,2,3} e^{i\alpha_i} m_i U_{ei}^2 \right| \tag{1.4}$$

being m_1, m_2 and m_3 the neutrino mass eigenvalues, U_{e1}, U_{e2} and U_{e3} the Pontecorvo–Maki–Nakagawa–Sakata matrix parameters which describe flavor oscillations and include the Dirac CP violating phase whereas α_i are the new Majorana ones. It is important to highlight that, since the smallest absolute neutrino mass is not currently known, two options for neutrino-mass ordering exist: $m_3 > m_2 > m_1$ (normal hierarchy or ordering, NO) and $m_2 > m_1 > m_3$ (inverted hierarchy or ordering, IO). Thus, predictions on $m_{\beta\beta}$ based on global best-fit values of neutrino oscillation parameters have to be calculated considering both scenarios. Moreover, since the complex Majorana phases of the mixing parameters in Eq. (1.4) cannot be probed by oscillations, the allowed region for $m_{\beta\beta}$ is obtained letting them vary freely in the entire (0 - 2π) available range. The effective Majorana mass as a function of the lightest neutrino mass in the 3ν scenario, considering the 3σ regions due to error propagation of the uncertainties on the oscillation parameters, is shown in Fig. 1.3. Thus one expects $m_{\beta\beta}$ of 15-50 meV if neutrino masses are ordered according to the IO and $m_{\beta\beta} < 5$ meV if they follow the NO. It is important to note that a detection of the effective Majorana mass will not be sufficient to determine the mass ordering if the lightest neutrino mass $m_{lightest}$ is above $\sim$ 40 meV. In this case NO and HO become indistinguishable from the point of view of $0\nu\beta\beta$ decay, collapsing in the so-called quasi-degenerate band. On the other hand, experiments which can test the region $m_{\beta\beta} <$ 10 meV can rule out the IO region. Therefore the $m_{\beta\beta}$ value around 0.01 eV represents a physics goal for the current and upcoming $0\nu\beta\beta$-decay experiments.

Since $0\nu\beta\beta$ has not yet been observed, from the $[T_{1/2}]^{-1}$ experimental limits and NME theoretical values, assuming eq. (1.3), it is possible to put a constraint on $m_{\beta\beta}$ value, as shown in Fig. 1.3 by the horizontal band representing the effective Majorana neutrino mass upper limits from KamLAND-Zen experiment [14]. However, the $m_{\beta\beta}$ upper limits thus derived are affected by the uncertainties of NME, see Tab. 1.1. The different theoretical methods, in fact, return quite spreaded values, see Fig. 1.4. As a consequence, varying them within the range allowed by such theoretical calculations one yields the $m_{\beta\beta}$ value bands as the dashed green one shown in Fig. 1.3.

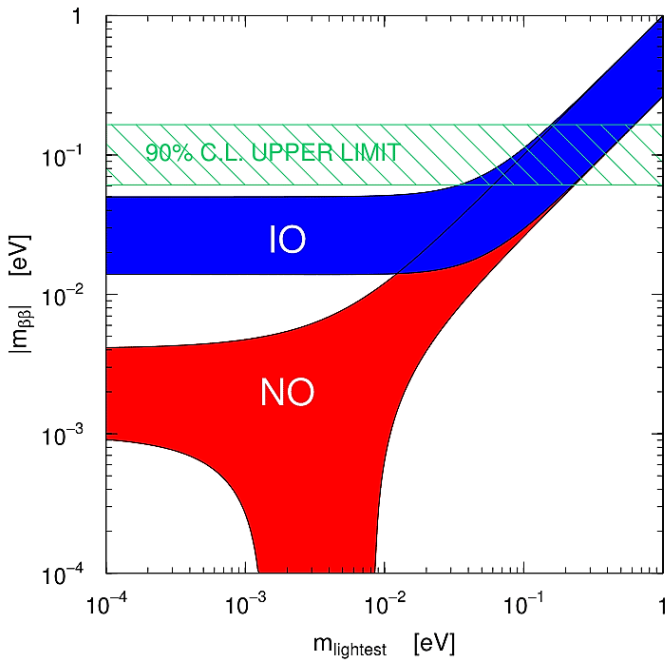

Figure 1.3: Diagram of the effective Majorana mass $m_{\beta\beta}$ as a function of the lightest neutrino mass taking into account the current uncertainties on the neutrino mixing parameters at 99.7% CL and comparing normal (red) and inverted (blue) ordering of the three active neutrinos. The horizontal dashed band indicates the 90% C.L. interval of the effective Majorana neutrino mass $m_{\beta\beta}$ upper limits from KamLAND-Zen experiment for ^{136}Xe [14] using its commonly adopted NME. Figure from Ref. [18].

1.2 Nuclear Matrix Elements

As already mentioned, the conversion between the half-life of the processes and the effective Majorana mass $m_{\beta\beta}$ depends on the NME, which are typically difficult to compute. In fact, $0\nu\beta\beta$ is first of all a nuclear process, therefore the transition has to be described properly, taking into account the relevant aspects that concern nuclear structure and dynamics. What is needed for its evaluation are nuclear structure calculations for the final and initial nuclear states, as well as a proper transition from the fundamental lepton-quark Lagrangian to the lepton-nucleon one. Thus NME calculations $M_{0\nu}$ result a complex task due to many reasons:

- i. The nuclear systems which can undergo $0\nu\beta\beta$ decay are medium and heavy open-shell nuclei with a complicated many-body structure. Thus, all the approaches propose different truncation schemes of the unsolved full nuclear many-body problem into a solvable one, limited to a restricted model space.

- ii. The hadronic operators are often phenomenologically written in terms of the form factors with unknown q^2-dependence.

- iii. The construction of the complete set of the intermediate nuclear states is needed as the $0\nu\beta\beta$-decay is a second order process. A large linear off-shell momentum (~ 100 MeV/c) is in fact available in the virtual intermediate channel thus involving states of any multipolarities.

- iv. The nuclear structure parameter entering in the calculation of NME have to be determined and constrained on associated nuclear processes like single β, $2\nu\beta\beta$-decay, muon and electron capture.

Several theoretical methods can be employed but, as already mentioned and illustrated by Fig. 1.4, there is no full agreement between their results [19, 20]. As a consequence, such prediction limits translates into limits on $m_{\beta\beta}$ which depend on the NME. Moreover, from the comparison with experimental data for the β-decay rates an additional issue emerges: the predicted half-lives are systematically faster than the measured ones, i.e. Gamow-Teller term seems to be weaker in nuclei. To address this evidence, theorists made a phenomenological modification of the strength of the spin-isospin GT operator, by replacing the bare single nucleon value axial coupling constant $g_A = 1.2695$ with an effective one g_A^{eff}. Such de-

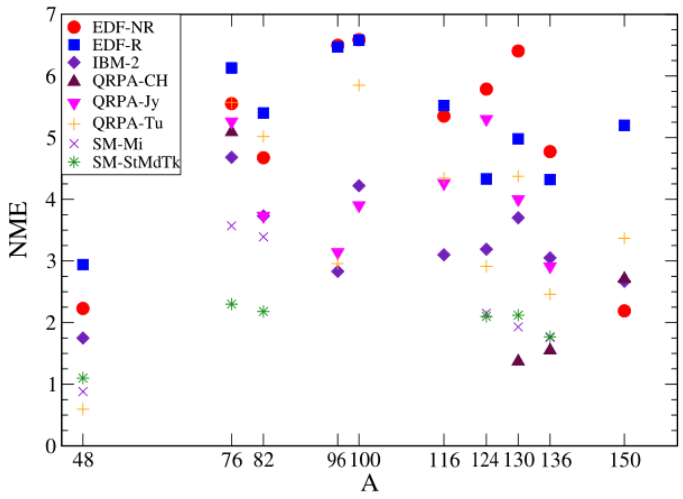

Figure 1.4: A representative compilation of most updated $0\nu\beta\beta$ NME calculations with an unquenched g_A value ($g_A = 1.27$) adopting EDF, IBM-2, QRPA and SM models for different isotopes. Figure from Ref. [21].

gree of renormalization - or quenching q - of the axial coupling $g_A^{eff} = qg_A$ was only very recently addressed - after more than fifty years - for single beta decays [22] but still afflicting the determination of the $0\nu\beta\beta$ NME where the renormalization could be different. It is important to highlight the relevance of such considerations also for the experimental searches: if the g_A value in the nuclear medium is, for example, decreased by a 10(20)% factor, the expected decay rate and therefore the number of signal events will also decrease, approximately of 20(35)%. This change have to be compensated by enlarging the scale of the experiment or increasing the data taking time by a factor of $\sim$ 2.3(6) in such case [23]. In other words, an effect that could be naively considered small has instead a big impact for the $0\nu\beta\beta$ experimental searches.
Because the initial state for the candidate isotopes is the $0^+_{g.s.}$ of the parent nucleus, angular-momentum conservation requires that the spin of the daughter nucleus and the coupled total angular momentum of the two emitted electrons have to be the same, thus coupling to zero the two angular momenta. Thus, in the case of the ground-state-to-ground-state decay the total angular momentum of the emitted electrons have to be

zero and can proceed through emission of two electrons both in the $S_{1/2}$ state. In the transition to the 2^+ final nuclear state, the electrons have to be coupled to two with at least one of the emitted electrons with no zero orbital angular momentum $P_{3/2}$ so hindering this decay mode by the angular-momentum barrier. In addition, transitions to excited states are made less likely by the less favourable phase-space conditions [3] as well as the by the corresponding NME values that are smaller than the g.s. one considering 2^+ or excited 0^+ final states [24]. Thus the main interest is addressed to $0^+_{g.s.} \rightarrow 0^+_{g.s.}$ transitions. However, experimentally the $0^+_{g.s.} \rightarrow 2^+$ transition allows the use of the coincidence method, through the de-excitation γ-ray from the 2^+ state, cleaning the spectrum from the background. Moreover, the rate comparison of the ground-state-to-ground-state transitions to the rates of decays into excited states - namely the first 2^+_1 and 0^+_1 states - would offer the possibility to distinguish between different $0\nu\beta\beta$ mechanisms [16, 25].

1.2.1 Theoretical Description

To date there are no observables that could be straighforwardly linked to the magnitude of $0\nu\beta\beta$ NME and thus could be used to determine them in an essentially model independent way. Therefore one has to rely on theoretical calculations. Over the years many different theoretical nuclear structure approaches have been proposed, varying from the Quasi-Particle Random Approximation (QRPA) [26], the nuclear shell model (NSM) [27], the neutron-neutron Interacting Boson Model (IBM-2) [3], Projected Hartree-Fock-Bogoliubov Method (PHFB) [28], Energy Density Functional Method [29] and Effective Field Theory (EFT) [30]. In the typical scenario, from a weak-interaction hamiltonian density with lepton and nuclear currents, the $0\nu\beta\beta$ two-body transition operators in momentum space can be deduced [31]

$$H = \tau_+\tau_-(-h_F + h_{GT}\sigma_{12} - h_T S_{12}) \tag{1.5}$$

where the three terms correspond to Fermi (F), Gamow-Teller (GT), and Tensor (T) components. This latter is the rank-2 tensor in momentum space that results be expressed as

$$S_{12} = 3(\vec{\sigma_1}\cdot\hat{q}\,\vec{\sigma_2}\cdot\hat{q}) - \sigma_{12}\,, \quad \sigma_{12} = \vec{\sigma_1}\cdot\vec{\sigma_2} \tag{1.6}$$

while the functions $h_{F,GT,T}(q^2)$ represent the form factors entering in the so called neutrino potentials $H_{F,GT,T}$(r, E_k) [32]

$$H_\alpha = \frac{2R}{\pi}\int_0^{+\infty}\frac{f_\alpha(qr)h_\alpha(q^2)qdq}{q+E_k-(E_i+E_f)/2} \tag{1.7}$$

being $f_{GT,F}(qr) = j_0(qr)$ and $f_T(qr) = j_2(qr)$ the spherical Bessel functions. As a consequence, the full nuclear matrix element $M_{0\nu}$ is given as a sum of F, GT and T contributions

$$M_{0\nu} = M_{0\nu}^{GT} - \frac{g_V^2}{g_A^2}M_{0\nu}^F + M_{0\nu}^T \tag{1.8}$$

$0\nu\beta\beta$ decay is a second order process so, in principle, one needs to construct and sum over all the intermediate states of the odd-odd (A, Z + 1) nucleus. However, if one replaces the energies E_k of the intermediate states in Eq. (1.7) by an average constant value one gets the so-called closure approximation

$$E_k \to \bar{E} \tag{1.9}$$

Invoking the closure approximations, thus neglecting the intermediate-state-dependent quantity in the denominator of Eq. (1.7) which is generally small compared to neutrino momentum, the contributions of intermediate states can be summed implicitly. Such approximation avoids the explicit calculation of excited states of the intermediate nucleus up to high energies, a nuclear structure calculation that is computationally even more involved than obtaining the decay initial and final states. Under the discussed approximations, the NME become

$$M_{0\nu}^{GT} = \frac{2R}{\pi g_A^2}\int_0^\infty qdq\,\langle f|\sum_{a,b}\frac{j_0(qr_{ab})h_{GT}(q^2)\vec{\sigma}_a\cdot\vec{\sigma}_b}{q+\bar{E}-(E_i+E_f)/2}\tau_a^+\tau_b^-|i\rangle \tag{1.10}$$

$$M_{0\nu}^{F} = \frac{2R}{\pi g_A^2}\int_0^\infty qdq\,\langle f|\sum_{a,b}\frac{j_0(qr_{ab})h_{F}(q^2)}{q+\bar{E}-(E_i+E_f)/2}\tau_a^+\tau_b^-|i\rangle \tag{1.11}$$

$$M_{0\nu}^{T} = \frac{2R}{\pi g_A^2}\int_0^\infty qdq\,\langle f|\sum_{a,b}\frac{j_2(qr_{ab})h_{T}(q^2)[3(\vec{\sigma}_j\cdot\hat{r}_{ab}\,\vec{\sigma}_k\cdot\hat{r}_{ab})-\vec{\sigma}_a\cdot\vec{\sigma}_b]}{q+\bar{E}-(E_i+E_f)/2}\tau_a^+\tau_b^-|i\rangle \tag{1.12}$$

In $0\nu\beta\beta$ decay, nuclear transitions to intermediate states with spins higher than one are involved via F-like and GT-like operators and are also expected to play an important role as illustrated by Fig. 1.5. The largest component of $M_{0\nu}$ is the GT part [32]. $M^F_{0\nu}$ is the sub-leading contribution, estimated in $M^{GT}_{0\nu}/M^F_{0\nu} \sim$ -2.5 [34]. The tensor contribution plays a significant role when considering mechanism mediated by heavy neutrinos [35] but it is in all the cases smaller than 10% of $M_{0\nu}$ [19, 31].

1.2.2 Uncertainties

Among the possible uncertanty sources entering in $0\nu\beta\beta$ NME calculations, the validity of the closure approximation was discussed at lenght. It was demonstrated that it is accurate when the average excitation energy of the intermediate nucleus $\bar{E}$ is known with an accuracy of a couple of MeV, always returning smaller $M_{0\nu}$ [16]. Comparing the result of non-closure calculation with the one assuming the closure approximation, it was deduced that it is correct to within 1-5% whether average energy is chosen properly [32, 36].
Larger systematic discrepancies can derive from different model spaces, interactions, or short range correlation (SRC) parametrizations which are still open issues in $0\nu\beta\beta$ NME calculations [37]. Such uncertanties, in fact, includes the two-nucleon short range correlations and finite nucleon size, both reducing the magnitude of the $0\nu\beta\beta$ NME. To include the latter, the operators inside the matrix elements of eq. (1.10), (1.11), (1.12) are multiplied by a radial function f, designed to take into account short-range correlations that are omitted by Hilbert-space truncation. The finite nucleon size effect is taken into account via momentum dependence of the nucleon form-factors. Naively, the lack of configurations underestimates the NME, while the lack of correlations overestimates them. However, their importance depends on the type of SRC correlation function and involved form-factor parameters [32].
A deformation dependence of both $M_{2\nu}$ and $M_{0\nu}$ matrix elements has also been found. Despite the nuclei undergoing double beta decay, which are of experimental interest, are spherical or weakly deformed - with exception of ^{150}Nd, which is strongly deformed - it was found that deformation

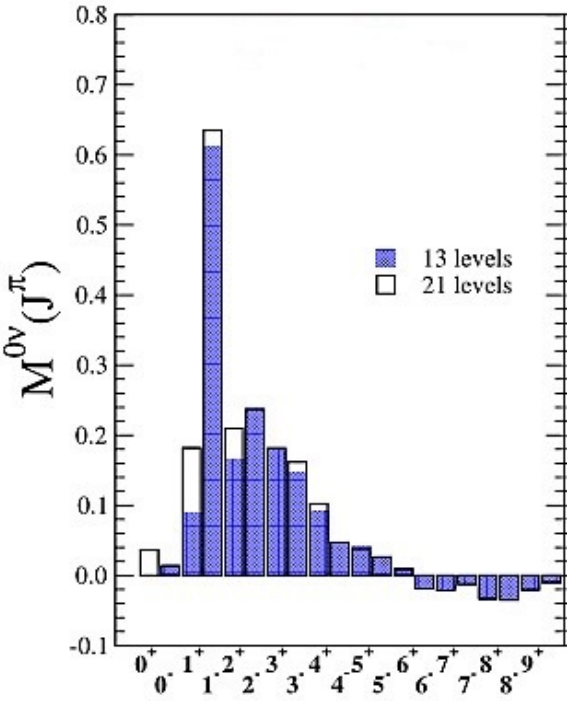

Figure 1.5: Calculated contribution from intermediate states to the $0\nu\beta\beta$ NME according to their momentum and parity assignment (J^{π}) in QRPA approach. Figure adapted from Ref. [33].

introduces a mechanism of suppression of the NME which gets stronger whent the initial and final nucleus deformations differ, resulting in a reduction up to 20% [24, 38]. Despite such general trend, discrepancies about the effect induced by deformation among the different theroretical models are still present for many isotopes [16].
A steady progress in nuclear structure approaches is gradually leading to a better understanding and reduction of the differences among the NME results. However, even in the most refined models $M_{0\nu}$ remain affected by significant uncertainties. In this view, the most promising way to reduce the latter is represented by the comparison with proper experimental results to constrain, in a model-independent manner, the calculation parameter space or to approach the topic from a different perspective.

Chapter 2

Hadron probes for $0\nu\beta\beta$ NME and the NUMEN project

$0\nu\beta\beta$ NME, as discussed in Chapter 1, are crucial for extracting the effective Majorana neutrino mass from the half-life measurement. Since they actually present the major uncertainties among the involved parameters, an experimental program to support the theoretical calculations with as much information as possible has been launched in the last years [39].
In this view, the experimental determination of the neutron occupancies via (p,t) two-nucleon transfer experiments [40, 41] has significantly influenced all NME approaches determining the occupation numbers of neutron and proton valence orbits in the initial and final nuclei. They represent, in fact, important constraints for the nuclear models used in the evaluation of the $0\nu\beta\beta$ NME. It has been demonstrated that, adopting the wave functions constrained to reproduce the experimental occupancies, the calculated $0\nu\beta\beta$ NME shown an enhancement up to 15% compared to previous free calculations [42].
The main interest is, however, for isovector response. In fact, $0\nu\beta\beta$ involves successive single β processes through intermediate states. Among them, low-lying single particle-hole states play dominant roles [43]. Due to the isospin symmetry, the Fermi response is concentrated in a unique transition, named Isobaric Analogue State, which practically exhausts the model-independent sum rule whereas the transitions strengths from other states have negligible contributions. The picture is more interesting

for Gamow-Teller transitions since its strength distribution is a unique property of each nucleus. However, it is already known that most β and $\beta\beta$ strengths are located in the high-excitation region - where the GT giant resonance is present and the double GT (DGT) one is expected - whereas the strengths for the low-lying states are small. The single β matrix elements can be studied experimentally using photon, lepton and hadron probes. The latters involve Single Charge Exchange (SCE) reactions since the nucleon-nucleon interaction is known to include, at least, central isovector and isoscalar, spin-exchange, spin-orbit and tensor components [44].
Using medium-energy light projectiles to inhibit the competing multi-nucleon transfer processes and in the limit of forward scattering angle to suppress the contribution from the spin-orbit and tensor components, the nuclear transition is mainly due to the central isospin and spin-isospin interactions. Under such experimental conditions the cross section dependence from the transferred momentum q and excitation energy E_x can be expressed as

$$\frac{d\sigma}{d\Omega}(q, E_x) = \sigma_\alpha(E_P, A) F_\alpha(q, E_x) B_T^\alpha \tag{2.1}$$

where $\alpha = \{F, GT\}$ indicates Fermi or Gamow-Teller transitions, $F_\alpha(q, E_x)$ describes the shape of the cross section distribution[1] and B_T^α is the beta decay strength of the target nucleus, defined as the square modulus of the corresponding NME.
The proportionality factor between the zero degree cross section and the beta decay strength, $\sigma_\alpha(E_P, A)$, accounts for the kinematic factor between the initial and final channels, the volume integral of the nucleon-nucleon interaction and the distortion of the incoming and outcoming waves due to the nuclear interaction. Such proportionality relation between the zero degree SCE cross section and single β decay strength, originally proposed by Goodman et al. [45] and theoretically described by Taddeucci [46] has been widely tested from the experimental side with high successful. In particular, light-ion induced reactions such as (n, p), (p, n), (d, ^{2}He), (^3He, t), (t, ^3He) at bombarding energies above 100 AMeV have highlighted a

[1] It reduces to Bessel function in the limit of $q \sim 0$.

remarkable proportionality between measured cross sections and known β-strengths for a large number of states in many systems. Such results have made SCE a unique spectroscopic tool to extract information from measured reaction cross sections.
Heavy-ion induced SCE reactions, instead, present a more involved picture, due to the projectile degrees of freedom, the sizeable amount of momentum transferred even at forward angles and the relevance of multistep processes with respect to the direct one. However, they offer the possibility to study nuclear states that are inaccessible to the more frequently used light reactions, thus motivating a recent renewed interest. This feature is interesting since neither β-decay nor light ions induced SCE reactions can effectively probe the nuclear response to the higher multipoles of the isospin (F-like) and spin-isospin (GT-like) operators which are considered to give a major contribution [47, 48] to $0\nu\beta\beta$ NME transitions. A full quantum mechanical description of heavy-ion induced SCE reactions has been introduced [49] very recently, confirming the connection - at low momentum transfer - with β decay-type transitions through a factorization expression similar to the one reported in eq. (2.1). This proves that heavy-ion reactions of a few tens of MeV per particle are well suited for β-like explorations, resulting also to a large extent independent of the multipolarity. The latter represents a remarkable achievement, providing a tool to investigate the nuclear transitions to the high-spin intermediate states involved in $0\nu\beta\beta$ NME calculations.
In the present Chapter a new nuclear approach to infer $0\nu\beta\beta$ NME based on the extensively use of heavy-ion induced DCE reactions will be discussed. It represents the core of the NUMEN project.

2.1 Heavy-Ion Double Charge Exchange Reaction

In DCE nuclear reactions the nuclear charge of the colliding projectile and target nuclei changes by two units leaving the mass number invariant. Such processes are characterized by the transfer of two units of the isospin

third component ($\Delta T_z = \pm 2$) between projectile and target

$$a(N_a, Z_a) + A(N_A, Z_A) \rightarrow b(N_a \pm 2, Z_a \mp 2) + B(N_A \mp 2, Z_A \pm 2) \quad (2.2)$$

The heavy-ion (HI) DCE reactions, in particular, present a number of important similarities with $0\nu\beta\beta$ decay, even if they are mediated by different - strong and weak - interactions. Among the most important ones:

i. Parent/daughter nuclear states of the $0\nu\beta\beta$ decay are the same as those of the target/residual nuclei in the DCE thus probing the same wave functions.

ii. Short-range Fermi, Gamow-Teller and rank-2 tensor components are present in both the transition operators, with relative weights depending on the incident energy for DCE. Thus, performing the DCE experiments at different bombarding energies could give sensitivity to the individual contribution of each component.

iii. A large linear momentum (~ 100 MeV/c) is available in the virtual intermediate channel in both processes [50]. This is a distinctive similarity since other processes such as single β decay, $2\nu\beta\beta$ decay, light-ion induced SCE cannot probe this feature [51].

iv. Both processes take place in the same nuclear medium. In-medium effects are expected to be present in both cases, so DCE data could give a valuable constraint on the theoretical determination of quenching phenomena on $0\nu\beta\beta$.

v. An off-shell propagation through virtual intermediate channels is present in both cases. In practice, a supplementary contribution of several MeV to the line width is present in the intermediate virtual states. This is related to the transit time of a particle - neutrino in weak case and pair of nucleons in the strong one - along the distance of the two vertices of the $0\nu\beta\beta$ and DCE reaction.

In the past, several attempts to study DCE using pion beams via the (π^+, π^-) or (π^-, π^+) reactions were led [52, 53, 54]. Some remarkable results were achieved, leading to the observation of second order collective excitations as the Double Isobaric Analogue State (DIAS) as well as the double dipole resonance states (DGDR). However, none of these was conclusive in the $\beta\beta$ process assessment since π-DCE nuclear transition operators presents very different structure [55]. Moreover, π having zero spin are unlikely to excite the fundamental spin-isospin GT excitations.

Few explorative studies of DCE processes induced by heavy-ion were performed over the past years, regarding their possible connection with $\beta\beta$ decay as well as the chance to investigate two-nucleon pairing correlation [56] in stable and unstable nuclei. Such investigations, however, were not conclusive, strongly limited by the very poor yields of the measured energy spectra as a consequence of the low cross sections involved. Due to these discouraging results, the study on DCE reactions and its possible relation with $\beta\beta$ decay was not systematically carried out. Nowadays the conditions are more favourable, thanks to the advent of new performing facilities, to tackle the experimental challenges in order to deeply investigate such nuclear processes. From the theoretical side, despite a complete quantum theory for DCE reactions is still not fully established, a new theoretical scenario was recently introduced [57]. It has been shown that DCE reaction can proceed as a one-step reaction via a special kind of two-body interaction generated by a correlation diagram similar to the $0\nu\beta\beta$, see Fig. 2.1. Such direct mechanism, which due to the similarities with $0\nu\beta\beta$ diagram was named Majorana-DCE (MDCE) [58], proceed via an exchange of π and ρ scalar mesons. It is a two-nucleon process built upon the simultaneous emission of two charged $q\bar{q}$ pairs in highly virtual vector rho-meson modes. At the end, the highly off-shell $q\bar{q}$ compounds will decay into mesons, preferentially into pions but also multi-pion configurations like the scalar and vector mesons. The neutral pion is used to establish a two-nucleon correlation while the charged pion is emitted. Its contribution has to be distinguished from second order DCE reactions, given by double single charge exchange (DSCE) processes [59] which resembles the diagram of $2\nu\beta\beta$ decay [60]. Finally, also the sequential nucleons exchange in multi-step transfer processes has to be considered. The first two mechanisms have quite different origin with respect to the last one: the meson exchange, in fact, is typical of the nucleon-nucleon correlation while the multi-nucleon transfer is triggered by the mean field action of the colliding nuclei. All the mentioned mechanisms contribute coherently to the measured nuclear cross section so it is important to determine the experimental conditions where the meson exchange mechanism is dominant, since the desired nuclear structure information possibly connected with the $\beta\beta$ one is available only from the direct process.

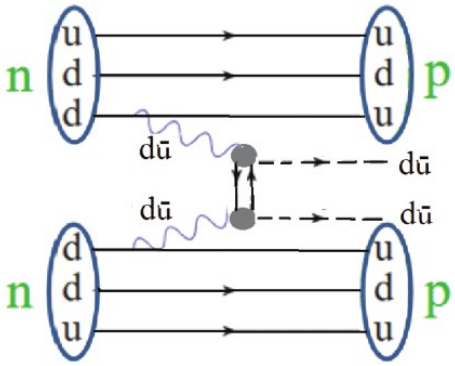

Figure 2.1: Schematic diagram illustrating the hadronic surrogate process of $0\nu\beta\beta$ decay. Figure adapted from Ref. [58].

2.1.1 Past Studies

In the past, few not encouraging experiments have been performed and most of them were not conclusive because of the very low cross sections, high background and small collected yields. Conflicting information were extracted by first (^{18}O, ^{18}Ne) DCE reactions. Blomgren et al. [61] were able to extract the angular distributions for different integrated excitation energy range for the ^{24}Mg(^{18}O, ^{18}Ne)^{24}Ne reaction at 76 AMeV 2.2. They suggested that the almost flat cross section behavior extracted in the low-energy excitation intervals could be justified by the possibility of a destructive interference between the direct and the sequential processes. However, the statistical uncertainty prevented any far-reaching conclusions.
More recently, Matsubara et al. [62] and Takaki et al. [63], investigating unbound ^{9}He and ^{12}Be nuclei through (^{18}O, ^{18}Ne) at 80 AMeV concluded in favor of multipolarity sensitivity transitions due to the different shapes of cross section angular distribution.
The multi-nucleon transfer dominance over the direct DCE reaction mechanism was observed for the transitions to the 0^+ ground state and the 2^+ of ^{40}Ar in (^{14}C, ^{14}O) reaction on ^{40}Ca at 51 MeV [64]. The appreciably large cross section of the 2p-pickup reaction ^{40}Ca(^{14}C, ^{16}O)^{38}Ar, measured

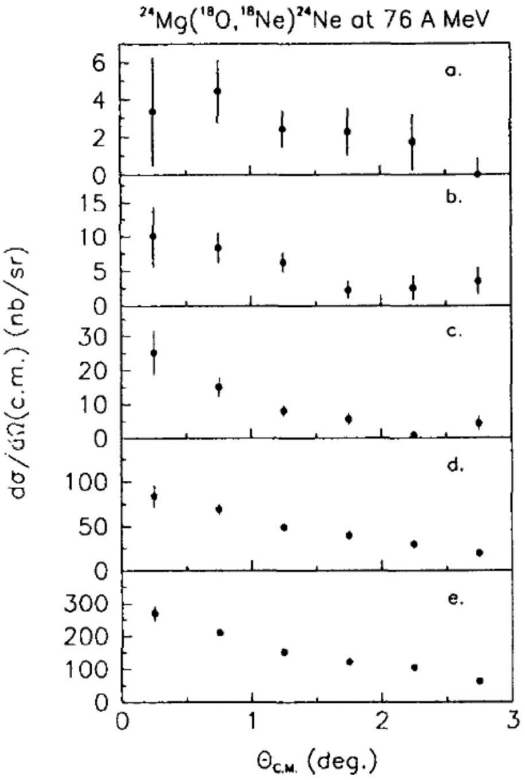

Figure 2.2: ^{24}Mg(^{18}O, ^{18}Ne)^{24}Ne DCE reaction angular distributions for different excitation energy intervals. (a) 0.0 - 4.5 MeV, (b) 4.5 - 7.5 MeV, (c) 7.5 - 10.0 MeV, (d) 10.0 - 15.0 MeV and (e) 15.0 - 20.0 MeV from Ref. [61].

in the same experiment, suggested that the independent transfer of two neutrons and pickup of two protons from the target was the leading reaction mechanism [65].

2.1.2 A First Modern HI-DCE Study: ^{40}Ca(^{18}O, ^{18}Ne)^{40}Ar

As discussed in the previous Section, the measurement of DCE high-resolution energy spectra, especially at very forward angles, are expected to be crucial to identify the transitions of interest for $0\nu\beta\beta$. The concurrent measurement of the other relevant reaction channels is also crucial in order to isolate the direct DCE mechanism from the competing multi-transfer processes. A first complete investigation of heavy-ion induced DCE was carried out by Cappuzzello et al. [66] for the ^{40}Ca(^{18}O, ^{18}Ne)^{40}Ar reaction at 15 AMeV. Such study was conceived to test the experimental feasibility of DCE reaction researches using modern detectors like the MAGNEX large acceptance magnetic spectrometer [92]. To select the best experimental conditions to investigate DCE reactions, several aspects regarding the structure of the involved nuclei and the dynamical conditions have been considered.

^{40}Ca(^{18}O, ^{18}Ne)^{40}Ar @ 15 AMeV: the choice of projectile/target system and kinematic conditions

As shown since the first studies, DCE reaction cross sections are expected to be small. Thus an appropriate choice of the projectile-ejectile system is required to favor them. The (^{18}O, ^{18}Ne) reaction is advantageous because the two nuclei ^{18}O and ^{18}Ne belong to the same multiplet in spin (S) and isospin (T) and in particular the ^{18}O, (0^+, T = 1) to ^{18}Ne (0^+, T = 1) transition through the intermediate ^{18}F (1^+, T = 0) is a strong one since the GT sum-rule strength is exhausted by the lowest energy 1^+ state. In addiction, the ^{18}O is the lightest non-radioactive T = 1 nucleus so it can be produced and accelerated with high intensities. Such reaction allows to populate target-residual system in the $\beta^+\beta^+$ direction. The target transition ^{40}Ca^{0+} $\rightarrow$^{40}Ar^{0+} is not a superallowed DGT as for the projectile-ejectile system. However the GT strength in not much fragmented in the intermediate channel and the Fermi transition is exhausted

by the 0^+ state at 4.4 MeV.
The choice of the proper beam energy is another important point in order to favour the experimental conditions suitable for studying the direct process involved in DCE reactions, disfavouring at the same time the sequential one. An estimation for the transfer mechanism contributions to the cross section can be carried out adopting the well established Brink's kinematic matching conditions [67] that relate the cross section to the reaction Q-value and the angular momentum transferred.

^{40}Ca(^{18}O, ^{18}Ne)^{40}Ar @ 15 AMeV: Experimental results

The ^{40}Ca(^{18}O, ^{20}Ne)^{38}Ar two-proton transfer, ^{40}Ca(^{18}O, ^{18}F)^{40}K SCE and the ^{40}Ca(^{18}O, ^{18}Ne)^{40}Ar DCE energy spectra were measured with an energy resolution of $\sim$ 500 keV, see Fig. 2.3.
As expected, in the two-proton transfer energy spectrum of Fig. 2.3(a) the cross section tends to increase with excitation energy as a consequence of the kinematic Q-matching conditions (Q_{opt} = 32 MeV) showing a cross section value around zero-degree of $\sim$ 3 μb/sr for the ^{40}Ca(^{18}O, ^{20}Ne)^{38}Ar$_{gs}$. Such value is not larger than the DCE one, differently from what reported by by Drake et al. [64] in their ^{14}C+^{40}Ca study at 51 MeV where the ^{40}Ca(^{14}C, ^{16}O)^{38}Ar two-proton transfer cross section was almost two orders of magnitude higher than the corresponding ^{40}Ca(^{14}C, ^{14}O)^{40}Ar. Such result - referable to the higher matching of the two-proton transfer channel for the ^{14}C+^{40}Ca reaction (Q_{opt} = 10 MeV, L_{opt} = 3) - is a hint for a negligible transfer contribution in the ^{18}O+^{40}Ca system.
The ^{40}Ca(^{18}O, ^{18}F)^{40}K charge exchange spectrum shown in Fig. 2.3(b) presents some structure but the high level density and the experimental energy resolution did not allow to isolate single transitions. About the DCE energy spectrum of Fig. 2.3(c), the ^{40}Ar ground state is clearly separated from the not resolved doublet of states ^{40}Ar 2^+ at 1.460 MeV and ^{18}Ne 2^+ at 1.887 MeV. Moreover, the angular distribution for the transition to the ^{40}Ar 0^+ ground state shown in Fig. 2.4 presents an oscillating pattern whose minima are quite well reproduced by the $|\, j_0(qR)\,|^2$ Bessel function, where $R = 1.4(A_1^{\frac{1}{3}} + A_2^{\frac{1}{3}})$ and $A_{1,2}$ are the projectile and target mass numbers. Such oscillating behavior is not expected in complex multi-step transfer reactions, due to the large number of angular mo-

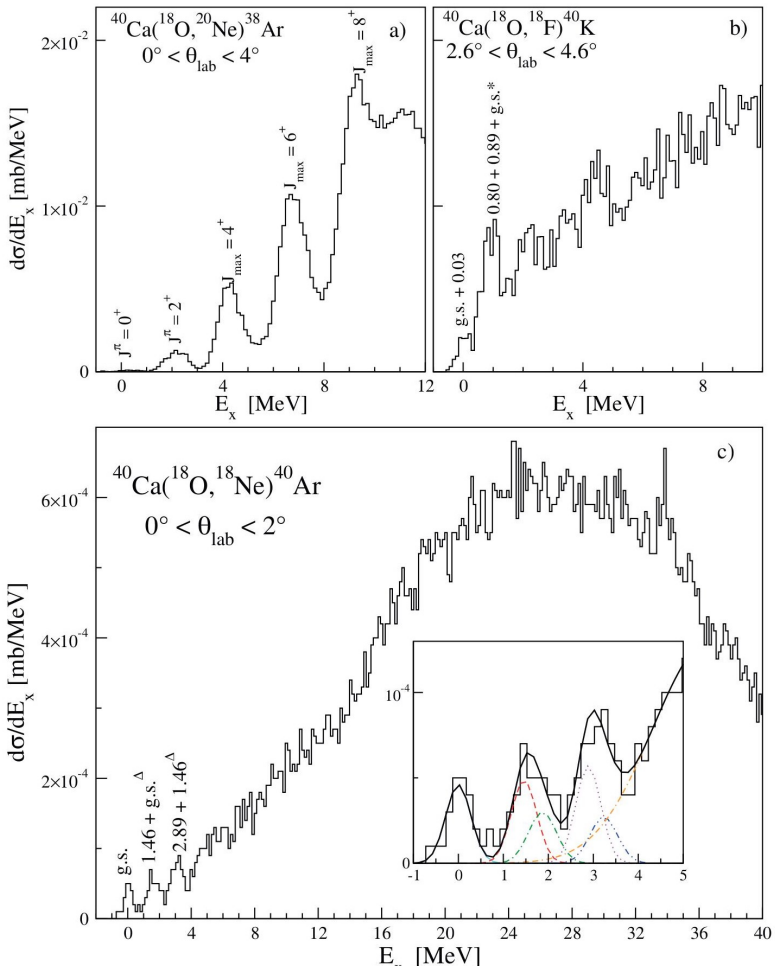

Figure 2.3: (a) Energy spectrum measured in the ^{40}Ca(^{18}O, ^{20}Ne)^{38}Ar 2p-transfer. (b) Energy spectrum from ^{40}Ca(^{18}O, ^{18}F)^{40}K SCE. The symbol g.s.* indicates the ^{40}Ca(^{18}O, ^{18}F$_{0.937MeV}$)^{40}K$_{g.s.}$ transition. (c) Energy spectrum from ^{40}Ca(^{18}O, ^{18}Ne)^{40}Ar DCE. The symbols g.s.$^{\Delta}$ and 1.46$^{\Delta}$ indicate the ^{40}Ca(^{18}O, ^{18}Ne$_{1.87MeV}$)^{40}Ar$_{g.s}$ and ^{40}Ca(^{18}O, ^{18}Ne$_{1.87MeV}$)^{40}Ar$_{1.46MeV}$ transitions, respectively. In the inset, a magnification of the low-lying states and a fit with 6 Gaussian functions (black solid line) is shown. The latter are centered at 0 (cyan solid), 1.46 (red dashed), 1.87 (green dot-dashed), 2.89 (magenta dotted), (1.46 + 1.87) = 3.33 (blue double-dot-dashed) and 5.6 MeV (orange dot-double-dashed) respectively.

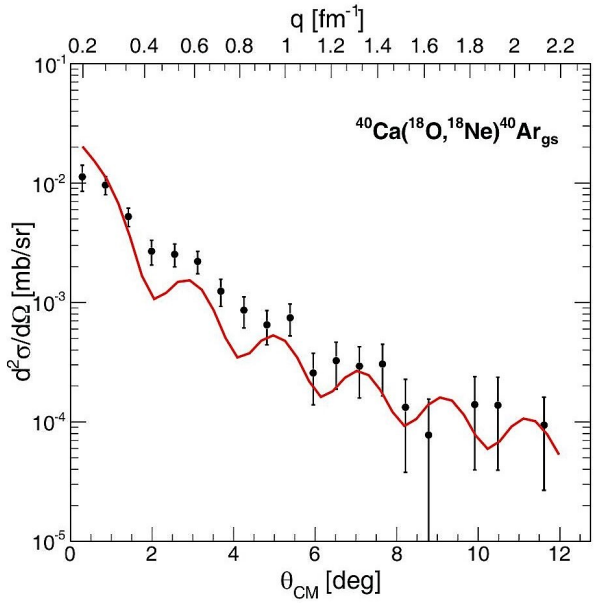

Figure 2.4: Differential cross section angular distribution of the ^{40}Ca(^{18}O, ^{18}Ne)^{40}Ar$_{g.s.}$ transition as a function of the scattering angle in the center of mass frame θ_{CM} and momentum transferred q. The red curve represents the L = 0 Bessel function folded with the experimental angular resolution ($\sim$ 0.6 °) and scaled to reproduce the incoherent sum of the predicted DF and DGT cross sections.

menta involved in the intermediate channels which would determine a structureless cross section distribution, thus representing another indication of the absence of such contributions.

^{40}Ca(^{18}O, ^{18}Ne)^{40}Ar @ 15 AMeV: A simple model to infer ^{40}Ca NME

In the lack of a well established microscopic theory to describe the DCE reaction, the authors of Ref. [66] assumed a DCE cross section factorization analogue to the SCE one [68] distinguishing between transitions originated by spin-isospin (GT-like) and isospin (F-like) operators with different multipolarities due to the large amount of momentum available. To simplify the estimation for the matrix element of DCE process, it was assumed either a pure DGT or DF transition. In particular, from

the measured DCE cross section at 0°, adopting the volume integrals from the SCE case and calculating the distortion and correction factors, the unit cross sections for the DGT and DF operators were estimated. In case of GT transitions, as depicted in Fig. 2.5, the sum over the energy distribution of ^{40}K 1^+ state up to 8 MeV for the on-shell contribution plus $\sim$ 7 MeV to account for the off-shell one were considered. In DF case only the ^{40}K 0^+ state at 4.38 MeV and the ^{18}F 0^+ state at 1.04 MeV were assumed in the intermediate channel. The extracted estimations for the maximum double Gamow-Teller and double Fermi strengths, $B^{DCE}(DGT) = B_P(DGT)B_T(DGT) < 0.2$ and $B^{DCE}(DF) < 0.31$, resulted not far from the values obtained combining the literature ones for the same transitions scheme, $B(DGT) = B_P(DGT)B_T(DGT) = 0.11$ and $B(DF) = B_P(DF)B_T(DF) = 0.42$ respectively.

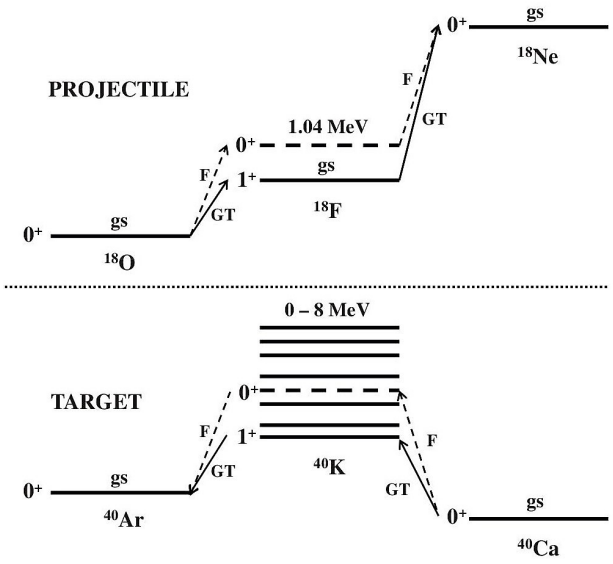

Figure 2.5: Scheme of the GT and F projectile and target transitions used to determine the B(DGT) and B(DF).

Since both DF and DGT are expected to contribute to the DCE total cross section at θ = 0°, their two contributions to the DCE cross section were estimated. Their incoherent sum value, amounting to 6 $\frac{\mu b}{sr}$ for DGT and

15 $\frac{\mu b}{sr}$ for DF, results comparable to the experimental one of $11\frac{\mu b}{sr}$. Then, the ^{40}Ca target NME was extracted. Finally, the ^{48}Ca $0\nu\beta\beta$ NME was inferred: $M_{0\nu}(^{48}\text{Ca}) = 2.6 \pm 1.3$ resulting compatible with those from literature [19, 69].

^{40}Ca(^{18}O, ^{18}Ne)^{40}Ar @ 15 AMeV: A test ground for the new Majorana-DCE reaction theory

The ^{40}Ca(^{18}O, ^{18}Ne)^{40}Ar DCE reaction data [66] just discussed have been recently examined on the basis of a recent introduced theory of heavy-ion DCE reaction (Majorana-DCE, MDCE) [57] based on the correspondences with the $0\nu\beta\beta$ decay. In such new approach, the calculations are performed by one-step Distorted Wave Born Approximation and the distortion coefficient is evaluated in black disk approximation due to the strong absorption in grazing ion–ion collisions. The transition strengths are taken from QRPA calculations. In this first investigation the form factors and interactions were treated schematically by approximating the complex off-shell momentum structure by the on-shell strength. This introduces an overall scaling factor which was fixed by normalizing the total cross section to the data point at the smallest scattering angle. First results of the MDCE model are shown in Fig. 2.6. The forward peak of the angular distribution is dominated by the (L = 0, S = 0) component. However, the (L = 2, S = 2) one is of comparable importance at the larger scattering angles, resulting essential for the overall description of the cross section angular distribution data.
This first result indicates that the MDCE mechanism is very promising for the description of heavy-ion DCE reaction at the energy of tens AMeV even if has to be further refined. Moreover, such theoretical analysis has to be extended to different colliding systems in order to systematically test its robustness and deeply investigate the link with $0\nu\beta\beta$.

2.2 The NUMEN project

The success of the first pilot experiment for the DCE reaction on ^{40}Ca and the considerations about the role of the competitive channels have opened

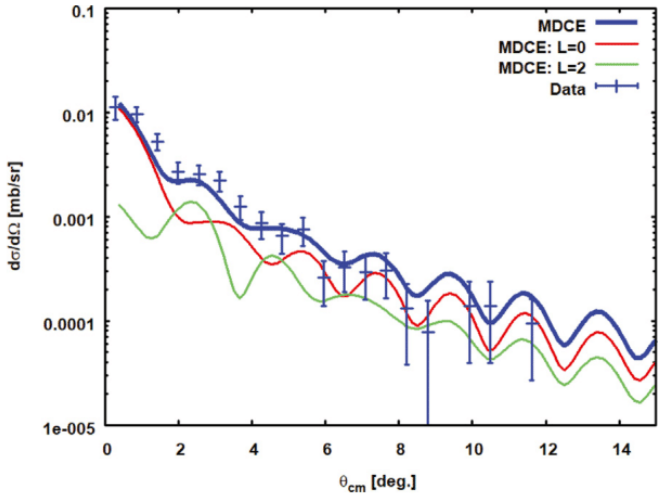

Figure 2.6: Comparison between the experimental angular distribution of the ^{40}Ca(^{18}O, ^{18}Ne)^{40}Ar$_{g.s.}$ DCE reaction and the new MDCE model. Figure adapted from Ref. [57].

the way to the idea of a more systematic and thorough investigation of heavy-ions induced DCE and their connection to $\beta\beta$ processes, carried out by the NUMEN collaboration.
The NUMEN (NUclear Matrix Elements for Neutrinoless double beta decay) project was proposed with the aim to investigate the nuclear response to DCE reactions for all the isotopes explored by present and future $0\nu\beta\beta$ decay studies.
The experimental approach toward the determination of $0\nu\beta\beta$ NME is the main goal of the project itself. NUMEN, in fact, proposes to access the nuclear matrix elements entering the expression of the life time of the $0\nu\beta\beta$ decay by measuring DCE reaction cross sections at different incident energies. To achieve this goal, one needs to test if the DCE measured cross sections and in turn DCE matrix elements are connected to $0\nu\beta\beta$ ones as a smooth and thus controllable function of the projectile energy and of the system mass. In this view, some clues result from different nuclear structure model calculations [70, 71] which have shown a nearly linear proportionality relation between DGT transitions - accessible in DCE reactions - and $0\nu\beta\beta$ decay NME, due to the pairing interactions. Moreover,

DCE reaction cross section measurements could have a major impact in tuning the nuclear structure theories of $0\nu\beta\beta$ NME, providing an independent testing ground for the approximations used to deduce the wave functions of the $0\nu\beta\beta$ candidate nuclei.
Experimental key requirements to perform DCE nuclear reaction investigations are a low emittance heavy-ion beams and a high performance detection system. The first is fulfilled by the use of the K800 Superconducting Cyclotron installed at LNS-INFN [72]. The MAGNEX large acceptance magnetic spectrometer represents the suitable facility for the detection of the ejectiles of interest, guaranteeing the challenging sensitivity and resolution required to measure rare DCE reactions over a large background coming from other intense reaction channels. The use and the features of the powerful techniques for the particle identification and the high-order trajectory reconstruction, implemented in MAGNEX, will be discussed in Chapter 3. Here is important to highlight that, at the moment, a limitation on the beam current delivered by the accelerator and on the maximum rate accepted by the MAGNEX focal plane detector exists. It must be sensibly overcome in order to systematically provide accurate nuclear structure information to the neutrino physics community for all the interesting cases. Thus, an upgrade of the INFN-LNS facilities is part of the project itself. This latter, in fact, is structured into several phases, briefly presented in the following, each one defined by the fulfillment of intermediate goals.

Phase I: the pilot experiment. The ^{40}Ca(^{18}O, ^{18}Ne)^{40}Ar DCE reaction at 15 AMeV discussed in the previous Sections returned the first example of high resolution and statistically significant experimental data for an heavy-ion DCE reaction in a wide range of transferred momenta, proving the experimental feasibility of the project. Moreover, the measurement of the competing processes ^{40}Ca(^{18}O, ^{18}F)^{40}K SCE, ^{40}Ca(^{18}O, ^{20}Ne)^{38}Ar 2p-transfer and ^{40}Ca(^{18}O, ^{16}O)^{42}Ca 2n-transfer demonstrated that the experimental investigation of their contributions to the DCE channel cross section is possible.

Phase II: from the pilot to the "hot" cases. The availability of the MAGNEX spectrometer for high resolution measurements of very suppressed

reaction channels was crucial in the ^{18}O+^{40}Ca pioneering measurement. However, with the present set-up it is difficult to suitably extend this research to the all cases, where $\beta\beta$ decay studies are and will be focused. In fact, the cross sections expected for such systems are lower than the ^{40}Ca measured one and the ^{20}Ne and ^{18}O beam current intensities are actually limitated by the CS accelerator to maximum value of the order of tens enA. Target thickening is not a feasible solution in order to preserve the energy spectra resolution necessary to isolate, at least, the g.s $\rightarrow$ g.s. from the other low-lying transitions. All of these considerations suggest that the beam current of the DCE experiments must be increased of two orders of magnitude. However, also the present tolerable event rate of the MAGNEX focal plane detector is limitated to few kHz. As a consequence, the MAGNEX focal plane detector [73], its electronical read-out [74, 75] as well as the beam transport lines [76] and the target system [77, 78] have to change. Moreover, in order to further increase the experimental energy resolution, the introduction of a coincident γ-rays detector array is foreseen [79]. The R&D of all these activities is already in progress and represents an important part of the present Phase II. From the experimental view, with the current experimental set-up, the attention is at the moment focused on a few favorable cases for $\beta\beta$ decay, including the ^{116}Cd discussed in the present Thesis, with the goal to achieve conclusive results for them. The theoretical investigation of the DCE reactions, crucial to deduce possible information on $0\nu\beta\beta$, represents another fundamental part of the present Phase.

Phase III: the facility upgrade. Once all the R&D activities for the upgrade of the whole facility will be ready, the disassembling of the old setup and re-assembling of the new one will start at the INFN-LNS.

Phase IV: the experimental campaigns. The last phase will consist of the systematic experimental campaigns at high beam intensities - some pμA expected - and integrated charge of hundreds of mC up to C, spanning all the $0\nu\beta\beta$ decay candidate isotopes, like: ^{48}Ca, ^{76}Ge, ^{76}Se, ^{82}Se, ^{96}Zr, ^{100}Mo, ^{106}Cd, ^{110}Pd, ^{116}Cd, ^{110}Sn, ^{124}Sn, ^{128}Te, ^{130}Te, ^{136}Xe, ^{130}Xe, ^{148}Nd, ^{150}Nd, ^{154}Sm, ^{160}Gd, ^{198}Pt.

The detailed description of the NUMEN project and its phases as well as all the adopted solutions foreseen for the facility upgrade are widely discussed in Ref. [79].

2.3 (^{20}Ne, ^{20}O) Double Charge Exchange Reaction

The (^{20}Ne,^{20}O) DCE reaction has been introduced for the first time by the NUMEN collaboration, with the aim to probe $\beta^-\beta^-$-like target nuclear response, being most $0\nu\beta\beta$ candidates $\beta^-\beta^-$ emitters.
^{20}Ne and ^{20}O belong to the isobaric isospin quintet (A = 20, T = 2) consisting of ^{20}Mg (T_z = -2), ^{20}Na (T_z = -1), ^{20}Ne (T_z = 0), ^{20}F (T_z = +1), and ^{20}O (T_z = +2) which is also the lightest isospin multiplets where all members are stable against particle emission, and the lightest isospin multiplets that can be described within the s-d shell.
However, as shown by Fig. 2.7, ^{20}Ne and ^{20}O are not mirror systems so the $0^+_{g.s.} \rightarrow 0^+_{g.s.}$ transition is not expected to be dominated by a specific one. No spectrosopic studies of (^{20}F, ^{20}O) reaction have been reported yet while ^{20}Ne $\rightarrow$ ^{20}F transitions have been analyzed via ^{20}Ne$(n,p)^{20}$F reaction at E_n = 198 MeV [81]. The excitation energy spectrum at very forward angles shows a peak at 1 MeV which may have contributions from several final states due to the limited experimental energy resolution. GT strength distribution, in particular, was deduced thanks to a multiple decomposition analysis (MDA), resulting rather weak and spreaded over a wide region of excitation energies. The decomposition indicates a ΔL = 0 continuum strength with the exception of one discrete state at E_x = 1.0 MeV. The measured transition strength to this state in ^{20}F, B(GT) = 0.161$\pm$0.029, is in reasonable agreement with the Shell Model prediction of 0.142. Such results is also in good agreement with the one from an earliest measurement made using the ^{20}Ne$(\pi^-, \gamma)^{20}$F reaction in which the 1.0 MeV state was the only 1^+ state populated and B(GT) = 0.1607$\pm$0.030 was obtained. Because of the approximate charge symmetry of nuclear forces, similar GT strengths should be seen for analog transitions in ^{20}F, ^{20}Ne, and ^{20}Na using the (n,p), (p,p'), and (p,n) reactions. Indeed, high resolution ^{20}Ne(p,p') at low momentum transfer shows the 1^+ peak at

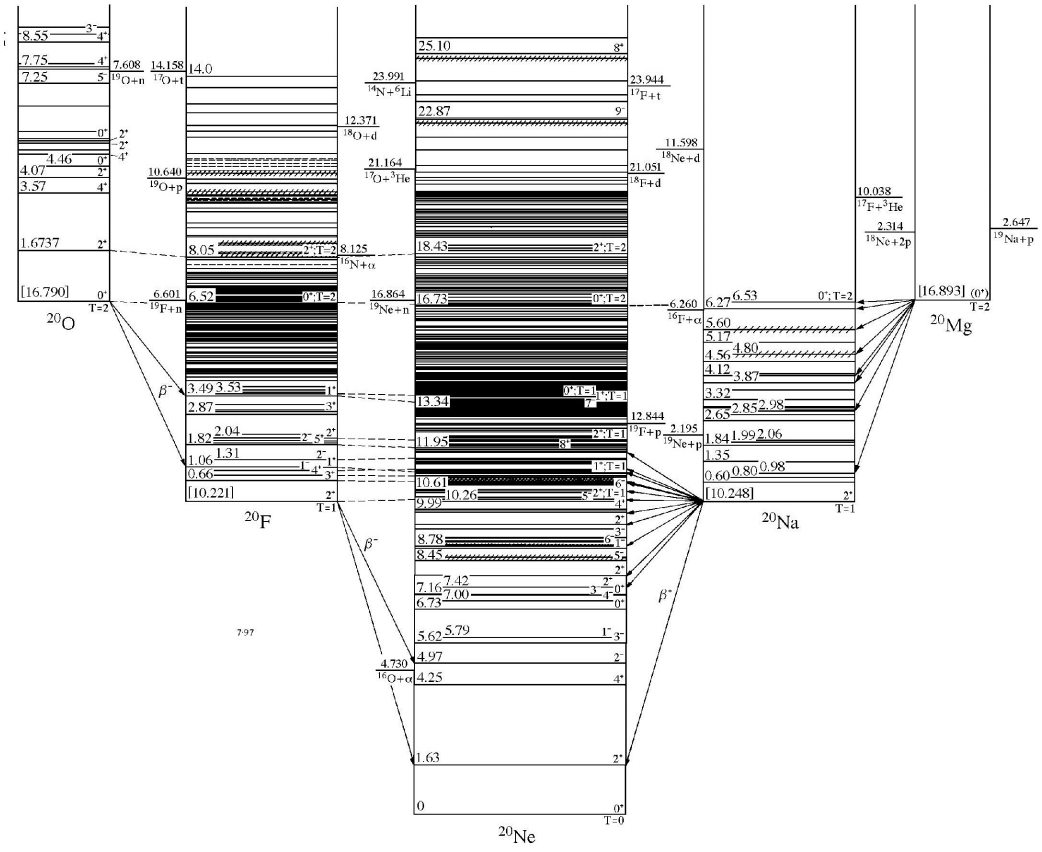

Figure 2.7: Isobar diagram, A = 20. The diagrams for individual isobars have been shifted vertically to eliminate the neutron-proton mass difference and the Coulomb energy, taken as $E_C = 0.60Z(Z-1)/A^{1/3}$. Energies in square brackets represent the approximate nuclear energy. Figure adapted from Ref. [80].

11.26 MeV with an obtained B(GT) = 0.185±0.02. Nowadays, (d, ^{2}He) high resolution measurements could shed light on the GT strength distribution structure up to high excitation energy.
Recently, an optical model study of the ^{20}Ne nucleus via elastic and inelastic scattering was performed with ^{76}Ge at 15 AMeV [82]. The elastic scattering angular distribution turned out to be highly sensitive to the ^{20}Ne deformation value as well as, due to the high absorption, the coupling to first low-lying excited states.

2.4 The $^{116}Cd \rightarrow {}^{116}Sn$ case

As already mentioned, medium-energy (E/A = 0.1 - 0.3 GeV) light-ion induced SCE studies on isotopes candidates for $0\nu\beta\beta$ decay were systematically carried out with the aim to test the relevant nuclear transitions among such systems [51, 83, 84]. In particular, the GT response in the intermediate system is separately explored from the parent and the daughter side to study nuclear transitions relevant to $\beta\beta$ processes. Thus, the high resolution GT$^{\pm}$ strength measurement can give significant insight into the details of the nuclear structure and can help to determine the $\beta\beta$-decay NME less nuclear model dependent [85]. However the connection is not straightforward because the relative phase between the two GT contributions cannot be measured. Moreover, the transition probabilities to individual 1^+ states are extracted from the experiments for each single step, while in the $\beta\beta$ NME the amplitudes are needed with the proper phase since they add coherently.
In case of ^{116}Cd $\rightarrow$ ^{116}Sn $\beta\beta$-decay partners, GT$^{\pm}$ transition strenghts were investigated in the past via the ^{116}Cd$(p,n)^{116}$In and ^{116}Sn$(n,p)^{116}$In reactions at 300 MeV [86] as well as ^{116}Cd(d,^{2}He)^{116}In [85]. It was demonstrated that ^{116}Cd - as well as ^{96}Zr and ^{100}Mo where valence neutrons and valence protons are in the different major shells - presents one strong GT state of $(g7/2)_n(g9/2)_p$ to the intermediate nucleus ground state. GT transitions to intermediate 1^+ states are particularly important for $2\nu\beta\beta$ as confirmed by QRPA calculation in the hypothesis of Single State dominance (SSD). SSD hypothesis suggests that $\beta\beta$-decay transitions are governed by the transition through the first 1^+ state of the intermediate nu-

cleus. It works well in case of nuclei where there is only one 1^+ state among the low-lying intermediate ones as for ^{116}Cd but also for ^{100}Mo and ^{128}Te. If it is not the case, one has to take into account not only the lowest but also the other intermediate low-lying 1^+ states in the so-called low-lying-state dominance (LLSD) approximation to account for the $2\nu\beta\beta$-decay rates [87].
However, in $0\nu\beta\beta$ nuclear transitions to intermediate states with spins higher than one are involved via F-like and GT-like operators and are also expected to play an important role (see Fig. 1.5). Thus, they could be experimental investigated, at small momentum transfer, via heavy-ion SCE reactions through MDA in order to extract F- and GT-like strenght distributions. Such result, in fact, is within the NUMEN project reach as suggested by recent heavy-ion SCE reaction theory [49]. In this view, the main limitation is represented by the possible contamination of SCE data due to the competing transfer mechanisms. For this reason such contribution has to be investigated in detail, in order to ensure that it is not dominant and can be neglected.

Chapter 3

The ^{20}Ne + ^{116}Cd reaction system at 306 MeV with the MAGNEX spectrometer

The ^{20}Ne + ^{116}Cd experiment at 15.3 AMeV was performed at INFN-Laboratori Nazionali del Sud in Catania, Italy. The K800 Superconducting Cyclotron (CS) accelerator [72] provided the ^{20}Ne beam at 306 MeV, with high energy resolution (1/1000) [88] and low emittance ($\sim 2\pi$ mm$\times$mr)[89]. The MAGNEX magnetic spectrometer was used to detect and momentum analyze the ejectiles produced in the nuclear collisions. In particular, according to the NUMEN project aims discussed in Chapter 2, the interesting quasi-elastic reaction channels are:

- elastic and inelastic scattering (^{20}Ne, ^{20}Ne);
- one-proton stripping (^{20}Ne, ^{19}F);
- two-proton stripping (^{20}Ne, ^{18}O);
- one-neutron pick-up (^{20}Ne, ^{21}Ne);
- two-neutron pick-up (^{20}Ne, ^{22}Ne);
- Single Charge Exchange (^{20}Ne, ^{20}F);

- Double Charge Exchange (^{20}Ne, ^{20}O).

as sketched by Fig. 3.1.

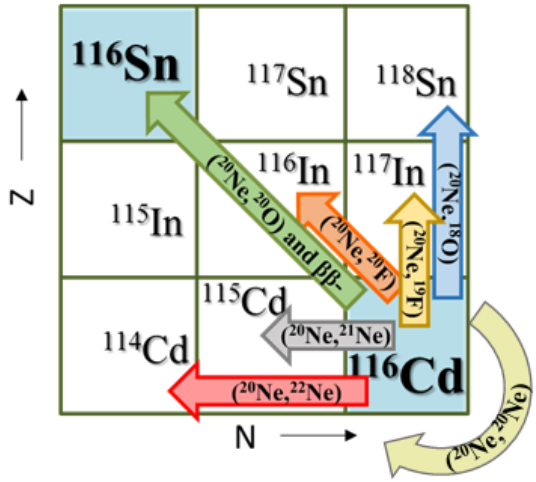

Figure 3.1: Schematic drawing of the interesting reaction channels for the ^{20}Ne+^{116}Cd system

In the present Thesis, particular attention will be devoted to ^{116}Cd(^{20}Ne, ^{20}O)^{116}Sn Double Charge Exchange (DCE) reaction as well as the ^{116}Cd(^{20}Ne, ^{20}F)^{116}In Single Charge Exchange (SCE) channel and the competing ^{116}Cd(^{20}Ne, ^{19}F)^{117}In one-proton and ^{116}Cd(^{20}Ne, ^{18}O)^{118}Sn two-proton transfer. In the next Sections, the experimental set-up arranged to perform the experiment, the MAGNEX spectrometer and its Focal Plane Detector (FPD) will be described.

3.1 The Experimental Set-Up

In the experiment, a $^{20}Ne^{10+}$ beam was delivered up to the MAGNEX scattering chamber. Before starting the beam transport, an accurate optical alignment - with an accuracy of $\sim$ 0.1 mm - was performed thanks to the use of bubble levels, thus ensuring that the beam hit the target at the spectrometer object point. During the preliminary transport, moreover,

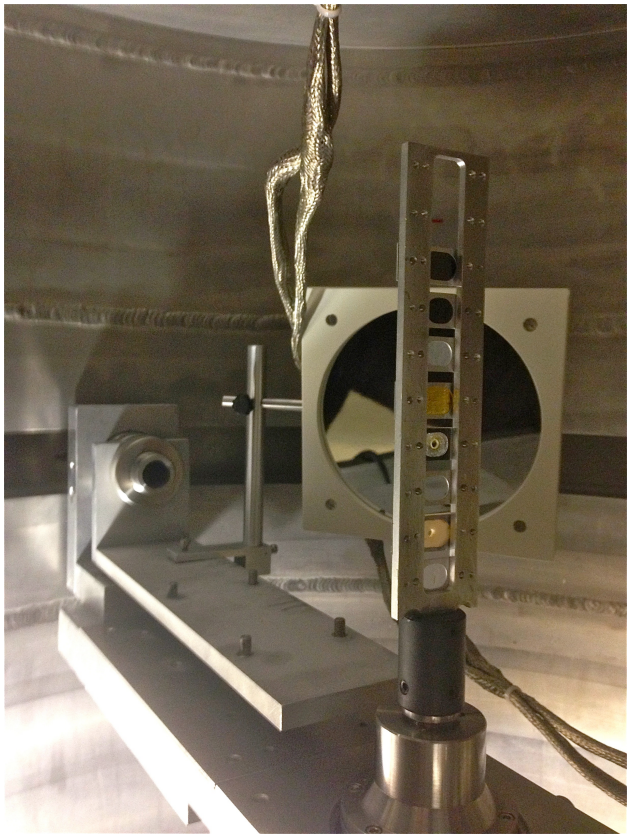

Figure 3.2: Inside view of the scattering chamber. The target ladder, the mirror and the beam line pipe are visible.

the beam spot was periodically checked by several alumina scintillating targets located along the transport line and inside the scattering chamber. In particular, the beam image on the last one - characterized by a circular 3 mm diameter hole and mounted on the target ladder - was observed through a mirror-camera system to estimate the beam spot dimension at the spectrometer object point. A picture of the scattering chamber interior is shown in Fig. 3.2. The resulting $\sim$ 3 mm diameter beam spot size guarantees a good matching with the spectrometer optical properties.
The target - produced at the LNS chemical laboratory - was a 1370 $\pm$ 140 μg/cm^2 rolled 96% pure ^{116}Cd foil followed by a 990 $\pm$ 100 μg/cm^2 natural C foil. The latter was included to minimize the contribution due

to lower charge states generated by the charge redistribution in the primary target. In fact, in the present $^{20}Ne^{10+}$ + ^{116}Cd experiment, as well as all the other NUMEN ones that use the $^{20}Ne^{10+}$ as incident beam, the magnetic rigidity of the $^{20}Ne^{10+}$ beam ions results lower than that of the ejectiles of interest. Thus, whatever is the magnetic field set, it will be bent more than the others thus making possible to guide them outside the FPD. However, the interaction of the beam with the electrons of the target material, produces also beam components characterized by charge states lower than 10+, namely $^{20}Ne^{9+}$ and $^{20}Ne^{8+}$, having magnetic rigidities similar to some of the ions of interest. Such low charge state components of the main fully-stripped beam have typically an intensity of the order of 10^{-3} (for the 9^{+}) and 10^{-5} (for the 8^{+}) with respect to the fully stripped 10+ incident beam ions [90]. Thus, they represents a huge background even for beam intensity of few enA. At forward angles, in fact, the elastic scattering on the target by such $^{20}Ne^{9+}$ and $^{20}Ne^{8+}$ beams produces high counting rate at the focal plane. The use of an appropriate second target located downstream the isotopic one and acting as a post-stripper is a feasible solution to minimize the amount of $^{20}Ne^{9+}$ and $^{20}Ne^{8+}$ produced, conveniently modifying the beam charge distribution. To this aim, a systematic study of different materials to be exploited as post-stripper has been performed within the NUMEN project [91], concluding that material containing Carbon - as the one used in the present experiment - are very efficient to reduce the lower charge state contributions. However, such solution reduces only partially this background so that part of the FPD was shielded by a system of movable aluminum screens, as shown in Fig. 3.3, to intercept the undesired $^{20}Ne^{9+,8+}$ ions. This solution, however, partially reduces the full FPD energy acceptance.

The average beam intensity during the experimental run was about 9-10 enA with maximum values not exceeding 15 enA, corresponding to the limit tolerable rate accepted by the MAGNEX FPD in the present configuration. The beam intensity was measured by a 8 mm diameter Faraday cup, mounted inside the scattering chamber 15 cm downstream the target ladder along the beam direction. An electron suppressor, polarized at -200 V, was mounted at the entrance hole of the Faraday cup in order to enhance the efficiency of the charge collection.

The ejectiles were momentum analyzed by the MAGNEX spectrometer.

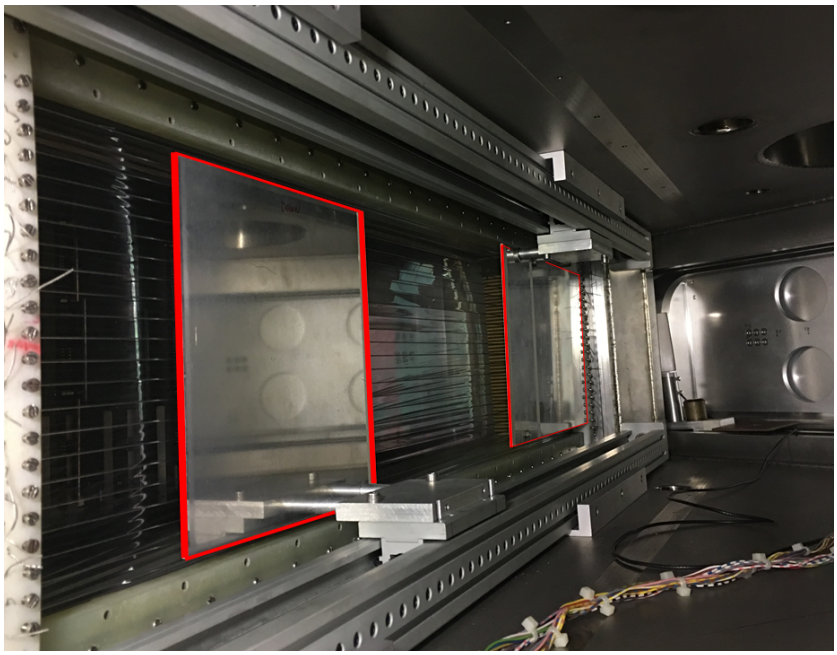

Figure 3.3: Picture of the movable screen system (highlighted by the red borders) mounted at the entrance of the gas filled FPD to stop the elastically scattered $^{20}Ne^{9+,8+}$ ions.

Its optical axis was centered at θ_{lab}^{opt} = +8° in the laboratory reference frame. The MAGNEX angular acceptance was set to [-5.16°, +6.3°] horizontal and [-6.5°, +-6.5°] vertical corresponding to a total solid angle of $\Delta\Omega$ ∼45 msr in the scattering angular range $3° < \theta_{lab} < 14°$.

3.2 The MAGNEX Large Acceptance Spectrometer

The MAGNEX large acceptance magnetic spectrometer installed at the INFN-LNS is a unique system for heavy-ion nuclear physics. The apparatus, in fact, combines high angular, mass and energy resolution with large phase-space acceptance, both in momentum and angle [92]. Originally designed to investigate nuclear reaction with radioactive beams, its use was extended to several different nuclear structure and reaction mechanisms studies [93, 94, 95, 96, 97, 98]. In particular, it had shown to be effective in processes characterized by low yields. The achieved high performance are the result of the interplay of innovative designs of the magnetic elements and the adoption of specific techniques to determine the phase-space parameters after the collision. MAGNEX is a Quadrupole-Dipole spectrometer consisting of quadrupole magnet focusing in the non-dispersive - vertical - direction and a 55° dipole magnet providing the dispersion and focus strength in the dispersive - horizontal - direction, obtained rotating the entrance and exit dipole boundaries of 18°. The two magnets are followed by the Focal Plane Detector (FPD) to detect the emitted ions. The accepted magnetic rigidities range from 0.2 to 1.8 Tm, corresponding to energies ranging from 0.2 to 40 AMeV depending on the ion mass and charge. The main MAGNEX optical properties and characteristics are reported in Tab. 3.1.

3.2.1 Reference Frame and Aberrations

The typical way to describe the motion of a charged particle beam is based on the choice of one of them as a reference. Its momentum and path through the magnetic elements are the reference momentum p_0 and trajectory t_0, respectively. The generic particle position and momentum

Table 3.1: Main optical characteristics of the MAGNEX spectrometer.

Optical characteristics	Values
Maximum magnetic rigidity (Tm)	1.8
Maximum solid angle (msr)	50
Horizontal angular acceptance (mr)	-90, +110
Vertical angular acceptance (mr)	$\pm$123
Momentum acceptance (δ)	-0.14, +0.1
Central path length (cm)	596
Momentum dispersion (cm/%)	3.68
Focal plane rotation angle (degrees)	59.2
Focal plane length (cm)	92
Focal plane height (cm)	20

are thus defined comparing them to the reference ones. Along the reference trajectory, a longitudinal or t axis lying in the direction of the reference momentum is defined, while the two transverse axes x and y are chosen perpendicular to it, thus composing a right handed reference frame (x, y, t). In the latter, the particle momentum is decomposed in p_x and p_y components along the x and y directions and the fractional deviation δ from the reference momentum, defined as δ = (p - p_0)/p_0. It is more convenient to consider the quantities x$'$ = p_x/p_t and y$'$ = p_y/p_t, where p_t is the longitudinal momentum component along the reference trajectory. Since p_x and p_y are typically small if compared to p_t, x' and y' can be approximated by the horizontal θ and vertical ϕ angles with respect to the reference trajectory. To complete the phase-space coordinate set, additional parameters are needed: the transverse distances from the central trajectory, x and y. Summarizing, each particle is described by the observables set $P = (x, \theta, y, \phi, \delta)$.

As the charged particle moves through the spectrometer, its final position $P_f = (x_f, \theta_f, y_f, \phi_f, \delta_f)$ results connected to the initial one $P_i = (x_i, \theta_i, y_i, \phi_i, \delta_i)$ as

$$M : P_i \rightarrow P_f \tag{3.1}$$

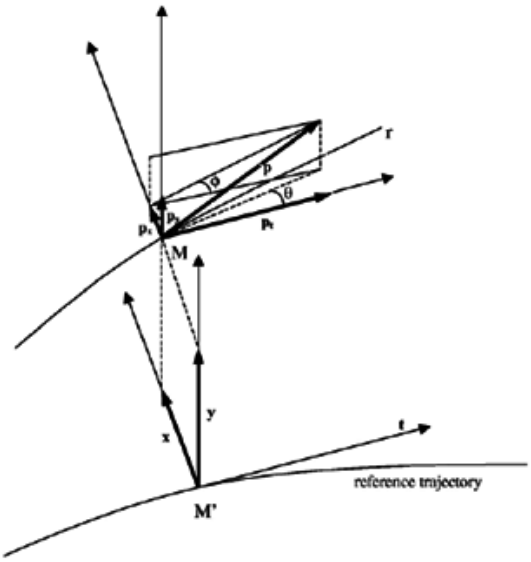

Figure 3.4: Reference frame adopted to describe the motion in a magnetic spectrometer

describing a general non-linear transport relation, characteristic of the particular optical system. More explicitly, it can be written as

$$\begin{cases} x_f = M_1(x_i, \theta_i, y_i, \phi_i, \delta_i) \\ y_f = M_2(x_i, \theta_i, y_i, \phi_i, \delta_i) \\ \theta_f = M_3(x_i, \theta_i, y_i, \phi_i, \delta_i) \\ \phi_f = M_4(x_i, \theta_i, y_i, \phi_i, \delta_i) \\ \delta_f = \delta_i \end{cases}$$

where the last equality expresses the conservation of the ion momentum modulus in a magnetic field in the absence of degrading materials. The previous equations can be expanded in Taylor series around the reference axis obtaining the so-called aberration expansions. In fact, exploiting the tensor notation, they can be rewritten as

$$x_f = \sum_k R_{jk} x_k + \sum_{kl} T_{jkl} x_k x_l + ... \tag{3.2}$$

where the coefficients at second T_{jkl} and higher order are typically referred as aberrations, since they determine deviations from the ideal first order optical properties.
The crucial issue of aberrations is faced in MAGNEX using both hardware and software solutions. In fact, the minimization of some important aberration terms have been obtained with a carefully shaping of the magnets - as in the case of the dipole entrance and exit Effective Field Boundaries (EFB) - as well as adopting other specific solutions [99]. As an example, the FPD entrance surface is rotated of θ_{tilt}=59.2° with respect to the central trajectory in order to compensate the T_{126} term. The aberration formalism, moreover, allows to construct the transport matrix M of a complex magnetic system, composed by several elements, as the product of the matrices of each magnet in a multistage approach. Such strategy has been implemented in the COSY INFINIY software [100]. The code is based on a fully algebraic approach to determine the ion trajectory inside the spectrometer [101]. It requires an accurate knowledge of the geometric and magnetic structure [102, 103, 104, 105], the use of algebraic algorithms to solve the high-order transport equations [106] and the precise measurement of the ions positions and directions at the focus as returned by a suitable FPD. More details about such ray-reconstruction technique will be provided in the following.

Creation of the direct and inverse transport maps

The ray-reconstruction procedure starts with the creation of a transport map which describes the evolution of the phase space parameters from the target point P_i to the focal plane P_f expressed by the operator M in eq. (3.1). Such task is achieved using the COSY INFINITY code, which solves eq. (3.1) ion by ion up to the 10^{th} order adopting Runge Kutta integration technique based on the formalism of the differential algebra [106]. The COSY INFINITY input includes the geometry of the spectrometer - distances between the magnetic elements, length of the drift space and slits defining the solid angle - the location of the FPD and the values of the quadrupole and the dipole magnetic fields, which are described as three-dimensional Enge functions. An extensive 3D mapping of the fields and interpolation procedure are crucial for the overall performance of the

technique. Special attention is required at the magnet fringes where the magnetic fields may change rapidly. Thus, important input parameters to create the transport matrix are the EFB of the dipole magnet, which are mathematically represented as 5^{th} order polynomials. In fact, there is a weak dependence of the shape of the entrance and exit EFB on the magnetic field strength and therefore they have to be carefully optimized for each magnetic setting looking at the resulting transport simulations. More details about the procedure will be given in Section 4.1.4.
An iterative procedure implemented in COSY INFINITY allows to construct the inverse transport map M^{-1} up to the same order. In such a way, if the appropriate positions and directions of the detected ions are determined - i.e. are measured with good accuracy at the focal plane - the full trajectories can be reconstructed back to the reaction target by applying the inverse map M^{-1} to the measured phase space parameters $P_f = (x_f, \theta_f, y_f, \phi_f, \delta_f)$. As a result, each initial phase space parameter is given by

$$\begin{cases} x_i = M_1^{-1}(x_f, \theta_f, y_f, \phi_f, \delta_f) \\ y_i = M_2^{-1}(x_f, \theta_f, y_f, \phi_f, \delta_f) \\ \theta_i = M_3^{-1}(x_f, \theta_f, y_f, \phi_f, \delta_f) \\ \phi_i = M_4^{-1}(x_f, \theta_f, y_f, \phi_f, \delta_f) \\ \delta_i = \delta_f \end{cases}$$

Finally, from the reconstructed $(x_i, \theta_i, y_i, \phi_i, \delta_i)$ quantities, the ejectile momentum vector can be deduced. The reconstruction quality depends on the accuracy of the phase-space parameter measurements. The latter are provided by the FPD, as described in the next Section.

3.3 The MAGNEX Focal Plane Detector

The MAGNEX FPD is a three dimensional gas-filled tracker detector completed by a wall of 60 silicon pad detectors. It measures the horizontal and vertical positions and angles of each incident ion along its trajectory as well as the energy losses in the gas region and the residual energy released in the silicon detectors. It is placed 1.91 m after the exit pole face

of the MAGNEX dipole, rotated by θ_{tilt}=59.2° with respect to the central trajectory and mounted on a movable carriage that can translate of $\pm$0.08 m along to the spectrometer optical axis, in order to match the detector position to different focus conditions [99]. The FPD design and operation principle are described in details in Ref. [92], in the following the main features are reported.

3.3.1 Design

The sensitive gas region, filled with 99.95% pure Isobutane (C_4H_{10}) at a pressure value typically ranging from 10 to 50 mbar depending on the experiment, is separated by the vacuum one by a 1.5 μm Mylar window. The latter is supported by twenty 0.9 mm diameter silicon coated stainless multistrand wires, horizontally arranged and spaced 10 mm each other. Despite introducing a 12% efficiency loss, such wires are extremely useful to perform the vertical coordinate calibration, representing an absolute references in the vertical direction, as illustrated in Sec. 4.1.1.
The drift chamber active volume measures 1360$\times$200$\times$96 mm^3. The cathode plate is located at the basis, usually supplied by -900 V to -1500 V, while, on the top, a Frisch grid connected to the ground and composed by 10 gold-plated tungsten wires 50 μm in diameter each and spaced 5 mm between centers is present. The electric field uniformity in such region is guaranteed by 41 rectangular rings parallel to the cathode, spaced 5 mm one from the other and composing a partition grid.
The proportional wires DC$_i$ ($i = 1, ..., 4$) and PC are placed 2 cm above the Frisch grid, one for each drift chamber. They are 20 μm diameter golden tungsten wires, typically supplied between +600 - +1300 V, composing the proportional counter section. A set of 224 anode pads orientated along the spectrometer optical axis is located 5 mm above each DC$_i$ ($i = 1, ..., 4$) proportional wire. Such pads - 8 mm long and 5.9 mm wide and separated by 0.1 mm from neighbor ones - measure the induced charge collected by the wires due to the electron avalanches produced in the multiplication region. A part of the anode systems is shown in Fig. 3.5.
The silicon pad detectors completely stop the incoming ions. They present an active area of 70$\times$50 mm^2 each, a thickness of 1000 μm and are ar-

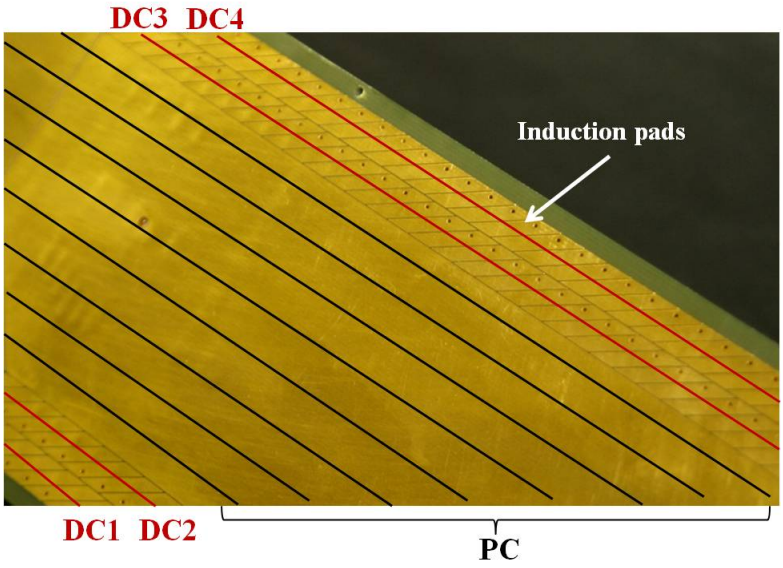

Figure 3.5: Picture of the FPD induction plate showing the segmented pads and the DC_i ($i = 1, ..., 4$) and PC proportional wires.

ranged in 20 columns of 3 detectors each mounted orthogonally to the spectrometer optical axis. A schematic representation of the FPD in reported in Fig 3.6.

3.3.2 Operating Principle and Electronic Read-out

The MAGNEX FPD was designed to measure the ion phase-space parameters and to perform the particle identification. The latter, as described in Section 4.1.2, is performed combining the measurements of the projectile residual energy E_{resid}, energy losses ΔE_i ($i = 1, ..., 4$) in the drift section and the horizontal position resulting by the induction pad system.
The detector data acquisition system is based on standard VME modules for data-encoding. The E_{resid} measurement is provided by the silicon pad detector signal, read-out by a charge sensitive pre-amplifier (5 mV/MeV) coupled to a 16-channel shaping amplifier and digitally converted by a peak-sensitive ADC. A similar electronic read-out chain is adopted to acquire the energy loss signals ΔE_1, ΔE_2, ΔE_3, ΔE_4, ΔE_{PC} generated in dif-

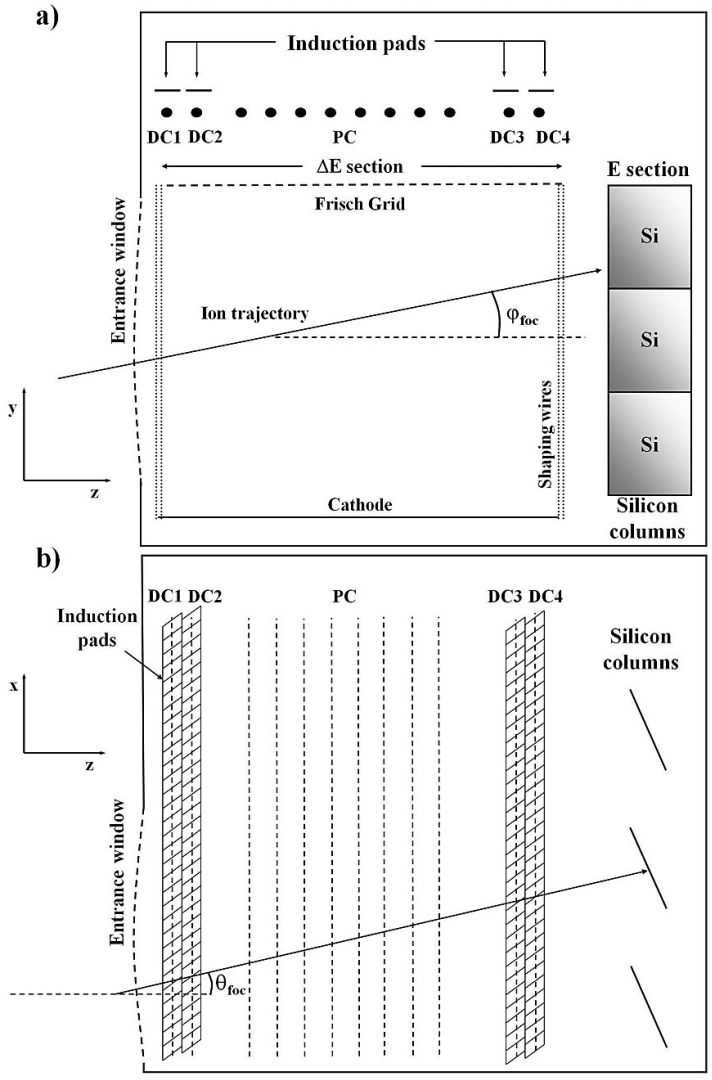

Figure 3.6: Schematic view of the MAGNEX Focal Plane Detector: a) side view; b) top view.

ferent portions of the FPD by the proportional wires DC_i and PC. In the multiplication region beyond the Frisch grid, due to the steeply growth of the electric field, the production of secondary electrons takes place with a multiplication factor of about 100-200 for each drifted primary electron. The signals produced by such avalanches, proportional to the energy loss in the gas drift region by the ion, are collected and shaped by 200 mV/MeV (silicon equivalent) charge sensitive pre-amplifiers [107] and transmitted to a shaping amplifier. The final shaped output is digitally converted by a peak-sensitive ADC.

The ion track horizontal positions X_1, X_2, X_3, X_4 at the FPD result from the signal induced by the electron avalanche on the closest induction pads. Such signals are pre-amplified and shaped by an analog multiplexed read-out system based on 16 channels GASSIPLEX chips [108] mounted on the upper side of the induction pads board in the gas environment [109]. The mutiplexed signals from each of the four chains are read-out and digitally converted by a CAEN digitizer (V1724) module. A dedicated algorithm [110] is then used to extract the center of gravity of the charge distribution at each DC_i section. By exploiting the regular geometric pattern of the segmented electrode, it is possible to obtain a unique correspondence between the measured centroids and the absolute horizontal positions X_1, X_2, X_3, X_4 in the MAGNEX reference frame. In this way, four positions are independently determined, allowing the extraction of the ion track horizontal position and angle at the spectrometer focal plane. Such parameters, which are referred to the spectrometer optical axis as X_{foc} and θ_{foc} are the ones adopted in the ray-reconstruction procedure.

The ion vertical position and angle are obtained through the electron drift time measurements in the drift gas region as the time interval between the logic signal generated by the silicon detectors (START) and the avalanche signals provided by the proportional wires (STOP), using four TAC+ADC read-out chains. Since the electron drift velocities are almost constant for fixed gas pressure and electric field - typically ranging between 3 and 5 cm/μs - the time measurements allows to derive the vertical positions Y_1, Y_2, Y_3, Y_4 along the trajectory. Such vertical coordinates, however, need an absolute calibration to be correctly expressed in the optical reference frame, described in Section 4.1.1. Their projection on the focal plane and

the angle with respect to the optical axis represent the vertical position (Y_{foc}) and angle (ϕ_{foc}) of the ion track.

3.3.3 Data Acquisition and Trigger

The acquisition system has been conceived assuming that the events multiplicity on the FPD is equal to one, i.e. that for each event only one silicon pad detector is hit.
The silicon signals are processed by a constant fraction discriminators (CFD) whose logic outputs are sent to a OR logical unit. The total OR of the 60 signals coming from the silicon detectors is used as the master acquisition trigger, so it is herein after referred to as Master_trigger. It is sent to a V1495 General Purpose VME board mounting a FPGA programmable unit. The acquisition starts only when the Master_trigger signal is active. The acquisition program, in fact, running on external workstations, operates in "polling" i.e. research cyclically the digital level of the Master_trigger signal.
During the acquisition time the V1495 remains inhibited to new input signals, returning a logical output (Master_live) signal only when the acquisition returns free. The Master_live also activates the gate signal for the ADCs. Then, the conversion between the standard VME and PC is obtained using an Optical Link Bridge, controlled by a PCI mounted on the workstation.
The live time is measured in each experimental run using VME scalers [CAEN MOD. V820]: the Master_trigger signal, converted from NIM to ECL standard to be accepted by the scaler module, is sent to a channel whereas the Master_live signal is sent to another one. In this way, two event counters are saved by the scaler and they are read by the acquisition program at the end of each run: a number of "raw" events which represents the total number of Master_trigger signals (FPD.raw) and a number of "live" events, given by the Master_live signals when the acquisition has actually read the event (FPD.live). The ratio FPD.live/FPD.raw determines the live time coefficient from which the dead one is deduced and then used to correct the efficiency in the cross section estimation, as described in Section 4.1.5.

Table 3.2: Ground state (g.s.) position along the focal plane, in terms of relative momentum δ, of each investigated reaction.

Reaction	δ (g.s.)
^{116}Cd(^{20}Ne, ^{20}O)^{116}Sn	-0.006
^{116}Cd(^{20}Ne, ^{20}F)^{116}In	-0.007
^{116}Cd(^{20}Ne, ^{19}F)^{117}In	-0.027
^{116}Cd(^{20}Ne, ^{18}O)^{118}Sn	-0.050

3.3.4 Experimental Settings

In the examined experiment, the FPD was filled with the Isobutane gas at 15.25 mbar pressure. The proportional wires DC_1, DC_2, DC_3, DC_4, PC and the cathode were supplied by a voltage of +730 V and -1100 V, respectively. The silicon detectors were supplied by a voltage equal to their nominal depletion value +20% in order to ensure a fully-depleted configuration. The quadrupole and dipole fields were set using the COSY-Setup software, specifically conceived for searching the best value to set-up the MAGNEX magnetic fields. In particular, when the kinematic parameters of the examined reaction and the desired relative fractional momentum position (δ) of a specific state are given as input, the COSY-Setup code returns the corresponding setting of the magnetic fields.The values of current to set in the magnet power supply are also returned by the program as output, adopting a calibration function. The magnetic fields are then measured by: one NMR probe inside the dipole and the average value returned by four Hall probes located in the quadrupole.
In the described experiment, the magnetic settings were constrained by the requirement to include, along with the DCE reaction also the competing channels in an energy range as wide as possible which includes their ground states, see Fig. 3.7. Thus, DCE, SCE, 1p- and 2p-transfer reactions were measured adopting a unique magnetic setting: Bρ = 1.399606 Tm, Bq = -0.7322 T. The ground state (g.s.) fractional relative momenta δ on the FPD for the different reaction channels are reported in Tab. 3.2.

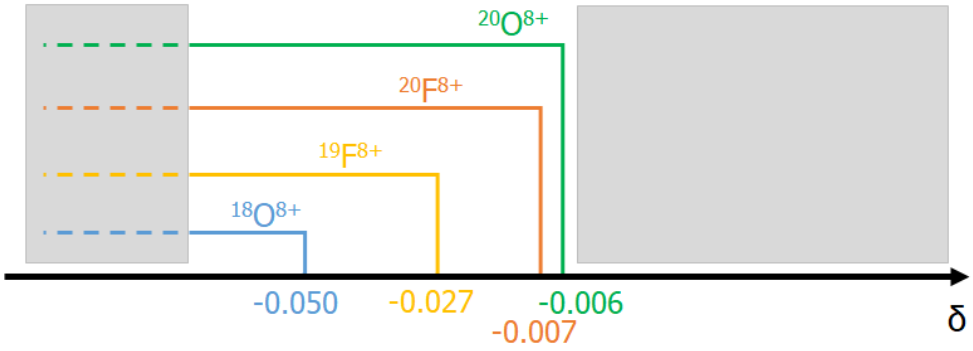

Figure 3.7: Schematic drawing, in relative momentum δ, of the interesting reaction channels for the ^{20}Ne+^{116}Cd system with the adopted magnetic setting. The grey rectangles represent the FPD regions covered by the aluminum shields mounted before its entrance.

Chapter 4

Data Analysis and Experimental Results

The present Chapter is devoted to the detailed description of the data reduction procedure, the outline of the reconstruction and analysis techniques and the presentation of the experimental results. The first point includes the calibration of the measured phase-space parameters as well as the particle identification in atomic number, mass number and charge of the detected ions. The construction of the spectrometer transport map, its optimization and inversion represent the following steps in the analysis of the investigated events, finally providing the ion kinetic energies and scattering angles in the laboratory reference frame. An experimental method to estimate the minimum cross section measurable by the MAGNEX spectrometer is presented and applied for the first time.
Finally, the differential cross section distributions in energy and angle for the investigated reaction channels are deduced.

4.1 Data Reduction

The data reduction procedure - hereafter described considering the ^{116}Cd (^{20}Ne, ^{20}O)^{116}Sn DCE reaction - involves many steps. An accurate calibration, in the spectrometer reference frame, of the ejectile horizontal and vertical positions measured by the FPD is needed to determine the input

parameters of the 10^{th} order ray-reconstruction procedure. The ions must be first identified - in atomic number (Z), mass number (A) and charge state (q) - and their measured phase-space parameters analyzed to correctly perform the ray-reconstruction procedure which finally returns ion by ion their dynamical variables.

4.1.1 Calibration of Horizontal and Vertical positions

As described in Section 3.3, four horizontal positions X_1 , X_2, X_3, X_4 for each ion track are deduced by the FPD segmented read-out board placed above each DC_i ($i = 1, ..., 4$) wire. A relative calibration of the induction pads response is performed before extracting the X_i parameters. Pulses of different amplitudes, from 2 V to 5 V in 1 V step, produced by a precision pulse generator, are sent directly onto each proportional wire, instantly inducing the same charge in each pad. Performing a linear fit which correlates the signal amplitudes returned by each single pad with a reference one, a relative calibration of the response of the different induction pads is obtained. After such calibration procedure, the center of gravity of the charge distribution is extracted event by event, thanks to an optimization algorithm specially developed for MAGNEX detector which takes into account the large variation of the number of excited pads as a function of the ion incident angle [110]. The horizontal positions X_i are then determined in the spectrometer reference frame from the corresponding centroid positions. Since the induction pad coordinates along the optical axis Z_i are known, by exploiting the (Z_i; X_i) correlation and performing a linear fit, see Fig. 4.1, the position at the focal plane X_{foc} and the corresponding horizontal angle θ_{foc} are deduced from the fit intercept and slope, respectively.
The vertical position needs also a calibration, which has been performed adopting as a reference the "shadows" on the vertical position distributions, determined by the absorption of the ejectiles flux due to the silicon coated wires used to support the Mylar window. In fact, the vertical (Y_i) distribution shows regular minima in correspondence of the mentioned wires (see Fig. 4.2) whose absolute positions as well as their relative distances have been precisely measured by means of a bubble level. So, the final absolute calibration of the vertical coordinates are obtained by com-

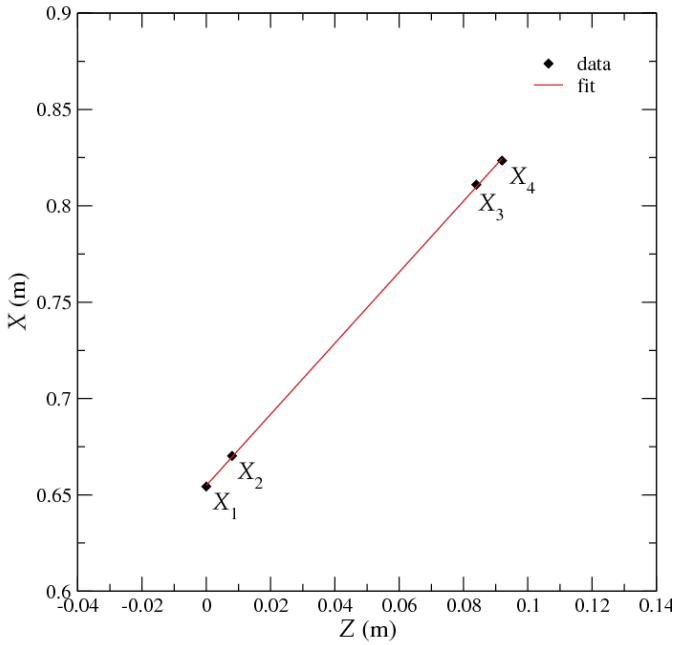

Figure 4.1: (Z_i; X_i) correlation for an ion track measured by the FPD

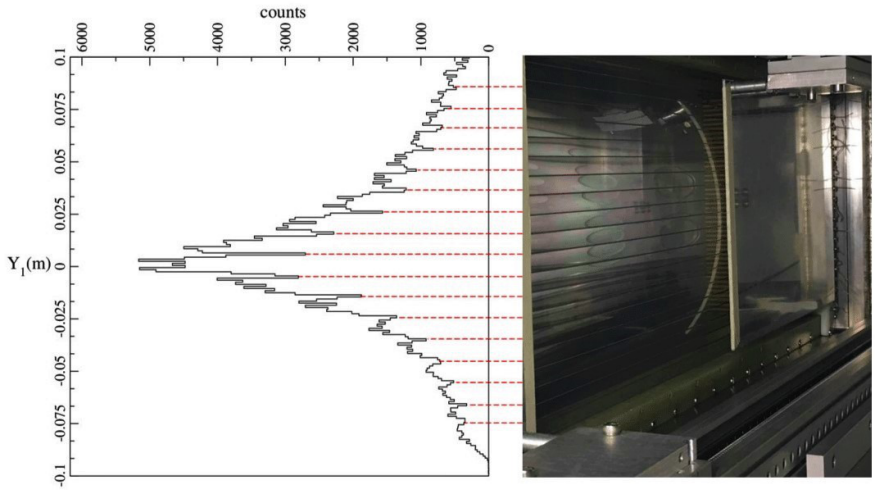

Figure 4.2: Typical Y_i spectrum without any event selection. The minima indicated by the red dashed lines correspond to the horizontal silicon coated wires used to support the entrance Mylar window, visible in the right photograph.

paring the position of the holes for each mono-dimensional Y_i spectrum with the wire absolute positions. Then, as for X_i case, the focal plane vertical position (Y_{foc}) and angle (ϕ_{foc}) are extracted event by event from the (Z_i; Y_i) correlation fit.
The X_{foc} and θ_{foc} as well as Y_{foc} and ϕ_{foc} quantities, representing the input parameters of the ray-reconstruction technique, are thus determined for each ion.

4.1.2 Particle Identification

The particle identification (PID) technique adopted in MAGNEX is described in detail in Ref. [111]. For each ion detected by the FPD, the atomic number (Z), the mass number (A) and the charge state (q) are determined. In the present case, Z is selected exploiting the correlation between the energy loss in two different portions of the FPD ionization chamber (ΔE_{DC2}; ΔE_{PC}) corrected by the path length in the gas depending

on the incident angle, namely

$$\Delta E_i^{corr} = \Delta E_i \frac{cos\theta_{tilt}}{cos\theta_{foc}} \tag{4.1}$$

where θ_{tilt} is the angle between the FPD and the plane normal to the spectrometer optical axis (θ_{tilt} = 59.2°).
A and q are deduced exploiting the correlation between the ejectile position at the focal plane in the dispersive direction (X_{foc}) and its residual energy (E_{resid}), which results proportional to the ion $\frac{\sqrt{m}}{q}$ ratio. Such representation derives from the property of the Lorentz force, which determines the trajectory of a charged particle in a magnetic field. In fact, in case of the action of a uniform magnetic field whose direction is perpendicular to the velocity vector of the particle it results

$$\mathbf{B}\rho = \frac{\mathbf{p}}{q} \tag{4.2}$$

where **B** is the magnetic field which forces the particle with charge q and momentum **p** to move on a trajectory with curvature radius ρ. In a non-relativistic approximation, the momentum is related to the kinetic energy and thus approximately, being $\Delta E_{gas} \ll \mathrm{E}_{resid}$, to the residual energy measured by the silicon detectors by a quadratic relation $p \sim \sqrt{2mE_{resid}}$. Since the curvature ($\rho$) is related to the position at the focal plane (X_{foc}), the relationship between the two measured quantities X_{foc} and E_{resid} is approximately quadratic with a proportional factor given by $\frac{m}{q^2}$

$$X_{foc}^2 \sim \frac{m}{q^2} E_{resid} \tag{4.3}$$

As a consequence, when the (E_{resid}; X_{foc}) correlation plot is represented, the trajectories of different isotopes of a given ion species result distributed on separated loci, according to their $\sqrt{\frac{m}{q^2}}$ ratios.

In the present experiment, the $^{20}O^{8+}$ ions have similar $\frac{\sqrt{m}}{q}$ ratio to $^{20}F^{8+}$ and $^{20}Ne^{8+}$ ones, being 0.55907, 0.55901 and 0.55891 respectively. As a consequence, the events associated to the detection of such ions share almost the same position in the (E_{resid}; X_{foc}) correlation plot, resulting indistinguishable. Thus, a first selection was applied in the (E_{resid}; X_{foc}) plot

region where all and only the three mentioned ions are present. Then, looking at the (ΔE_{DC2}; ΔE_{PC}) correlation gated by this first selection, is possible to identify in Z the $^{20}O^{8+}$ ions as shown by the contour drawn in Fig. 4.3(a). Finally, exploring the (E_{resid}; X_{foc}) correlation gated by the (ΔE_{DC2}; ΔE_{PC}) selection, the final unambiguous identification of the $^{20}O^{8+}$ in A and q is achieved as shown in Fig. 4.3(b). Therefore, adopting the logic AND condition between the two described topological selections, represented by the two contours shown in Fig. 4.3, the $^{20}O^{8+}$ PID is accomplished. A similar procedure to that just described was used to identify the other ejectiles of interest, namely the $^{20}F^{8+}$, the $^{19}F^{8+}$ and the $^{18}O^{8+}$.

Thanks to the achieved resolution - $\frac{1}{160}$ in A and $\frac{1}{48}$ in Z [111] - the amount of misidentified or spurious events for the typical direct reaction channels explored in the past studies, characterized by μb to mb cross section values, was negligible. However, for the purposes of NUMEN, due to the strong suppression expected for the interesting channels, a detailed investigation of the PID capabilities becomes necessary. Such reasons have motivated the study described in detail in Section 4.2.1.

4.1.3 Focal Plane Phase-Space Parameters

Once the ion identification procedure is completed, the final phase-space parameters $(X_{foc}, \theta_{foc}, Y_{foc}, \phi_{foc})$ for the selected events are analyzed in detail, providing information about the achieved horizontal and vertical focusing conditions and the aberration effects. In a typical plot, characteristic of the final vertical phase-space, that correlates the measured vertical position (Y_{foc}) to the horizontal one (X_{foc}), a "butterfly" shape is present [112]. It indicates that the vertical trajectories are focused for a specific value of the ion momentum ($\bar{\delta}$) depending on the quadrupole and dipole fields strength. In the present case, the plot shown in Fig. 4.4, is characterized by an "half-butterfly" shape since the focusing value is reached close to the acceptance limit, considering that the X_{foc} = 0 position corresponds to the spectrometer optical axis.

For the same events, a plot of the measured horizontal angle (θ_{foc}) against the horizontal position (X_{foc}) is shown in Fig. 4.5. Since the FPD is in-

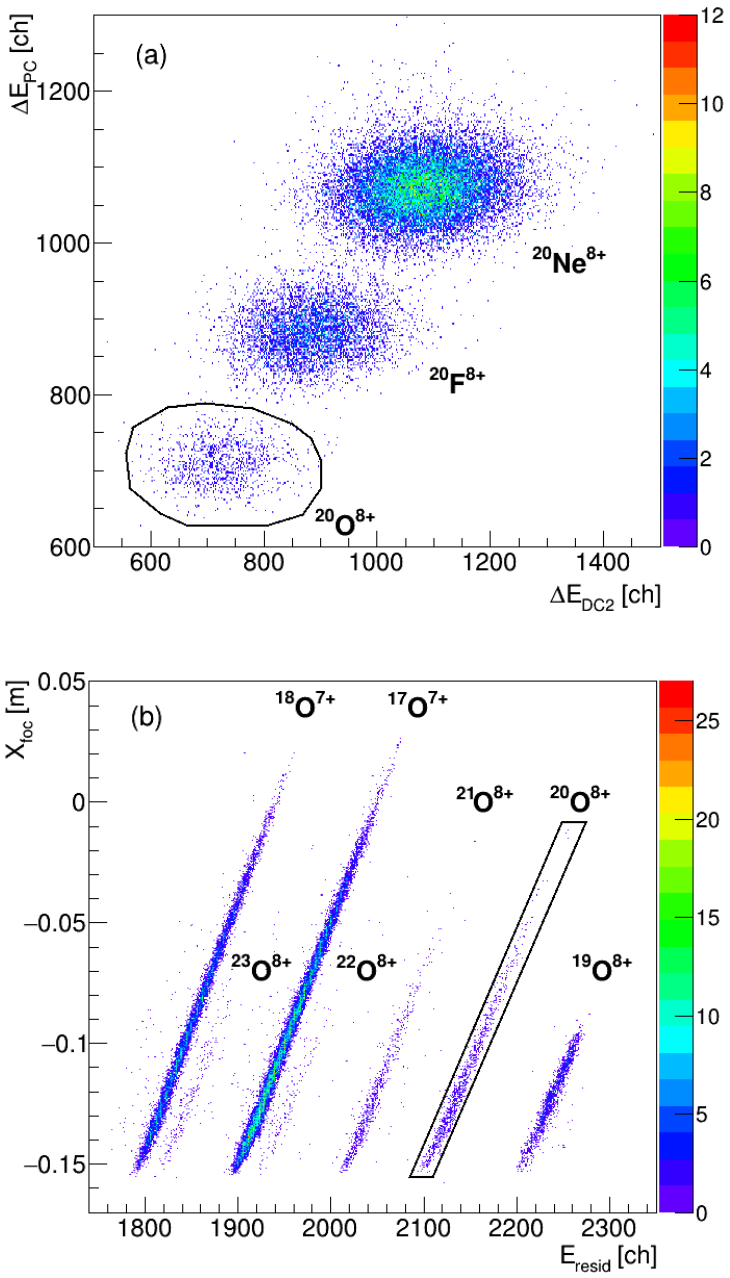

Figure 4.3: Particle identification technique adopted in the ^{20}Ne+^{116}Cd experiment. Panel (a): selection in atomic number Z between $^{20}F^{8+}$, $^{20}O^{8+}$ and $^{20}Ne^{8+}$ in the (ΔE_{DC2}; ΔE_{PC}) correlation plot. Panel (b): selection in mass number A and charge state q in the (E_{resid}; X_{foc}) representation gated by the contour drawn in panel (a) for the oxygen ions.

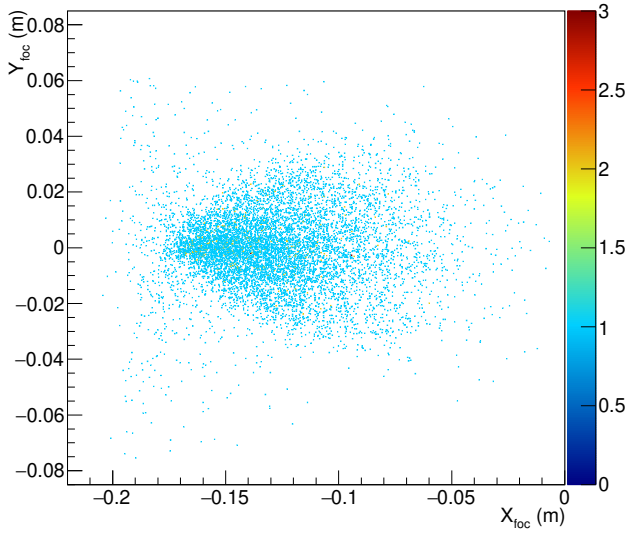

Figure 4.4: Y_{foc} vs. X_{foc} correlation plot for the selected $^{20}O^{8+}$ events of the ^{116}Cd(^{20}Ne, ^{20}O)^{116}Sn DCE reaction.

clined by 1.033 rad (59.2°) with respect to the plane perpendicular to the optical axis, the measured θ_{foc} values in the plot are distributed around such angle. Due to the limited statistics, no clear loci corresponding to isolate states populated in the ^{116}Cd(^{20}Ne, ^{20}O)^{116}Sn DCE reaction result immediately visible.

4.1.4 Ray-Reconstruction Technique

The ray-reconstruction method, described in Section 3.2.1 is a fundamental step of the data reduction, since it allows to retrieve the ejectile momentum vector at the target, thus determining the reaction Q-value and the scattering angle. The practical implementation of the procedure is organized in two steps.

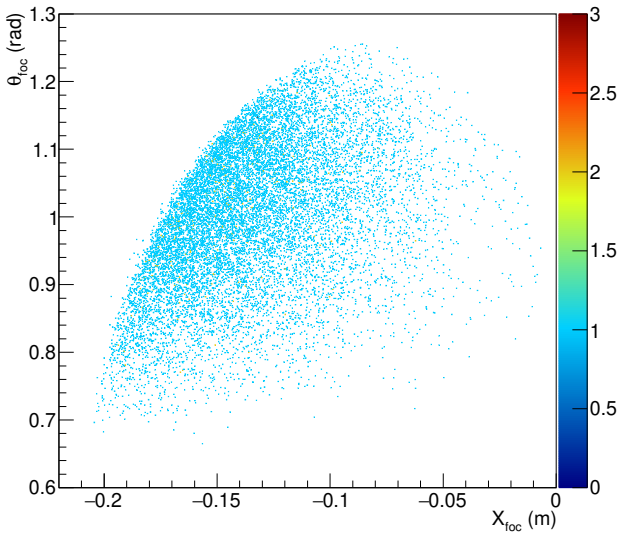

Figure 4.5: θ_{foc} vs. X_{foc} correlation plot for the selected $^{20}O^{8+}$ events of the ^{116}Cd(^{20}Ne, ^{20}O)^{116}Sn DCE reaction.

Direct transport map M

The first goal of the procedure is to generate an accurate transport map M, necessary to describe the evolution of the phase-space parameters from the target position to the focal plane. Setting the magnetic fields in the COSY INFINITY software, the direct map M is calculated up to 10^{th} order. Once it is created, an accurate check is mandatory, by comparing the experimentally measured final phase-space parameters with the simulated ones. To this purpose, a set of simulated events corresponding to the analyzed reaction - the ^{116}Cd(^{20}Ne, ^{20}O)^{116}Sn DCE in the described case - is generated by a Monte Carlo routine: the ^{20}O ejectiles connected to the excitation of ^{116}Sn excited states were tracked through the spectrometer by the application of the direct transport map. In particular, the ^{116}Sn ground (0+), 1.293 (2+), 1.756 (0+) states as well as six additional transitions at 4, 5, 6, 7, 8, 9 MeV were chosen. In the simulations, the beam energy value needs to be properly corrected to take into account the energy loss and straggling experienced both by the projectiles and

the ejectiles, since the simulation program does not include such effects. This step is separately performed assuming that the reaction occurs at the target middle depth and calculating the projectile and ejectile energy losses by means of dedicated tools like LISE++ [113] and SRIM [114].
The results of the performed simulation are shown in Fig. 4.6 for the DCE dataset shown in the previous Sections. Despite the highly non-linear aberrations, the simulated events (red points) give a rather faithful representation of the experimental data (black points) both in the horizontal (X_{foc}; θ_{foc}) and vertical (X_{foc}; Y_{foc}) phase-space representations. In particular, in order to obtain a satisfying matching with the experimental results, i.e. faithfully reproducing the shape of the high order aberrations observed in the experimental scatter plots, a very accurate modeling of the dipole Effective Field Boundaries was necessary.

Inverse transport map M^{-1}

The successive step of the ray-reconstruction procedure consists in the inversion of the direct transport map (M^{-1}) by the COSY INFINITY program and the extraction of the ion momentum vectors at the target point. These are directly related to the physical quantities of interest, such as the reaction Q-values and the scattering angles. A correlation plot of the reconstructed vertical (ϕ_i) against horizontal (θ_i) angle is shown in Fig. 4.7. It does not present the expected ideal rectangular profile defined by the four movable slits located 260 mm downstream the target and upstream the quadrupole entrance that define the solid angle acceptance. In fact, an efficiency loss effect due to a cut-off of the ejectile envelope by the spectrometer vacuum vessels is present [115]. It actually reduces the nominal solid angle acceptance to an effective value which can be estimated taking the contour of the reconstructed (θ_i; ϕ_i) representation in the laboratory frame, as shown in Fig. 4.7. Such effect will be taken into account, in particular, to correctly estimate the solid angle values of the different angular bins, needed to extract the differential cross sections distributions in energy and angle. The scattering angle in the laboratory frame (θ_{lab}) is then deduced as

$$\theta_{lab} = \arccos \frac{cos(\theta_{opt}) - sin(\theta_{opt})tan(\theta_i)}{1 + tan^2(\phi_i)} \tag{4.4}$$

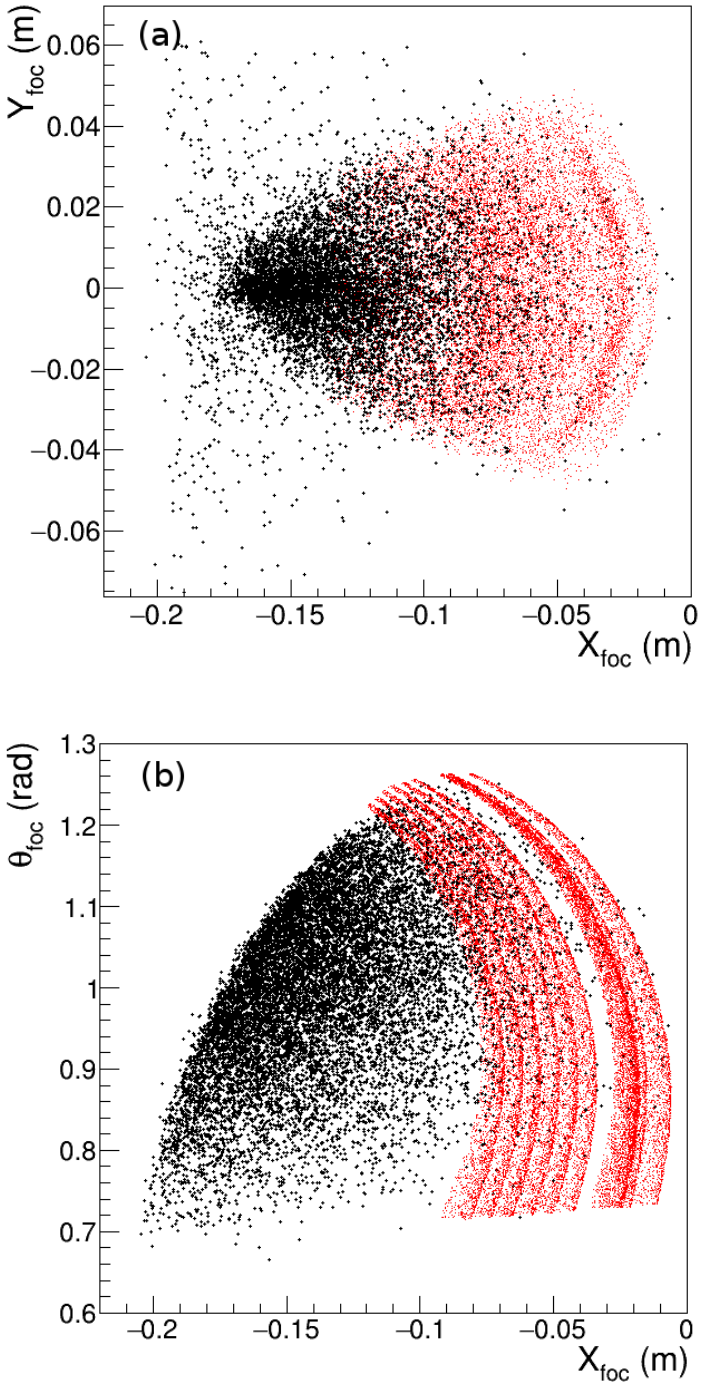

Figure 4.6: Panel (a): comparison between the DCE reaction experimental data (in black) and the simulated events (in red) in the (X_{foc}; Y_{foc}) representation. Panel (b): comparison between the experimental DCE reaction data (in black) and the simulated events (in red) in the (X_{foc}; θ_{foc}) representation.

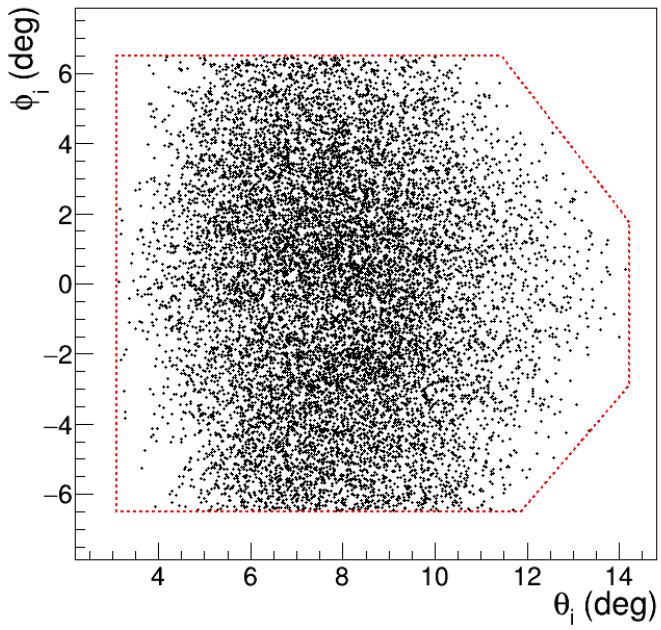

Figure 4.7: Reconstructed vertical (ϕ_i) vs. horizontal (θ_i) angle correlation plot for the $^{20}O^{8+}$ DCE ions. The red contour represents the assumed effective solid angle acceptance.

The ejectile kinetic energy is extracted from the reconstructed relative momentum δ. The corresponding Q-values or equivalently the excitation energy (E_x) are finally obtained by a missing mass calculation based on relativistic energy and momentum conservation laws, assuming a binary reaction

$$E_x = Q_0 - Q = Q_0 - K(1 + \frac{M_e}{M_r}) + E_b(1 - \frac{M_p}{M_r}) + 2\frac{M_p M_e}{M_r} E_b K cos(\theta_{lab}) \tag{4.5}$$

where M_e, M_r and M_p are the ejectile, residual and projectile masses, respectively, E_b represents the beam energy, K is the ejectile kinetic energy and Q_0 is the ground state-to-ground state Q-value.

4.1.5 Excitation Energy Spectra

In the bi-dimensional (E_x; θ_{lab}) correlation plot, the ground and the others excited states energetically resolved of the residual and ejectile nuclei should be visible as straight loci, since the excitation energy does not depend on the scattering angle for well reconstructed transitions. An example for the DCE channel is reported in Fig. 4.8. The efficiency cut around 10 MeV in excitation energy is introduced by the aluminum shields mounted at the FPD entrance, described in Sec. 3.1 and shown in Fig. 3.3, which partially reduces the spectrometer energy acceptance.
The excitation energy spectrum is obtained from the (E_x; θ_{lab}) correlation plot projecting on the vertical axis. The differential cross section distribution in excitation energy is then extracted adopting the following expression

$$\frac{d\sigma}{dE}(E_x) = 2\pi \int_{\theta_{min}}^{\theta_{max}} sin\theta d\theta \frac{N(E_x)}{N_{beam} N_{target} \Delta E t_{live} \epsilon} \tag{4.6}$$

where N(E_x) represents the number of ejectiles with the same excitation energy, N_{beam} is the number of incident ions, N_{target} is the number of scattering centers per unit surface, $\Delta\Omega$ is the solid angle covered by the FPD, t_{live} is a factor which takes into account the acquisition dead time and ϵ is an overall detection efficiency factor.

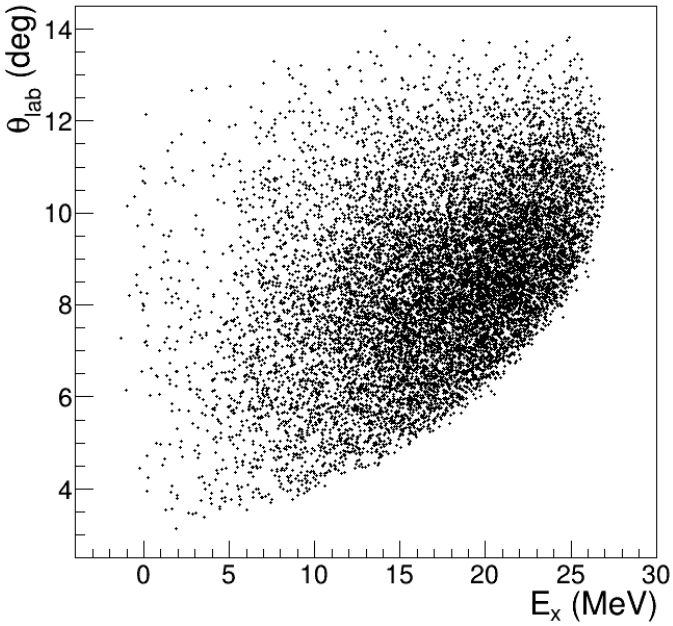

Figure 4.8: Correlation plot between the scattering angle (θ_{lab}) against the excitation energy (E_x) for the ^{116}Cd(^{20}Ne, ^{20}O)^{116}Sn DCE reaction.

The number of incident ions is retrieved integrating the beam current measured by the Faraday Cup. A digital integrator gives the total charge Q collected in each run. At the considered energy and due to the post-stripper action, the ^{20}Ne ions can be considered almost totally stripped after passing through the target. Therefore the number of the beam ions is simply evaluated as $N_{beam} = Q/Ze^-$, where Z is thus equal to ten and $e^- = 1.602 \times 10^{-19}$ C. Actually, a dedicated VME scaler measured directly the integrated charge Q_{live} corrected for the acquisition dead time, thus already including the factor t_{live} of eq. (4.6). The number of target nuclei for unit surface N_{target} is calculated from the known target density and thickness. The obtained value is $N_{target}(^{116}Cd) = 4.2 \pm 0.1 \times 10^{18}$ atoms/cm^2. The overall efficiency factor ϵ accounts for the FPD detection ($\sim$ 88%) and the ray reconstruction procedure ($\sim$ 90%) efficiencies. The latter, in particular, was evaluated as the ratio between the total number of the well reconstructed events over the total number of identified ones. Concerning the evaluation of the solid angle $\Delta\Omega$, the effective acceptance determined by the (θ_i; ϕ_i) locus reported in Fig. 4.7 was assumed. Its internal region was divided in circular rings in step of $\Delta\theta = 1^\circ$ since the solid angle values correspond to the areas defined by the interception between such rings and the effective acceptance contour.
The angular differential cross section expressed in the center of mass (c.m.) reference frame is defined as

$$\frac{d\sigma}{d\theta}(\theta_{c.m.}) = detJ(\theta_{c.m.}) \frac{N(\theta_{c.m.})}{N_{beam} N_{target} \Delta\Omega t_{live} \epsilon} \tag{4.7}$$

where, in addiction to the already described quantities, N(θ) represents the number of events detected at a fixed angle θ and $detJ(\theta)$ is the Jacobian determinant for the laboratory to center of mass frame transformation.

4.1.6 Cross Section Uncertainties

The cross section uncertainties were determined by applying the error propagation on eqs. (4.6) and (4.7).
The uncertainties on the parameters N_{beam}, N_{target}, and ϵ are common to all the experimental bins, determining an overall cross section uncertainty

estimated in about 10% which will not included in the error bars. Other sources of uncertainty come from the solid angle determination and the statistical error. The latter, due to the limited statistics consequence of the small involved cross sections, results the dominant contribution.
The error on the solid angle is estimated considering the variation of the accepted angular region caused by the uncertainties on the reconstructed vertical and horizontal angles, $\Delta\phi_i = \pm 0.4^\circ$ and $\Delta\theta_i = \pm 0.2^\circ$ respectively. In particular, the error on θ_i parameter affects more the angular bins corresponding to the border of the solid angle acceptance, which thus are typically characterized by larger error bars. The error on $N(\theta)$ or $N(E_x)$ is the statistical one ($\sqrt{N}$) obtained assuming the Poisson distribution.
In some cases, the total number of counts for specific transitions is estimated as the area of a Gaussian function adopting the formula

$$A = \sqrt{2\pi} h \sigma \tag{4.8}$$

In such cases the corresponding error is deduced by applying the error propagation law to the formula (4.8), also including the correlation terms.

4.2 Experimental Results

The Data Reduction procedure described in the previous Section was applied to all the analyzed reaction channels. The differential cross section distributions in energy and angle have been extracted. They are presented and discussed in the following.

4.2.1 ^{116}Cd(^{20}Ne, ^{20}O)^{116}Sn Double Charge Exchange reaction

The differential cross section distribution in excitation energy is shown in Fig. 4.9. In the main panel, it is presented in a reduced angular range to avoid distortions introduced by the efficiency loss effect due to the shielding screens described in Sec. 3.1 that affect the (E_x; θ_{lab}) correlation at small scattering angles and high excitation energies (see Fig. 4.8) In the inset, the differential cross section energy spectrum is reported in the full angular acceptance for the excitation energy range up to 5 MeV.

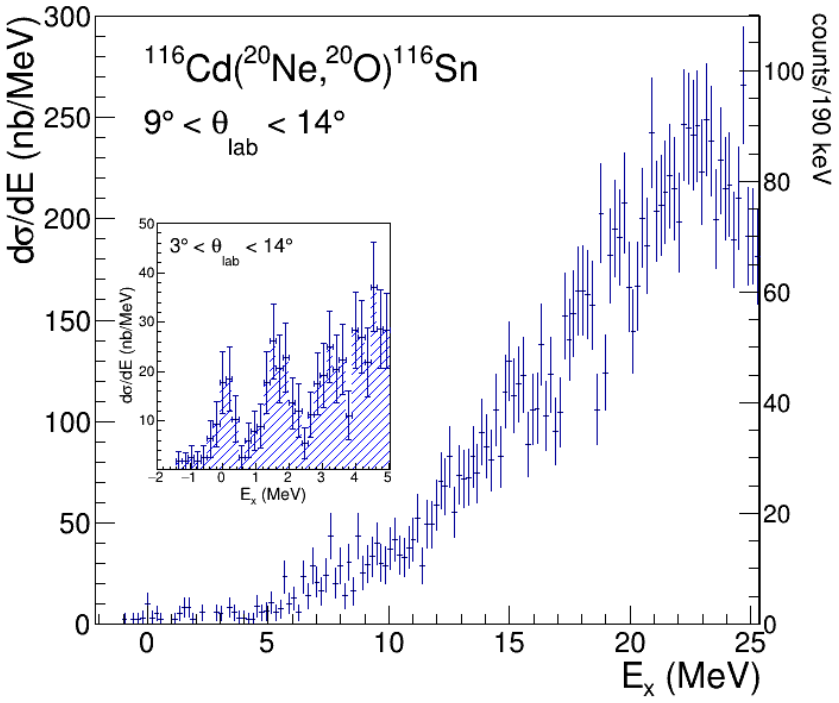

Figure 4.9: DCE differential cross section spectrum in excitation energy. In the main panel it is shown up to high excitation energy in the angular range $9° < \theta_{lab} < 14°$. In the inset, a zoomed view of the low energy part highlights the presence of three visible structures.

An isolated peak is clearly visible in the ground state region as well as two additional structures at $\sim$ 1.7 and $\sim$ 3.2 MeV. A best fit analysis of the differential cross section distribution in energy, assuming Gaussian models for the peaks and shown in Fig. 4.10, was performed in order to distinguish the transition contributions.
The g.s. transition peak (in green) presents a full width half maximum (FWHM) of $\sim$ 800 keV thus resulting well separated by the second structure corresponding to the excitation of the first low-lying state of both residual (^{116}Sn) and ejectile (^{20}Ne) nuclei. The width of the g.s. peak can be used as an estimate of the experimental energy resolution. The latter is affected by three main contributions: the spectrometer finite energy

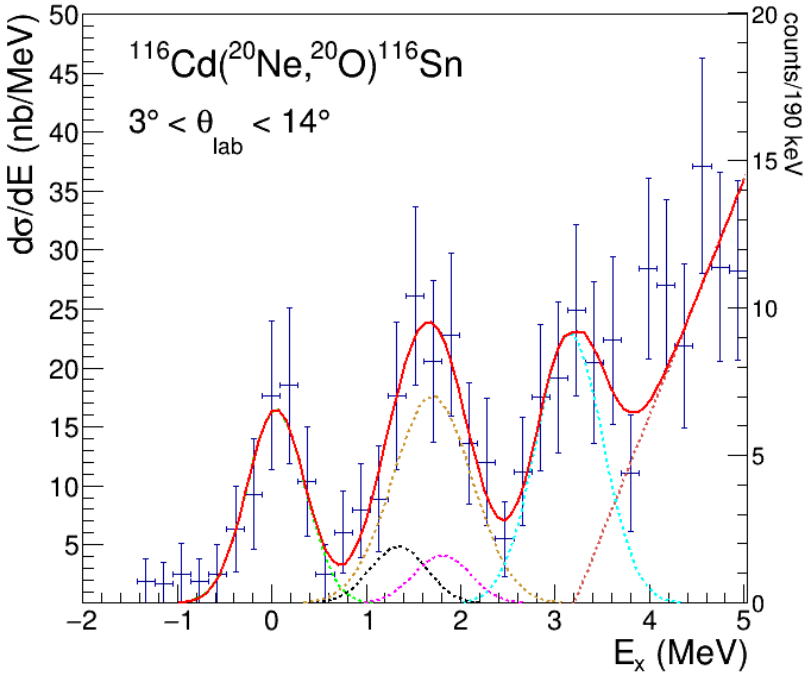

Figure 4.10: Cross section distribution analysis of the low excitation energy region for the DCE spectrum. The g.s. transition (in green) results quite well separated by the 2_1^+ (in black) and the 0_1^+ ^{116}Sn states (in magenta) as well as the 0_1^+ ^{20}O state (in yellow) which all contribute to the second peak. The structure at $\sim$ 3.2 MeV is reproduced by the combination of an additional Gaussian function (in light-blue) and a straight line reproducing the growing smooth cross section trend at higher excitation energies.

Table 4.1: List of ^{116}Sn and ^{20}O nuclear states separated for spin and parity (J^{π}) and excitation energy (E_x) up to 1.8 MeV. In the fourth column the Gaussian fit centroids are reported. The integrated ($3^{\circ} < \theta_{lab} < 14^{\circ}$) cross section values are listed in the last column.

Nucleus	J^{π}	E_x (MeV)	Fit centroids (MeV)	σ (nb)
^{116}Sn	0^+	0.00	0.045	12.73±2.37
^{20}O	0^+	0.00		
^{116}Sn	2^+	1.293	1.338	3.63±3.21
^{20}O	2^+	1.673	1.699	18.51±3.40
^{116}Sn	0^+	1.756	1.801	3.09±3.01

resolution ($\sim$ 1/1000) corresponding, in this case, to $\sim$ 300 keV; the finite beam energy spread which contributes also for about 300 keV, being about 1/1000 of the beam energy; the effect induced by the target thickness, which accounts for about 800 keV, considering the ^{20}O ions passing through 1370 μg/cm^2 target and 990 μg/cm^2 post-stripper foils.
The second visible structure in Fig. 4.10 results nicely reproduced as the sum of the ejectile and residual first low-lying states, namely the 2^+_1 (in black) and 0^+_1 (in magenta) of the ^{116}Sn and the 0^+_1 (in yellow) of the ^{20}O, thus allowing to deduce the cross sections for their individual transitions.
The third peak is modeled by the combination of a Gaussian (in light-blue) and a first order polynomial function (in orange). The latter is inserted to reproduce the growing smooth cross section trend at higher excitation energy due, in particular, to the residual nucleus high level density.
The integrated cross section values extracted by the fit analysis and the corresponding nuclear states are listed in Tab. 4.1.

The cross section angular distribution for the g.s. to g.s. (g.s. $\rightarrow$ g.s.) transition, shown in Fig. 4.11, was deduced adopting an angular bin of $\Delta\theta_{lab}$ = 2° and including all the events having excitation energy values between $\pm$0.66 MeV.

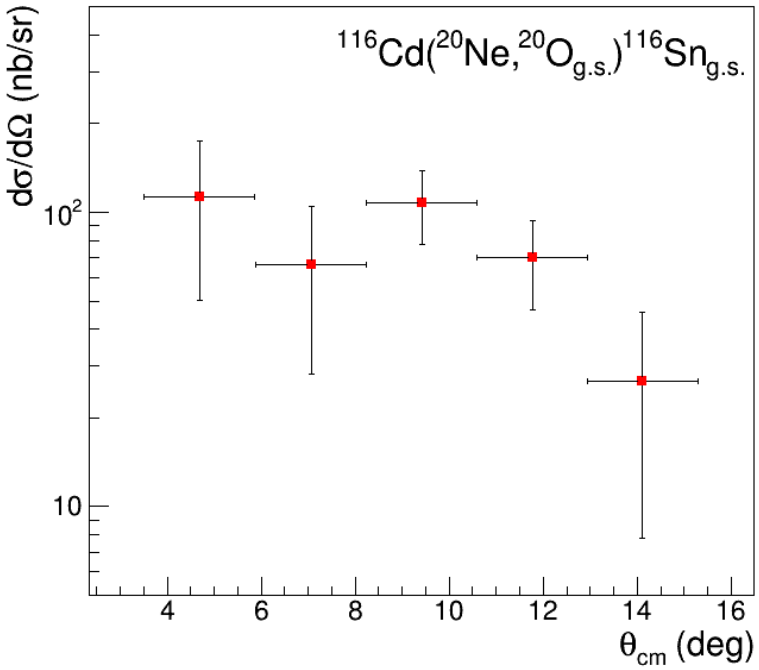

Figure 4.11: Differential cross section angular distribution for the DCE reaction g.s. $\rightarrow$ g.s. transition

Cross section sensitivity analysis of the MAGNEX spectrometer

Due to the small measured DCE cross sections, it is worth to analyze the sensitivity of the experimental set-up to the measurement of such quantity. In the past no studies of this kind were performed so the method described in the following was conceived and applied for the first time. The analysis aims at deducing the cross section sensitivity of the MAGNEX spectrometer - i.e. the lower limit cross section value significantly measurable by the detection system - and it was developed for the ^{116}Cd(^{20}Ne,^{20}O)^{116}Sn DCE reaction data discussed in the Thesis.
Unavoidable contributions limiting the overall spectrometer sensitivity come from the not ideal PID, due to finite detection resolution and background contaminations. To estimate the purity of the described PID method in the measurement of the DCE channel, it was first studied the effect of the identification topological cut defined for $^{20}O^{8+}$ ejectiles in the (E_{resid}; X_{foc}) representation, shown in Fig. 4.3(b). In fact, such contour selects not only the $^{20}O^{8+}$ ions but also part of the $^{20}F^{8+}$ and $^{20}Ne^{8+}$ ejectiles since the three species, having similar $\frac{\sqrt{m}}{q}$, share almost the same position in the (X_{foc}; E_{resid}) correlation plot. Plotting the (ΔE_{DC2}; ΔE_{PC}) histogram gated by the mentioned topological condition, the three expected loci are clearly visible, as shown in Fig. 4.12. The corresponding bi-dimensional histogram, shown in Fig. 4.12, was thus fitted by a three-Gaussian-sum function corresponding to the $^{20}O^{8+}$, $^{20}F^{8+}$ and $^{20}Ne^{8+}$ species. Then, the contribution of $^{20}F^{8+}$ and $^{20}Ne^{8+}$ events underneath the $^{20}O^{8+}$ peak was estimated by integrating the tails of their individual fit in the $^{20}O^{8+}$ region. The latter is defined as ($\pm 3\sigma_x$, $\pm 3\sigma_y$) from its centroid, consistent with the typical PID graphical selection width. The obtained impurity contributions are listed in Tab. 4.2 for some of the central silicon detectors where, due to the kinematic conditions, the three analyzed ions are simultaneously detected. The different silicon pad detectors, in fact, correspond to different horizontal positions along the focal plane and thus to different ejectile kinetic energy. These results represent the relative amount of mis-identified $^{20}O^{8+}$ events from the atomic mass number identification. The error values have been evaluated taking into account the parameters resulting from the fits and including their correlations. The contribution from $^{20}Ne^{8+}$ is considerably smaller than $^{20}F^{8+}$

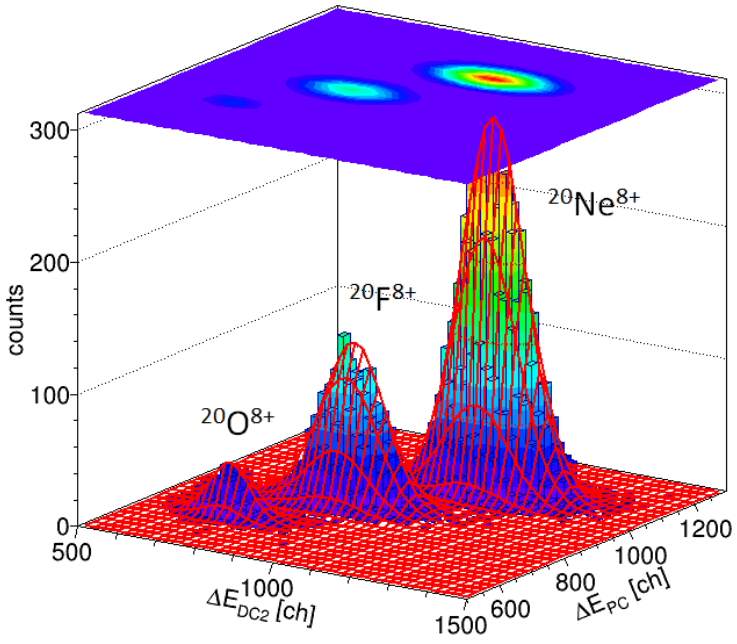

Figure 4.12: Bi-dimensional energy loss histogram for the $^{20}Ne^{8+}$, $^{20}F^{8+}$ and $^{20}O^{8+}$ events in one silicon detectors (Si No. 29) gated with the topological selection for the $^{20}O^{8+}$ ions shown in Fig. 4.3(b). The superimposed overall red function is the fit described in the text.

Table 4.2: Impurities contribution from $^{20}F^{8+}$ (second column) and $^{20}Ne^{8+}$ (third column) ions in the $^{20}O^{8+}$ region of interest for some FPD silicon detectors (Si No.). The values are expressed in percentage with respect to the number of identified $^{20}O^{8+}$ ions. Upper limits are reported if relative error exceeds 100%.

Si No.	$^{20}F^{8+}$ (%)	$^{20}Ne^{8+}$ (%)
20	$<1.2\times10^{-1}$	$<6\times10^{-5}$
23	$<1.7\times10^{-1}$	$<4\times10^{-9}$
26	$1.3\pm0.3\times10^{-1}$	$6\pm3\times10^{-15}$
29	$2.2\pm0.3\times10^{-1}$	$9\pm6\times10^{-16}$

one, so it will be neglected hereafter.
About the mass number and charge state identification purity estimation, an analogous procedure was followed. The contour in the (ΔE_{DC2}; ΔE_{PC}) representation shown in Fig. 4.3(a) was adopted to explore the selected events in the (E_{resid}; X_{foc}) correlation, shown in Fig. 4.13. By comparing the plots in Fig. 4.12 and Fig. 4.13, it clearly emerges that the impurity contribution to the $^{20}O^{8+}$ events from the identification procedure in A and q is much smaller (average peak-to-peak distance of $\sim 20\sigma$) compared to the one coming from the atomic number identification. This is not surprising due to the better intrinsic resolution of both X_{foc} and E_{resid} compared to ΔE_{DC2} and ΔE_{PC} [101, 111].
Fig. 4.13(b), however, highlights another feature: few and isolated events are present between the well-separated peaks, not belonging clearly to any of them. In order to obtain a reliable overall sensitivity estimation of the PID technique, their contribution needs also to be taken into account. The few spurious events visible in Fig. 4.13(b) do not appear to be distributed according to a clear pattern, so it was assumed a constant linear density value. The latter was estimated by considering the three visible peaks shown in Fig. 4.13(b) which corresponds to the $^{19}O^{8+}$, $^{20}O^{8+}$

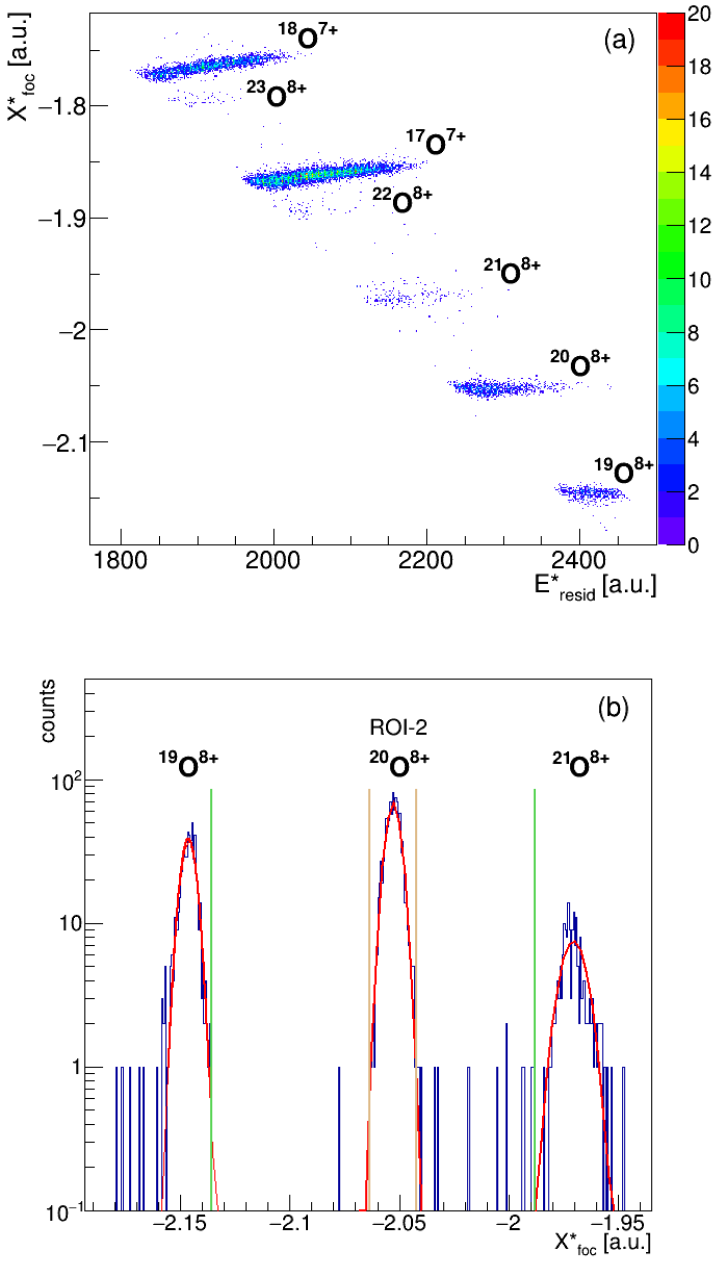

Figure 4.13: Panel (a): (E_{resid}; X_{foc}) correlation plot for the gated oxygen events after an axis rotation. Panel (b): projection on the X^*_{foc} axis. Few spurious events between the three peaks corresponding to the $^{21}O^{8+}$, $^{20}O^{8+}$ and $^{19}O^{8+}$ are visible. The fit functions described in the text is also reported as well the region of interest for the $^{20}O^{8+}$ ions (ROI-2).

and $^{21}O^{8+}$ ions, fitting them with Gaussian functions and assuming as background events all the ones located outside $\pm 3\sigma$ from their centroids. The amount of them falling underneath the $^{20}O^{8+}$ identification region of interest - defined as the interval spanning $\pm 3\sigma$ around the $^{20}O^{8+}$ distribution center of gravity (ROI-2, see Fig. 4.13(b)) - was estimated. The values obtained for the different silicon detectors examined are listed in Tab. 4.3. The error on such quantity has been estimated by Monte Carlo varying the limits of the two defined regions between the $^{19}O^{8+}$, $^{20}O^{8+}$ and $^{21}O^{8+}$ peaks within the parameter errors resulting from their fits, repeating the procedure and assuming the standard deviation of the obtained distribution.
The results about impurity and background contaminations allow to estimate the absolute cross section sensitivity limit.
Regarding the PID impurities, the trend of $^{20}F^{8+}$ contamination events shown in Tab. 4.2, which rises for silicon detectors corresponding to higher excitation energy, is connected to the expected enhancement of the ^{116}Cd(^{20}Ne,^{20}F)^{116}In SCE reaction cross section at increasing excitation energy. To validate this hypothesis, the ratio between the estimated impurity events over the total $^{20}F^{8+}$ identified ones, R($^{20}F^{8+}$) was extracted. The values, listed in Tab. 4.3, confirm that such trend is strictly connected to the growing cross section of the (^{20}Ne,^{20}F) channel. A global average factor given by the weighted average of the R($^{20}F^{8+}$) factors - equal to $0.029\pm0.003\%$ - was extracted. This latter was further combined with the MAGNEX ray-reconstruction efficiency. In fact, ray-reconstruction algorithms act as a filter reducing the $^{20}F^{8+}$ events number kinematically reconstructed as $^{20}O^{8+}$ to 81%. Scaling the SCE channel cross section spectrum by this value, the impurity contribution of $^{20}F^{8+}$ in the DCE spectrum is estimated. The latter, which arises from the $^{20}F^{8+}$ impurity events in the atomic number particle identification, is shown in Fig. 4.14.
About the PID background contribution, it is likely related to not-exact residual energy (E_{resid}) measurement by the silicon detectors, due to different possible phenomena like incomplete charge collection at the border and pile-up effects. So, an overall factor given by the weighted average of the estimated ones in the different detectors was adopted: $\langle BG(^{20}O^{8+})\rangle = 0.29\pm0.02\%$. Moreover, since 10% of such background events are generated, in average, by $^{20}O^{8+}$ ions, $\langle BG(^{20}O^{8+})\rangle$ factor was scaled of 0.9, ob-

Table 4.3: For the selected silicon detectors (Si No.), PID purity factors for $^{20}F^{8+}$ ejectiles R($^{20}F^{8+}$) (second column). The values are expressed in percentage with respect to the total number of identified $^{20}F^{8+}$ ions in each corresponding silicon detector. PID background contribution to $^{20}O^{8+}$ events, BG($^{20}O^{8+}$) (third column). The values are expressed in percentage with respect to the number of identified $^{20}O^{8+}$ ions in corresponding silicon detectors. Upper limits are reported whether the error exceeds the central value.

Si No.	R($^{20}F^{8+}$) (%)	BG($^{20}O^{8+}$) (%)
20	<0.95	<0.19
23	<0.095	0.19 ± 0.10
26	0.021 ± 0.004	0.28 ± 0.02
29	0.043 ± 0.006	0.32 ± 0.03

taining the background percentage affecting the total $^{20}O^{8+}$ events number. Finally, the background cross section spectrum was deduced assuming a uniform distribution in energy, returning a value of 0.19 nb/MeV.
The discussed contributions resulting from the particle identification background and impurity are reported in Fig. 4.14 as a function of the system excitation energy. Their sum, also shown in Fig. 4.14, represents the overall PID cross section sensitivity distribution for the ^{116}Cd(^{20}Ne, ^{20}O)^{116}Sn DCE reaction. At low excitation energy the contribution from the spurious background events is dominant with respect to the Fluorine impurities one. The turning point between the two is $\sim$ 9 MeV, thus, in the ground state region (ROI-GS), defined as $\pm$0.66 MeV in excitation energy, the contribution due to the $^{20}F^{8+}$ contamination is almost negligible. The integrated cross section sensitivity for the ^{116}Cd(^{20}Ne,^{20}O)^{116}Sn DCE reaction in such energy interval amounts to 0.26 nb. This result is characteristic of the present system, depending on both kinematics and dynamics of the contaminant (^{20}Ne,^{20}F) SCE reaction. However, the sensitivity values do not exceed the maximum of 0.5 nb/MeV as shown by Fig. 4.14.
As a consequence of the performed analysis, the estimated signal-to-noise ratio of the DCE channel, which can be deduced by Fig. 4.15, results very favorable. This point confirms the high significance of the extracted experimental cross section values especially for the ground-state to ground-state transition but also for the others reported in Tab. 4.1.
The obtained results depend, of course, on the considered reaction channel. However, the method can be systematically applied to any other system or channel. The DCE reaction channel was analyzed because it represents the most suppressed channel among the investigated ones and the most relevant to the aim of the NUMEN project.

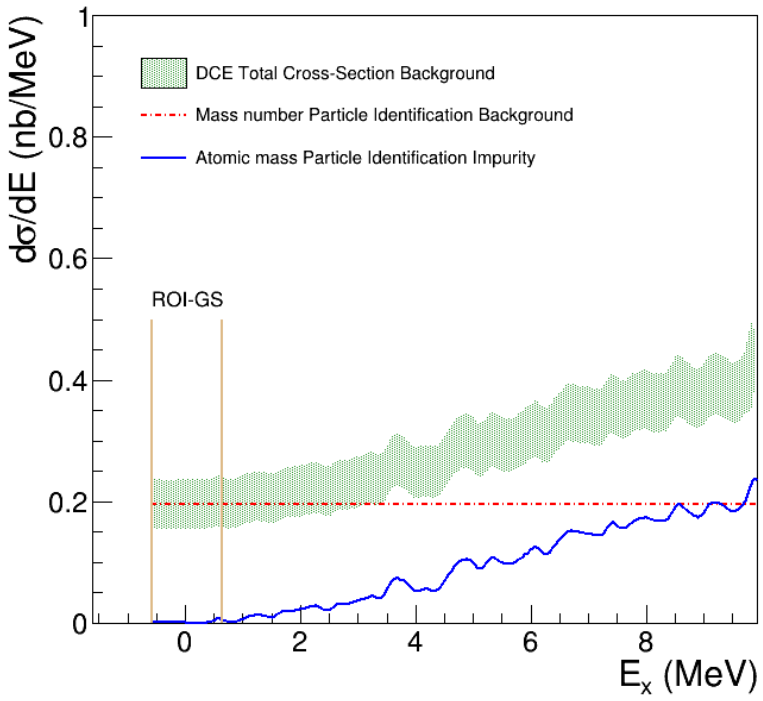

Figure 4.14: Differential cross section sensitivity distribution for the ^{116}Cd(^{20}Ne,^{20}O)^{116}Sn reaction at 15.3 AMeV. The PID background (red dashed line), the $^{20}F^{8+}$ impurities (blue line) contributions discussed in the text and the ground state region (ROI-GS) are also depicted. The 1σ-error band is shown only for the cross section distribution for clarity reasons.

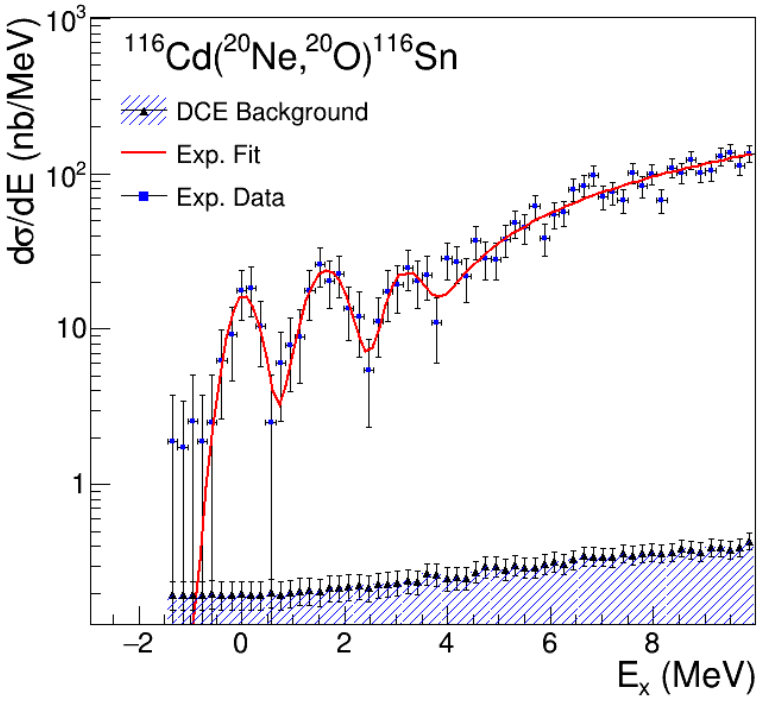

Figure 4.15: Differential cross section distributions of DCE reaction and the estimated sensitivity

4.2.2 ^{116}Cd(^{20}Ne, ^{20}F)^{116}In Single Charge Exchange reaction

The ^{20}F ions are detected in the 8+ charge state so their number should be scaled by the 8+/9+ charge state factor to deduce the main (9+) absolute cross section. This factor, considering the ^{20}F ions crossing a carbonium foil at 15 AMeV kinetic energy, amounts to $\sim 5.7\times10^{-3}$ [90]. Since the explored energy spectrum extends up to quite high excitation value, a charge state scaling factor as a function of the excitation energy was deduced by interpolating the data of Ref. [90]. Moreover, in order to include also the dependence of the energy from the scattering angle given by the kinematic condition, such charge state functions were calculated for each angular bin in 2° step. In the lack of any indication from literature, the choice was for a phenomenological exponential relation. As an illustration, in Fig. 4.16 the function adopted in the $8° < \theta_{lab} < 10°$ angular range is reported. The discrepancies on the deduced charge state factor

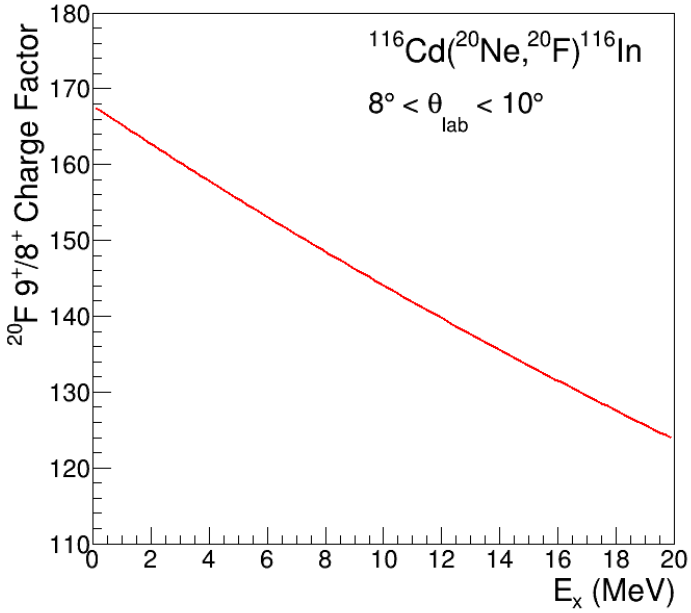

Figure 4.16: 9+/8+ charge state factor function for the ^{20}F obtained interpolating the values reported in Ref. [90] in a fixed angular interval

values were tested adopting different functions. The differences did not exceed 20% in all cases, thus representing a modest possible source of error. The differential cross section spectrum in excitation energy for the Single Charge Exchange reaction is reported in Fig. 4.17. In the small

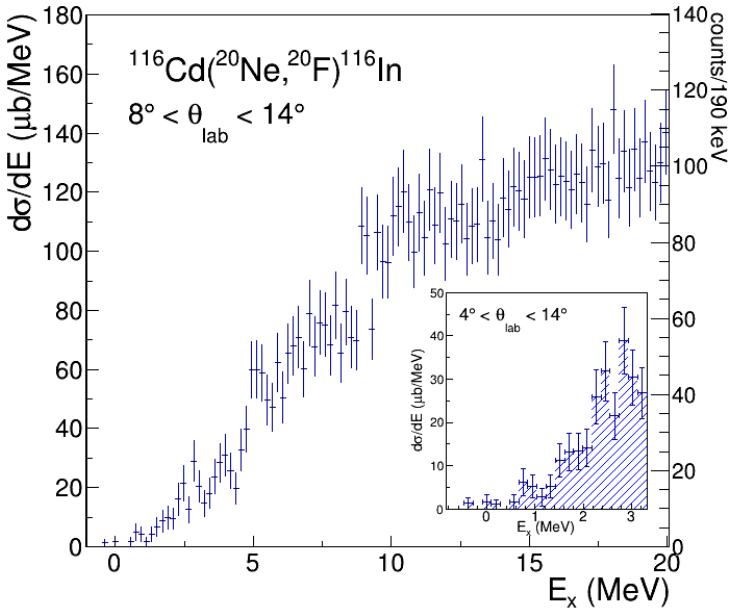

Figure 4.17: SCE differential cross section distribution in energy. In the main panel, it is shown up to high excitation energy for the angular range $8^\circ < \theta_{lab} < 14^\circ$. In the inset, the zoomed low energy view in the full angular range is reported.

panel of Fig. 4.17, the cross section spectrum in the full angular acceptance for the excitation energy range up to 3.5 MeV is reported. The high level density of odd-odd ^{116}In residual nucleus, combined with the experimental energy resolution, does not allow the investigation of single or isolated transitions. Therefore, cross sections can be extracted only by integrating on selected energy range, including the contributions from several nuclear transitions. The list of ^{116}In and ^{20}F nuclear states up to 0.35 MeV and the corresponding experimental integrated cross section value are reported in Tab. 4.4.

Table 4.4: List of ^{116}In and ^{20}F nuclear states distinguished for spin and parity (J^{π}) and excitation energy (E_x) up to 0.35 MeV. In the last column the integrated experimental cross section value in the same excitation energy range is reported.

Nucleus	J^{π}	E_x (MeV)	σ (μb)
^{116}In	1^+	0.000	
^{20}F	2^+	0.000	
^{116}In	5^+	0.127	
^{116}In	4^+	0.223	
^{116}In	2^+	0.273	
^{116}In	8^-	0.290	
^{116}In	4^+, 5^+	0.314	
		0.8$\pm$0.5	

4.2.3 ^{116}Cd(^{20}Ne, ^{19}F)^{117}In One-Proton Transfer reaction

The ^{19}F ions are detected, as the ^{20}F, in the 8+ charge state. Thus, a similar procedure as the one described for the ^{20}F, to scale their number on the corresponding charge state factor, was applied.
The differential cross section distribution in excitation energy of the one-proton stripping channel is shown in Fig. 4.18. In agreement to the Brink's transfer matching conditions [67], the spectrum is peaked at E_x^{opt} $\sim$ 15 MeV. In the inset, the magnification of the low excitation energy part up to 4.5 MeV is shown. Above 1 MeV, three structures at $\sim$ 1.5, $\sim$ 2.4 and $\sim$ 3.5 MeV are visible. However, due to the ^{117}In and ^{19}F high nuclear level densities, they are expected to be the unresolved sum of several different peaks. In order to extract the differential cross section angular distribution in the low energy region, the data need to be analyzed in each different angular bin. Fig. 4.19 shows the performed analysis in the $8^\circ < \theta_{lab} < 9^\circ$ angular interval. The cross section trend at low excitation energy is nicely reproduced by a logarithmic function (in green). In fact, as expected, the g.s. $\rightarrow$ g.s. transition cannot be experimentally resolved

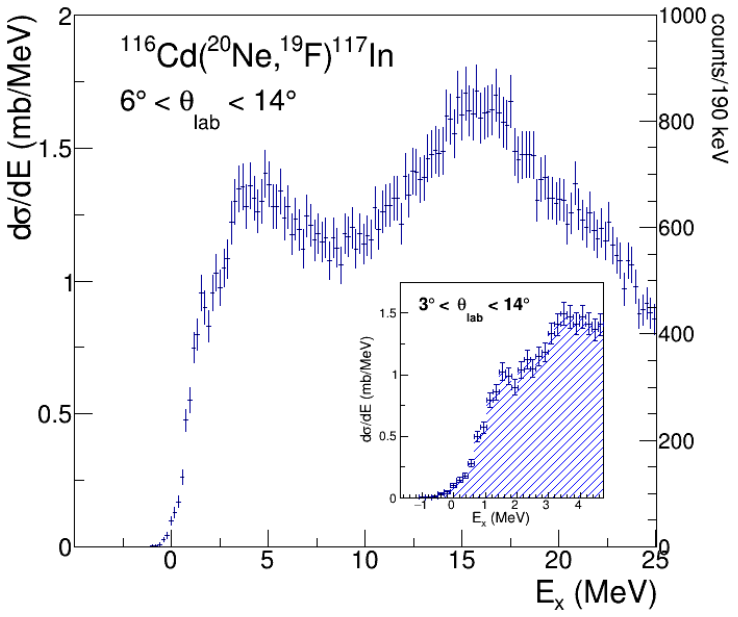

Figure 4.18: One-proton transfer differential cross section distribution in excitation energy. In the main panel the spectrum is shown up to high excitation energy for the angular range $6^\circ < \theta_{lab} < 14^\circ$. In the inset, the zoomed low energy view highlights the presence of three visible structures.

from the first excited states at $\sim$ 0.1, 0.2, 0.3 MeV. The smooth trend up to 1 MeV excitation energy suggests a not-dominant contribution from any of the other low-lying excited states. Beyond 1 MeV, three Gaussian functions (in light-blue, magenta and yellow) were introduced to fit the mentioned visible structures. Due to the high level densities and the finite energy resolution, they may have contributions from several states, thus the fit parameters have been let to vary freely. The described fit procedure was necessary in order to estimate the contributions resulting from the tails of such structures in the energy range up to 1 MeV. The differential cross section angular distribution in the 0-1 MeV excitation energy range is reported in Fig. 4.20. It is interesting to note that the shape results clearly peaked in the grazing angle ($\theta_{gr} \sim 15^\circ$) region.

Table 4.5: List of ^{117}In and ^{19}F nuclear states separated for spin and parity (J^{π}) and excitation energy (E_x (MeV)) up to 1 MeV. In the last column the integrated experimental cross section value corresponding to the same energy range is reported.

Nucleus	J^{π}	E_x (MeV)	σ (mb)
^{117}In	$9/2^+$	0.00	
^{19}F	$1/2^+$	0.00	
^{19}F	$1/2^-$	0.110	
^{19}F	$5/2^+$	0.197	
^{117}In	$1/2^-$	0.315	
^{117}In	$3/2^-$	0.589	
^{117}In	$3/2^+$	0.660	
^{117}In	$7/2^+$	0.748	
^{117}In	$1/2^+$	0.749	
^{117}In	$5/2^+$	0.881	
			0.35$\pm$0.02

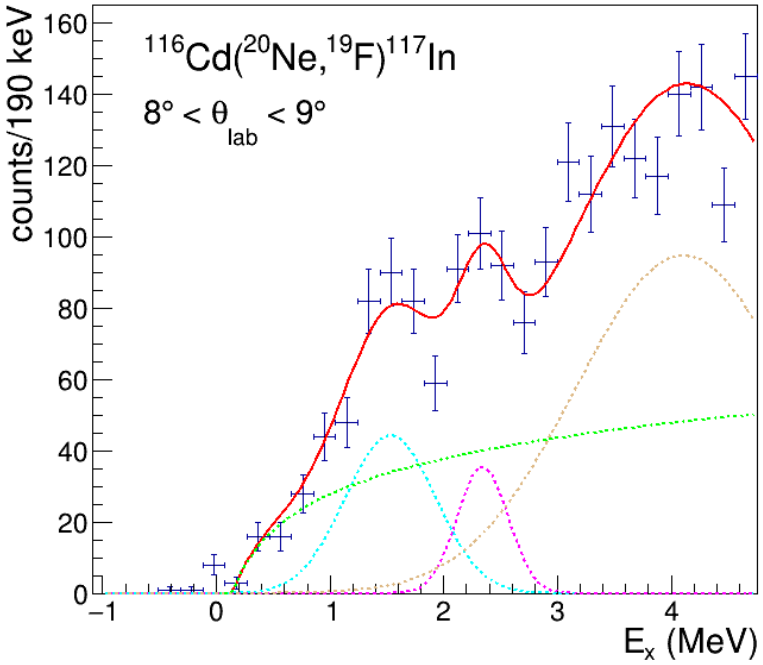

Figure 4.19: Energy spectrum analysis of the 1p-transfer channel in the $8^\circ < \theta_{lab} < 9^\circ$ angular range. The three visible peaks above 1 MeV were phenomenologically reproduced by a multi-Gaussian function fit in order to estimate their contributions in the excitation energy interval up to 1 MeV.

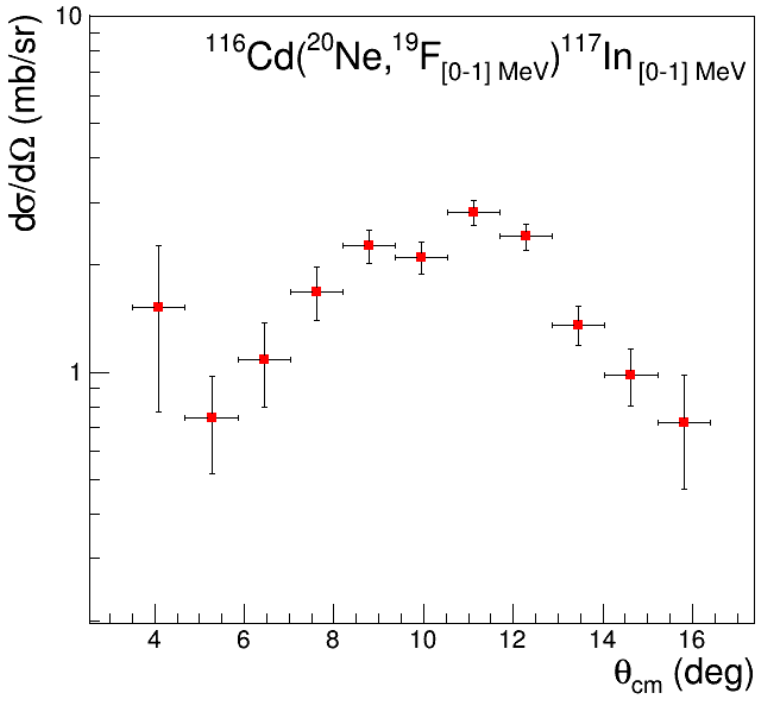

Figure 4.20: 1p-transfer differential cross section angular distribution in the excitation energy range up to 1 MeV.

4.2.4 ^{116}Cd(^{20}Ne, ^{18}O)^{118}Sn Two-Proton Transfer reaction

The differential cross section spectrum in excitation energy for the two-proton stripping reaction is reported in Fig. 4.21. In the main panel it is shown up to $\sim$ 15 MeV whereas the inset shows the low excitation energy range up to $\sim$ 4 MeV. In this latter, few bumps are visible thus motivating a more accurate cross section analysis shown in Fig. 4.22. The g.s.

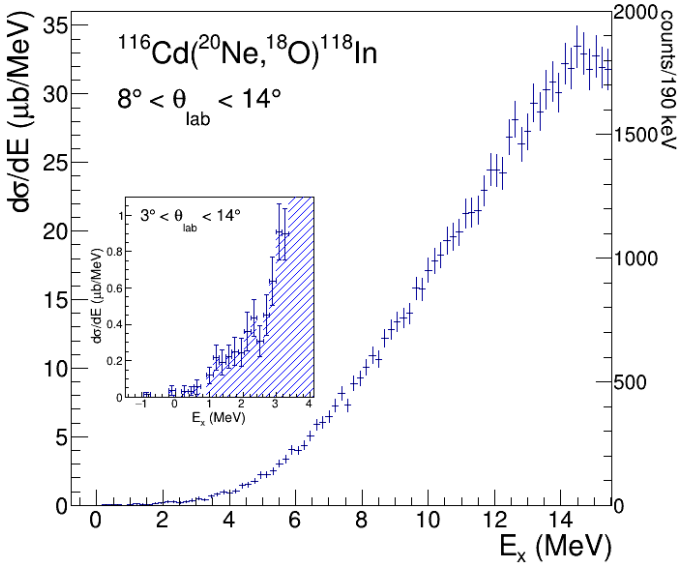

Figure 4.21: 2p-transfer differential cross section spectrum in excitation energy. In the main panel the distribution is shown up to high excitation energy for the angular range $8^\circ < \theta_{lab} < 14^\circ$. In the inset, a zoomed view of the low energy part is shown, highlighting the presence of very suppressed structures.

$\rightarrow$ g.s. transition (in light-blue) is visible even if very suppressed. The bump at $\sim$ 1.2 MeV is well reproduced by a second Gaussian function (in yellow) which is centered at the energy expected for the transition to first 2^+ state of the ^{118}Sn. In order to correctly extract the absolute cross section corresponding to such transitions, the distribution was further fitted by three additional Gaussian corresponding to the visible peaks plus a second order polynomial introduced to reproduce the smooth trend

at higher excitation energy. Due to the finite energy resolution and the

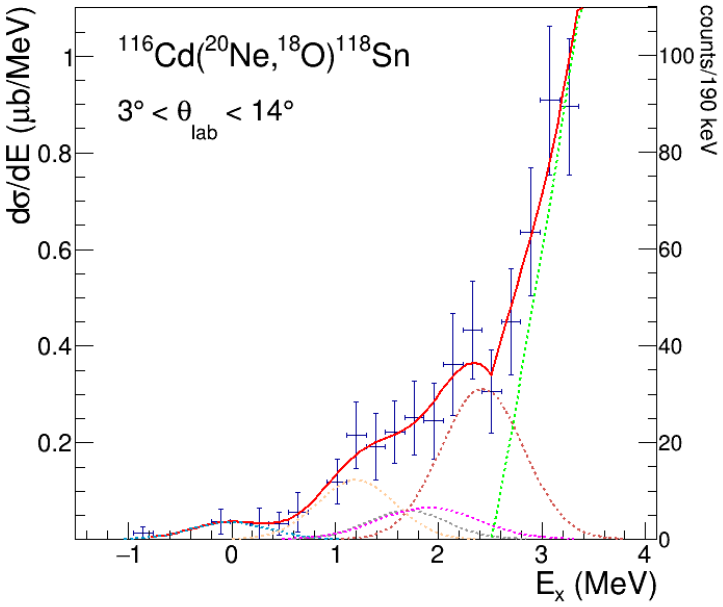

Figure 4.22: Experimental analysis of the differential cross section spectrum for the 2p-transfer distribution in the low excitation energy range. The g.s. transition (in light-blue) as well as the other visible small bumps are modeled by Gaussian functions (in magenta, grey and orange) plus a second order polynomial (in green) introduced to better reproduce the spectrum up to 4 MeV.

level densities of the systems, the visible structures could receive contributions from many possible states, see Tab. 4.6. However, it is interesting to notice that the performed analysis returned for all the Gaussian functions FWHM values compatible with the g.s. one, thus suggesting the dominance of a single state in each energy interval. Furthermore, all the centroids, listed in Tab. 4.6, are close to some specific state energy values, thus strengthening this single state dominance hypothesis. In order to confirm such possibility, however, much higher energy resolution would be needed.

Table 4.6: List of ^{118}Sn and ^{18}O nuclear states separated for spin and parity (J^{π}) and excitation energy (E_x) up to 2.6 MeV. In the fourth column the Gaussian fit centroids discussed in the text are reported. In the last column the corresponding integrated cross section values are given.

Nucleus	J^{π}	E_x (MeV)	Fit centroids (MeV)	σ (nb)
^{118}Sn	0^+	0.00	-0.016	34±20
^{18} O	0^+	0.00	-0.016	
^{118}Sn	2^+	1.229	1.201	120±50
^{118}Sn	0^+	1.758	1.703	60±40
^{18}O	2^+	1.982	1.909	80±65
^{118}Sn	2^+	2.042		
^{118}Sn	0^+	2.056		
^{118}Sn	4^+	2.280		
^{118}Sn	5^-	2.321		
^{118}Sn	3^-	2.324		
^{118}Sn	2^+	2.328		
^{118}Sn	2^+	2.403	2.422	300±190
^{118}Sn	4^+	2.408		
^{118}Sn	4^+	2.489		
^{118}Sn	0^+	2.497		
^{118}Sn	7^-	2.575		
^{118}Sn	2^+	2.577		

4.2.5 Summary

The most significant integrated cross section values deduced by the experimental analyses presented in the previous Sections for Double Charge Exchange (DCE), Single Charge Exchange (SCE), One-Proton Stripping and Two-Proton Stripping reactions are reported in Tab. 4.7.

Table 4.7: List of the integrated cross section values (σ) for the different investigated reaction channels distinguished for nucleus (second column), nuclear state spin and parity (J^{π}) and excitation energy (E_x).

Reaction channel	Nucleus	J^{π}	E_x (MeV)	σ
DCE (^{20}Ne,^{20}O)	^{20}O, ^{116}Sn	0^+	g.s.	12.73$\pm$2.37 nb
DCE (^{20}Ne,^{20}O)	^{20}O	2^+	1.293	3.63$\pm$3.21 nb
DCE (^{20}Ne,^{20}O)	^{116}Sn	2^+	1.673	18.51$\pm$3.40 nb
SCE (^{20}Ne,^{20}F)	^{20}F, ^{116}In	0^+	[0, 0.35]	120$\pm$50 μb
1p-transfer (^{20}Ne,^{19}F)	^{19}F, ^{117}In	0^+	[0, 1]	0.35$\pm$0.02 mb
2p-transfer (^{20}Ne,^{18}O)	^{18}O, ^{118}Sn	0^+	g.s.	34$\pm$20 nb
2p-transfer (^{20}Ne,^{18}O)	^{118}Sn	2^+	1.229	120$\pm$50 nb

Chapter 5

Nucleon Transfer Mechanisms and their contributions to heavy-ion Charge Exchange reactions

Transfer as well as charge exchange reactions are direct processes, i.e. the involved nuclei pass directly from initial to final states without the formation of an intermediate compound system. Such quasi-elastic mechanisms result extremely useful to investigate selected degrees of freedom of the involved nuclei. For example, the nucleus mean field and the single-particle configurations, the existence and behavior of clusters inside the nuclei and other nuclear structure information. Distinctive features which characterize the angular distributions of direct reactions have been experimental observed. In the majority of cases they are peaked at small angles and show regular oscillations. The period and slope of the latter vary smoothly with energy and mass number, the phase is determined by the angular momentum transferred and the amplitude changes regularly with the strength of the Coulomb interaction relative to that of the real part of the nuclear interaction. However, with the increase of the masses of the colliding nuclei i.e. in heavy-ion collisions at energies higher than the Coulomb barrier, it is difficult to single out the direct one-step reactions due to the very strong coupling of the open channels that leads to a strong absorption of the incident flux. Since the aim of the

present investigation, as well as of the NUMEN project itself, is to investigate the direct Charge Exchange reactions, the competition with respect to multi-nucleon transfer mechanisms populating the same final nuclear states needs to be evaluated in the typical NUMEN conditions. In this Chapter, a detailed analysis of the sequential nucleon transfer processes and an estimation of their contributions affecting SCE and DCE channels will be discussed and presented for the ^{20}Ne+^{116}Cd system.

5.1 Optical Potential

One of the main ingredients of the quantum description of direct reactions is the optical potential. The interaction between projectile and target, in terms of relative separation, is assumed to be describable by a one-body complex potential. Indeed, the diffraction pattern shown by most of the nuclear reaction angular distributions led to the introduction of a complex expression, with the real part describing the scattering of the projectile nucleus on the target one. The imaginary part, instead, deals with the loss of probability flux from the elastic channel and the channels of interest.
Phenomenological optical potentials are often parameterized in terms of energy-dependent Woods-Saxon functions for the nuclear part while the imaginary one typically has volume plus surface contributions [116]. However, such parametric potentials, derived from wide systematics in mass and energy, are expected to reproduce only in average the trend for specific systems, often requiring additional case by case arbitrary scaling on the data [82]. Thus, it is preferable to adopt a potential obtained in a microscopic way.
The double-folding approach calculates the heavy-ion interaction potential $V(\boldsymbol{r})$ using realistic nucleon-nucleon (NN) interaction [117]. In particular, the optical potential for heavy-ion scattering is obtained by averaging an appropriate NN interaction over the matter distribution densities of the two colliding ions

$$V(\boldsymbol{r}) = \int\int \rho_1(\boldsymbol{r}_1)\rho_2(\boldsymbol{r}_2)v_{NN}(\boldsymbol{r}-\boldsymbol{r}_1+\boldsymbol{r}_2)d^3r_1 d^3r_2 \tag{5.1}$$

The integration is performed over the projectile and target volumes, v_{NN} is the effective nucleon-nucleon interaction and $\rho_i(\boldsymbol{r}_i)$ are the nuclear density distributions that can be extracted from appropriate experimental dataset or by mean field calculations. One of the most frequently used NN potentials is the M3Y density-dependent[118]. The latter includes central, spin-orbit and tensor terms whereas the proton (p) and neutron (n) density distributions are parametrized by Woods Saxon functions

$$\rho_{p,n}(r) = \frac{\rho_{0_{p,n}}}{1 + e^{\frac{R_{p,n}-r}{a_{p,n}}}} \tag{5.2}$$

where $\rho_{0_{p,n}}$ is the density at the center of the nucleus, $R_{p,n}$ the distribution radius and $a_{p,n}$ the surface thickness.
The double folding São Paulo potential (SPP) [119] also adopts density distributions parametrized as Woods Saxon functions, including Pauli non-locality term.
Theoretical angular distribution of the elastic ^{116}Cd(^{20}Ne, ^{20}Ne)^{116}Cd channel were obtained adopting the described microscopic optical potentials and compared with the elastic scattering data measured in a specific NUMEN run. The comparison between the experimental angular distribution[1] and the optical model (OM) calculations is reported in Fig.5.1, where the elastic over Rutherford differential cross sections are shown. The theoretical distributions are both obtained adopting as real and imaginary normalization coefficients N_R = 1.0 and N_I = 0.78, respectively. The scaling value of the imaginary part has been proven effective in describing the elastic scattering angular distributions for many systems in a wide mass and energy ranges outside the region of strong couplings among different reaction channels [93]. Such normalization coefficient effectively takes into account the coupling of all the other states to the elastic channel, corresponding to the dissipative processes which take flux from the elastic scattering.
The two different potentials return very similar results, providing a good description of the experimental data in the explored angular region ($3^\circ < \theta_{cm} < 20^\circ$). Only at large scattering angles the calculations slightly overestimate the data. A similar effect was observed also for the ^{20}Ne+^{76}Ge

[1]Data reduction performed by Dr. S. Firat.

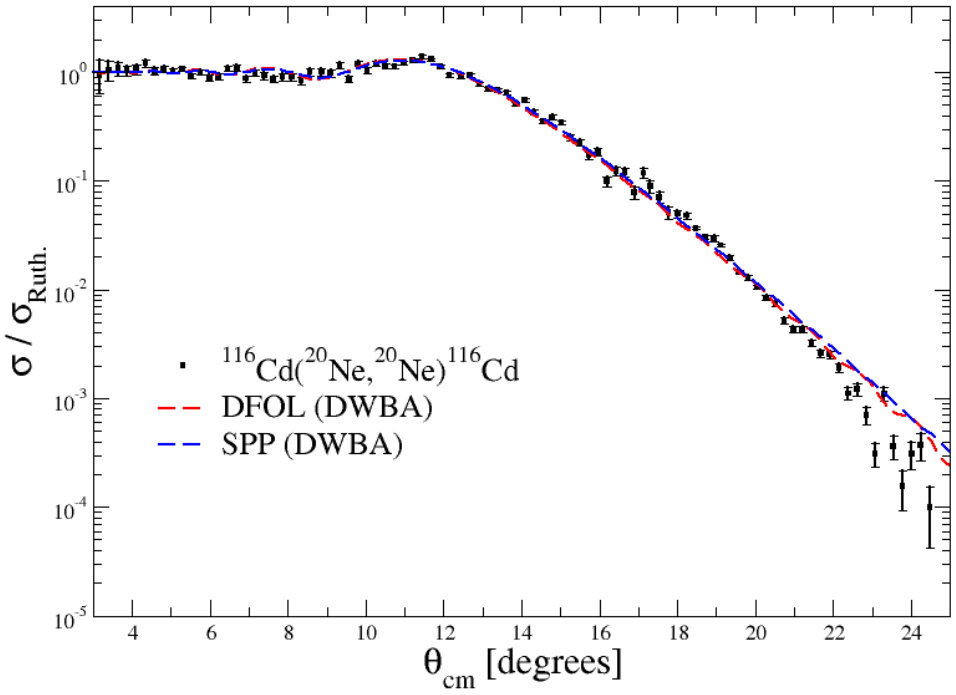

Figure 5.1: Experimental angular distributions of the ^{116}Cd(^{20}Ne, ^{20}Ne)^{116}Cd elastic over Rutherford differential cross section at 306 MeV compared with the optical model calculations adopting M3Y (DFOL) and São Paulo (SPP) potentials.

elastic scattering at the same colliding energy [82]. In the latter case such discrepancy was recovered introducing the couplings to relevant inelastic low-lying states for both target and projectile systems within the Coupled Channel (CC) framework. Such effects, in fact, are not included in the optical model calculations performed in a pure DWBA scheme as the ones here described and they typically involve the region at large angles where the elastic channel cross section is comparable or even weaker than inelastic one, thus resulting more sensitive to such absorptions.

5.2 Nucleon Transfer reactions

During a transfer reaction a nucleus A is fragmented into the clusters a + v, the cluster a survives in the final state while the cluster v gets attached to the nucleus b to form the composite system B:

$$(a+v)+b \rightarrow a+(b+v)$$

The relevant couplings are attributed to the nuclear mean fields where the individual nucleons are stripped to or picked up from. Such point of view effectively uncouples the excitation of projectile and target modes and allows the introduction of wave function product. In this approach the quantum mechanical state of the nucleus A can be expressed as:

$$\phi_A = C^A_{av}\phi_a\phi_v\varphi_{av}(\boldsymbol{r}) + \phi^C_A \tag{5.3}$$

where ϕ_a (ϕ_v) represents the internal wave functions of cluster a (v) and $C^A_{av}\varphi_{av}(\boldsymbol{r})$ represents the overlap function, written in terms of a normalized relative wave function $\varphi_{av}(\boldsymbol{r})$ and a spectroscopic amplitude (S.A.) C^A_{av}. The product of these three terms is implicitly coupled to the angular momentum of the nucleus A. ϕ^C_A indicates the part of the state which can not be described as the two moving clusters since different configurations might contribute. Similarly, the state of the nucleus B can be written as:

$$\phi_B = C^B_{bv}\phi_b\phi_v\varphi_{bv}(\boldsymbol{r}') + \phi^C_B \tag{5.4}$$

The transition matrix element that describes the transfer process will be a complex many-body object, that can be expressed as:

$$T(aB,Ab) = \langle \phi_B\phi_a\chi_{aB}|\widehat{O}|\phi_A\phi_b\chi_{Ab}\rangle \tag{5.5}$$

Where χ_{Ab} describes the relative motion of A and b (similarly for χ_{aB}) and $\widehat{O}$ is the adequate many-body operator, typically termed T-matrix, which typically includes the isoscalar (τ=0) and isovector (τ=1) components. The following approximations allow to reduce the full many-body problem of eq. (5.5) to a solvable three-body problem:

- The terms ϕ^C_A and ϕ^C_B, corresponding to complex configurations of A and B, do not contribute significantly to the transfer.

- The normalized overlap functions $\varphi_{av}(\boldsymbol{r})$ and $\varphi_{bv}(\boldsymbol{r}')$ can be approximated by the eigenstates of two-body Hamiltonians with some real mean-field interactions V_{av} and V_{bv}.

- During the collision process the interactions between the clusters a, b and v are completely described by two-body operators V_{bv}, V_{av} and U_{ab}, that cannot alter the internal states of the clusters. The processes that induce the excitations of the clusters b and a are not considered, thus the interaction between them is represented by an effective complex optical potential U_{ab}.

Within such approximations, the transfer matrix elements can be described as

$$T(aB, Ab) = C_{bv}^{B*} C_{av}^{A} T^{(3)}(aB, Ab) \tag{5.6}$$

where the three-body matrix elements can be expressed by

$$T^{(3)}(aB, Ab) = \langle \chi_{aB}^{-}(\boldsymbol{R}')\varphi_{bv}(\boldsymbol{r}')|V_{av} + U_{ab} - U_{aB}|\Psi^{+}(\boldsymbol{R}, r)\rangle \tag{5.7}$$

$\Psi^{+}(\boldsymbol{R}, r)$ represents the exact solution of the three body problem of a, b and v with the corresponding interactions and U_{aB} is a suitable potential that is used to construct the two-body relative wave function $\chi_{Ab}^{-}(\boldsymbol{R}')$. Equivalently, one can use the prior form:

$$T^{(3)}(aB, Ab) = \langle \Psi^{-}(\boldsymbol{R}', r')\varphi_{bv}(\boldsymbol{r}')|U_{ab} + V_{bv} - U_{Ab}|\chi_{Ab}^{+}(\boldsymbol{R})\varphi_{av}(\boldsymbol{r})\rangle \tag{5.8}$$

where the three-body and two-body wave functions have similar meanings. It should be noticed that the previous expressions are exact, assuming a three body model for the transfer process.
The most widely used method for describing direct nuclear processes, and in particular transfer reactions, is the Distorted-Wave Born Approximation (DWBA). It can be applied whenever the interaction potential can be expressed as the sum of two terms $V = V_I + V_{II}$ such that the Schrödinger equation for a particle subject to V_I is exactly - or at least within a good approximation - solvable and the effects of the remaining term V_{II} are small compared to V_I, so that its wave function can be calculated within the first order Born approximation. Often, in nuclear reaction theory, the distorted waves account for elastic scattering, while

the effect of the investigated inelastic nuclear interaction is described by the potential V_{II}. Hence, the validity of the DWBA depends upon elastic scattering being the most relevant event which occurs when the two nuclei collide, so that other mechanisms can be treated as perturbations. In transfer processes, DWBA is obtained assuming that the three-body wave function can be approximated by

$$\Psi^{+}(\boldsymbol{R}, r) \simeq \chi^{+}_{Ab}\varphi_{av}(\boldsymbol{r}) \tag{5.9}$$

so that, in post representation, the transition matrix element becomes

$$\begin{aligned} T^{(3)}(aB, Ab) &\simeq T^{DWBA}_{post}(aB, Ab) \\ &= \langle \chi^{-}_{Ab}(\boldsymbol{R}')\varphi_{bv}(\boldsymbol{r}')|V_{post}|\chi^{+}_{Ab}\varphi_{av}(\boldsymbol{r})\rangle \end{aligned} \tag{5.10}$$

where

$$V_{post} \equiv V_{av} + U_{ab} - U_{aB}. \tag{5.11}$$

An equivalent derivation can be followed starting from the prior expression for the transfer approximation

$$\Psi^{-}(\boldsymbol{R}', r') \simeq \chi^{-}_{aB}(\boldsymbol{R}')\varphi_{bv}(\boldsymbol{r}') \tag{5.12}$$

thus in the so called prior representation the transition matrix elements become

$$\begin{aligned} T^{(3)}(aB, Ab) &\simeq T^{DWBA}_{prior}(aB, Ab) \\ &= \langle \chi^{-}_{Ab}(\boldsymbol{R}')\varphi_{bv}(\boldsymbol{r}')|V_{prior}|\chi^{+}_{Ab}\varphi_{av}(\boldsymbol{r})\rangle \end{aligned} \tag{5.13}$$

where

$$V_{prior} \equiv V_{bv} + U_{ab} - U_{Ab}. \tag{5.14}$$

The DWBA can also be derived within the Coupled Reaction Channels (CRC) formalism. Such model proceeds by constructing a model of the system wave function and solving the Schrödinger's equation $[H - E]\psi = 0$ as accurately as possible within that model space. In fact, considering the model Schrödinger's equation and projecting separately onto the different internal basis states $\{\varphi_i\}$ the following set of equations is obtained

$$[E_i - H_i]\psi_i(R_i) = \sum_{j \neq i}\langle \varphi_i|H - E|\varphi_j\rangle\psi_j(R_j) \tag{5.15}$$

The matrix element $\langle\varphi_i|H-E|\varphi_j\rangle$ has two different forms, depending on whether one expands on initial $\{\varphi_i\}$ or final $\{\varphi_j\}$ partition basis states, also generating the so called non-orthogonality terms $\langle\varphi_i|\varphi_j\rangle$ when different mass partitions are considered. Expanding the total wave function of the system in the set of internal states $\{\varphi_n\}$, the infinite set of coupled equations for the channel functions (5.15) can be written as

$$[E-\epsilon_n-K-V_{n,n}]\chi_n=\sum_{n'}V_{n,n'}\chi_{n'} \tag{5.16}$$

being K the kinetic energy of their relative motion and $V_{n,n'}$ the coupling potentials derived by the interaction ones. Eq. (5.16) represents a set of coupled differential equations for the set of functions $\{\chi_n\}$ reflecting the Coupled Channel Reaction (CRC) method. The latter is typically solved in iterative way, finally returning the full CRC solution.
However, as soon as supplemental states are included in the model function, the number of coupled equations increases as well. Among the possible approximated solutions, the Distorted Wave Born Approximation (DWBA) is obtained fixing at zero the coupling term of the first equation which then becomes

$$[E-\epsilon_n-K-V_{0,0}]\chi_0=0 \tag{5.17}$$

The corresponding solution χ_0 is then deduced and inserted into the other equations corresponding to the state n, thus providing a first order approximation for χ_n. Such approximation neglects any back coupling between the different considered channels, resulting thus appropriate only when such effects are small.
The Coupled Channel Born Approximation (CCBA), instead, includes in the DWBA scheme the couplings to the target and projectile excited states in the initial partition. In fact, next to elastic scattering, inelastic scattering to some collective states often has the largest cross sections. Hence, it is a natural extension to include these channels in the description of the reaction. The transitions between the different partitions, instead, are calculated in the pure DWBA framework. In such a way the calculations take into account the inelastic excitations of the involved nuclei, which could represent relevant reaction routes especially in considering heavy-ion-induced collisions.

5.2.1 ^{116}Cd(^{20}Ne, ^{19}F)^{117}In One-Proton Transfer reaction analysis

The experimental one-proton stripping differential cross section shown in Fig. 4.20 was analyzed in the CCBA and CRC frameworks. A preliminary DWBA analysis was also performed, setting all the S.A. to one in order to investigate the existence of dominant transitions among all the different possible ones. Such a study could be important due to the complex nuclear structure of the systems involved, especially the heavy odd-odd ^{117}In residual nucleus and its corresponding high level density. In such conditions, in fact, since it could be hard to include all the possible transitions, it would be useful considering, at least, those which are kinematically favored. In the present case, ten nuclear states (see Tab. 4.5) are already included in the low excitation energy region up to 1 MeV, where the experimental angular distribution of Fig. 4.20 was extracted. Thus, even considering for the initial partition ^{20}Ne + ^{116}Cd just the ground states, twenty nuclear transitions have to be computed. Their different contributions are shown in Fig. 5.2 together with the incoherent sum. It is interesting to note that they result all comparable and that all the transitions show a similar overall trend peaked at the grazing angle region ($\theta^{gr}_{c.m.} \approx 15^{\circ}$) independently of the orbital momentum transferred. The latter is a distinctive feature of the reactions in presence of strong absorption.

Inelastic scattering to collective states, however, often presents large cross sections in heavy-ion collisions, as already anticipated. Hence, they have to be included in an accurate description of the reaction, to account for the inelastic scattering plus transfer two-step process. In the present calculation, the ^{20}Ne$_{1.634}$ (2^+) and ^{116}Cd$_{0.513}$ (2^+) states were included in the initial partition. Thus, in addition to DWBA, the calculation was also performed in CCBA and CRC schemes to evaluate the effects of the coupling to the initial partition excited states (CCBA) as well as the back couplings (CRC). The adopted coupling scheme for the projectile and target systems in the CRC calculation is shown in Fig. 5.3. The nuclear structure of the involved nuclei was described microscopically by shell-model (SM), adopting the NushellX code [120]. For the projectile-ejectile system the spectroscopic amplitudes were derived using the Zuker-Buck-McGrory

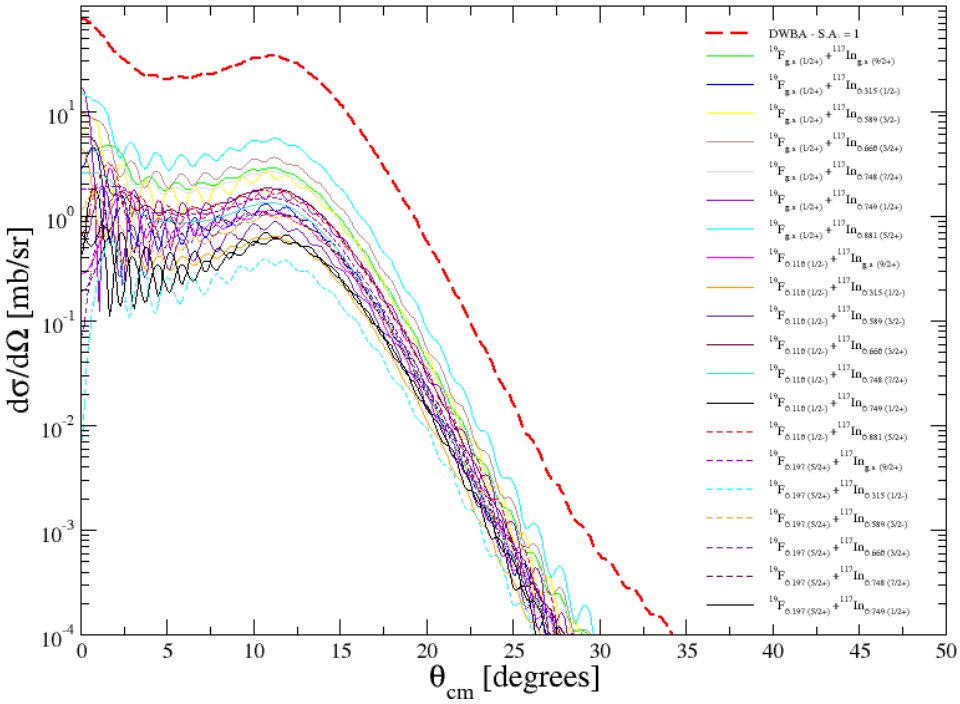

Figure 5.2: DWBA calculation for the ^{116}Cd(^{20}Ne, ^{19}F)^{117}In one-proton stripping angular distribution in the 0-1 MeV excitation energy range. All the considered transitions are reported as well their incoherent sum (dashed red line).

(ZBM) interaction [121]. It considers the {$1p_{1/2}$,$1d_{5/2}$, $2s_{1/2}$} as valence orbits for the neutrons and protons and the ^{12}C nucleus as closed core. In Tab. 5.1 some of the ^{19}F energy nuclear states values predicted by the adopted model are listed.

For the target-residual system, the protons valence model used includes the {$2p_{1/2}$, $1g_{9/2}$, $1g_{7/2}$, $2d_{5/2}$} orbits and the neutron sub-space considers the {$1g_{7/2}$, $2d_{5/2}$, $2d_{3/2}$, $3s_{1/2}$, $1h_{11/2}$} orbits for the valence neutrons [122]. The ^{88}Sr nucleus is considered as a core and because of this, such interaction is referred to as 88Sr45.

The comparison between the experimental angular distribution presented in Sec. 4.2.3 and the DWBA, CCBA and CRC calculations is shown in Fig.

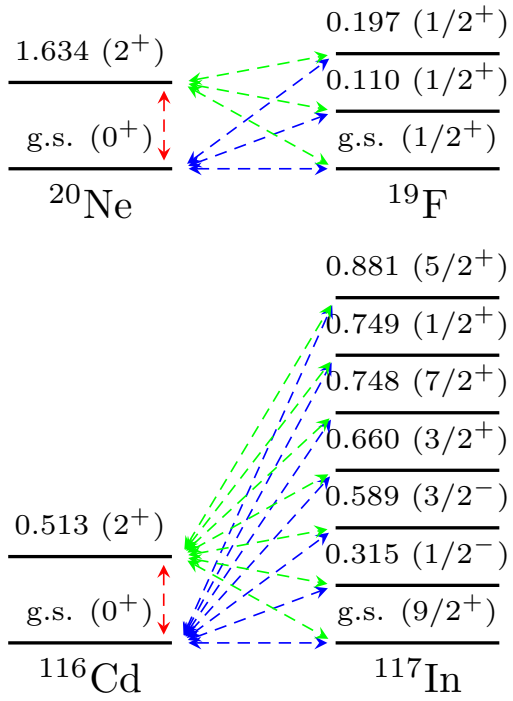

Figure 5.3: Coupling scheme adopted in the ^{116}Cd(^{20}Ne, ^{19}F)^{117}In one-proton stripping CRC calculation

5.4. No scaling factors are introduced in the calculations, thus the agreement results very satisfying, especially considering the high number of channels involved in the calculations and the complicated internal structures of the considered nuclei. In particular, the shape of the experimental angular distribution peaked in the grazing angle region is well described by all the calculations. One should notice that, the inclusion of the coupling with first excited states (CCBA) decreases the cross section at small angles but increasing, instead, at larger ones compared with the DWBA calculation. The back couplings among the different channels, included in the full CRC calculation, globally enhances the cross section value, improving the matching with the experimental data.

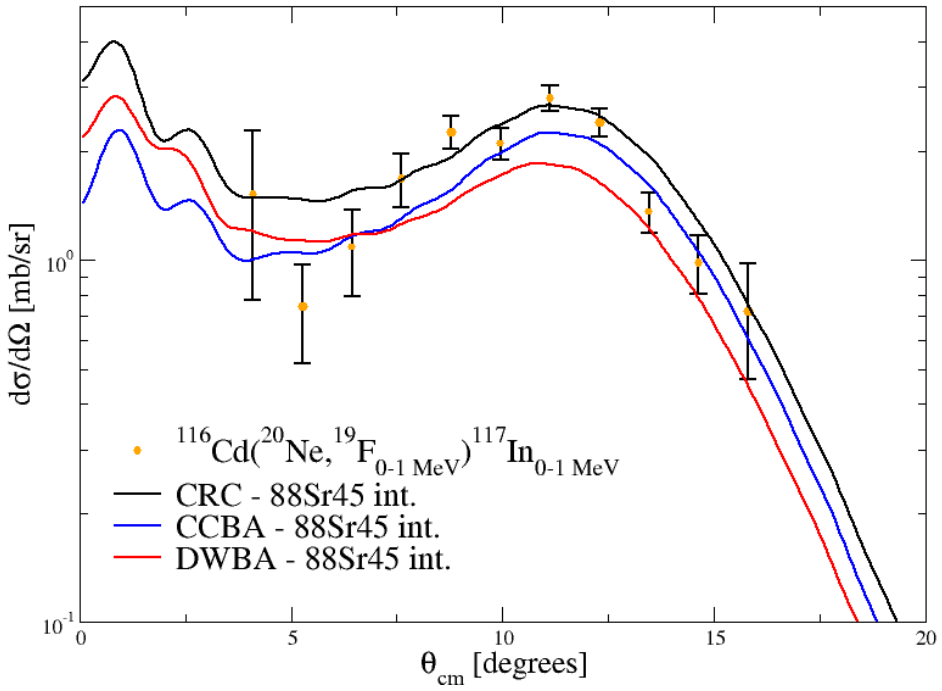

Figure 5.4: Comparison between DWBA, CCBA and CRC calculations and the experimental angular one-proton stripping cross section distribution in the 0-1 MeV excitation energy range

5.2.2 Sequential One-Nucleon Transfer processes and Competition with Single Charge Exchange reaction

The second-order nucleon transfer processes proceeding via sequential proton-stripping and neutron-pickup could populate the same final states involved in SCE reaction, see the sketch in Fig. 5.5.
The competition among the two different mechanisms has already been investigated in the past - see for a review on the topic Ref. [57] - but mainly considering light and medium systems [123], highlighting a pronounced selectivities to incident energies and scattering angles [124, 125, 126] and to the different final states involved [127].
To the aim of NUMEN, however, such analysis have to be extended to

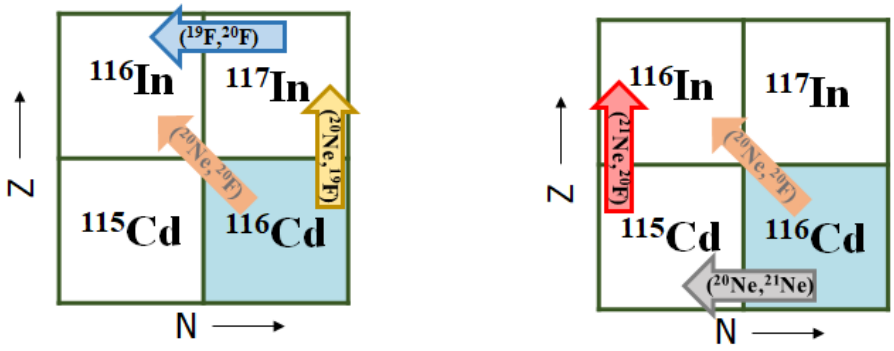

Figure 5.5: Schematic representation of sequential one-nucleon transfer mechanisms in competition with the (^{20}Ne, ^{20}F) SCE channel. The 1p-stripping + 1n-pickup and the 1n-pickup + 1p-stripping routes are depicted on the left and right, respectively.

heavy nuclei as the $0\nu\beta\beta$ candidates typically are and in the energy and angular ranges explored by the project [128].
The two-step transfer contributions are typically calculated in the second-order DWBA. The corresponding transfer matrix elements are given by

$$T^{II}(aB, Ab) = \sum_{\gamma} C_{\alpha\gamma\beta} \langle \chi_\beta | F_{\beta\gamma} G F_{\gamma\alpha} | \chi_\alpha \rangle \tag{5.18}$$

where the sum is extended to the intermediate channels γ, $C_{\alpha\gamma\beta}$ contain the spectroscopic factors of the first and second steps, F denotes the transition form factors and G is the optical model Green operator.
In the performed calculations[2], the nuclear structure of the involved nuclei was derived by the microscopical shell model NushellX code [120]. The ZBM interaction, adopted for the projectile-ejectile ^{20}Ne, ^{19}F, ^{21}Ne, ^{20}F systems reasonably reproduces the low-lying states of the intermediate nuclei (see Tab. 5.1). The model space used to describe the nuclear structure of the heavy nuclei considers the {$1f_{5/2}$, $2p_{3/2}$, $2p_{1/2}$, $1g_{9/2}$} orbits for the valence protons, and the {$1g_{7/2}$, $2d_{5/2}$, $2d_{3/2}$, $3s_{1/2}$, $1h_{11/2}$} ones for the valence neutrons. The effective interaction derived in this model space - named jj45pna interaction - was elaborated using the ^{78}Ni

[2]In collaboration with Dr. S. Burrello.

Table 5.1: Comparison between theoretical and experimental energy values of the low-lying spectra obtained by SM with ZBM interaction for the ^{19}F and ^{21}Ne projectile-like intermediate nuclei

^{19}F	Exp. (MeV)	Th. (MeV)	^{21}Ne	Exp. (MeV)	Th. (MeV)
$1/2^+$	0.000	0.000	$3/2^+$	0.000	0.000
$1/2^-$	0.110	0.503	$5/2^+$	0.351	0.501
$5/2^+$	0.197	0.409	$7/2^+$	1.750	1.607
$5/2^-$	1.346	1.855	$1/2^-$	2.789	2.686
$3/2^-$	1.459	2.235	$1/2^+$	2.794	3.940
$3/2^+$	1.554	2.485	$9/2^+$	2.867	3.366

nucleus as a core [129]. The proton-proton, neutron-neutron, and proton-neutron interactions are derived from the charge-dependent Bonn potential (CD-Bonn) [130].
The channels of the two different intermediate partitions ^{21}Ne+^{115}Cd and ^{19}F+^{117}In populated, respectively, via 1n-pickup + 1p-stripping (Path1) and 1p-stripping + 1n-pickup (Path2) which have been considered in the two-step DWBA calculations are listed in Tab. 5.2.
The cross section values obtained from the transfer contribution due to the routes mentioned above are listed in Tab. 5.3. The total integrated cross section, given by the sum of the different contributions, is evaluated in 0.07 μb. In order to estimate the role of the sequential-nucleon transfer mechanisms with respect to the SCE process, such value can be compared with the experimental one measured for the SCE reaction (see Tab. 4.4) in the same angular and energy ranges, which amounts to 0.8 ± 0.5 μb. The result of the two-step DWBA analysis thus highlights that the sequential transfer contribution is not the dominant mechanism feeding heavy-ion SCE reaction since it accounts for $\sim$ 10% of its cross section. Such result, combined with the new theoretical description available for the heavy SCE reactions [49], confirms that under the NUMEN experimental conditions - incident energy of few tens of AMeV and very forward angles - they are suitable probes to perform β-like investigations, since their cross

Table 5.2: List of the projectile- and target-like states considered in the two-step DWBA for the two different intermediate partitions populated via 1n-pickup + 1p-stripping (Path1) and 1p-stripping + 1n-pickup (Path2) sequential transfer reactions.

Path1:	J^π (^{21}Ne)	E^* (^{21}Ne) (MeV)	J^π (^{115}Cd)	E^* (^{115}Cd) (MeV)
	$5/2^+$	0.351	$1/2^+$	0.000
	$5/2^+$	0.351	$3/2^+$	0.229
	$5/2^+$	0.351	$5/2^+$	0.361
	$1/2^-$	2.789	$1/2^+$	0.000
	$1/2^-$	2.789	$3/2^+$	0.229
	$1/2^-$	2.789	$5/2^+$	0.361
	$1/2^+$	2.794	$1/2^+$	0.000
	$1/2^+$	2.794	$3/2^+$	0.229
	$1/2^+$	2.794	$5/2^+$	0.361
Path2:	J^π (^{19}F)	E^* (^{19}F) (MeV)	J^π (^{117}In)	E^* (^{117}In) (MeV)
	$1/2^+$	0.000	$9/2^+$	0.000
	$1/2^+$	0.000	$1/2^-$	0.315
	$1/2^+$	0.000	$3/2^-$	0.589
	$1/2^-$	0.110	$9/2^+$	0.000
	$1/2^-$	0.110	$1/2^-$	0.315
	$1/2^-$	0.110	$3/2^-$	0.589
	$5/2^+$	0.197	$9/2^+$	0.000
	$5/2^+$	0.197	$1/2^-$	0.315
	$5/2^+$	0.197	$3/2^-$	0.589

Table 5.3: Integrated ($3^\circ < \theta_{lab} < 14^\circ$) cross section values calculated for the different transitions to the final partitions proceeding via 1n-pickup + 1p-stripping (Path1) and 1p-stripping + 1n-pickup (Path2). The total integrated cross sections are given in the last column.

J^π (^{20}F)	E*(^{20}F) (MeV)	J^π (^{117}In)	E* (^{117}In) (MeV)	σ_{Path1} [μb]	σ_{Path2} [μb]	$\sigma^{SCE}_{transfer}$ [μb]
2^+	0.000	1^+	0.000	0.000	0.113×10^{-2}	0.113×10^{-2}
2^+	0.000	5^+	0.128	1.093×10^{-2}	0.224×10^{-2}	1.317×10^{-2}
2^+	0.000	4^+	0.223	3.605×10^{-2}	0.121×10^{-2}	3.726×10^{-2}
2^+	0.000	2^+	0.273	0.004×10^{-2}	0.675×10^{-2}	0.679×10^{-2}
2^+	0.000	4^+	0.313	1.289×10^{-2}	0.008×10^{-2}	1.297×10^{-2}

sections are only marginally affected by the multi-nucleon transfer contribution. The discussed calculations can be further refined taking into account the inelastic excitations of the involved nuclei in the initial partition in a CCBA scheme. Moreover, also the coherent interference between the two paths should be evaluated since their two contributions were incoherently added.

5.2.3 ^{116}Cd(^{20}Ne, ^{18}O)^{118}Sn Two-Proton Transfer reaction analysis

The theoretical description of two-neutron transfer reactions has been developed much further than for other multi-nucleon transfers, mainly because of its usefulness in probing pairing correlations in nuclei. In the present work the goal is, however, to obtain microscopic results for the two-proton stripping mechanism [131] which is instead a poorly investigated reaction channel. To this aim, the independent coordinate (IC) scheme was adopted, thus taking into account the direct transfer of the two nucleons from the initial partition to the final one. Such approach, however, neglects the explicit calculation of multi-step effects that proceed

from the entrance partition via the intermediate one up to the final channel, resulting accurate only when the intermediate channels are weakly excited or whether they does not couple strongly to the final populated ones. Since the successive mechanisms could be relevant in heavy-ion collisions, also sequential processes were considered. The IC method was adopted to perform CRC calculation in the direct transfer, including the first excited state of $^{20}Ne_{1.63}$ (2^+) and the one-phonon quadrupole state of $^{116}Cd_{0.514}$ (2^+) as well as the two-phonon quadrupole states $^{116}Cd_{1.213}$ (2^+), $^{116}Cd_{1.219}$ (4^+) and $^{116}Cd_{1.283}$ (0^+) for the initial partition. In the final partition, the first 2^+ state for the ^{18}O at 1.982 MeV and the 1.230 MeV (2^+), 1.758 MeV (0^+), 2.043 MeV (2^+), 2.057 MeV (0^+), 2.280 MeV (4^+) ^{118}Sn states were included, see Fig. 5.6 for the corresponding coupling scheme.

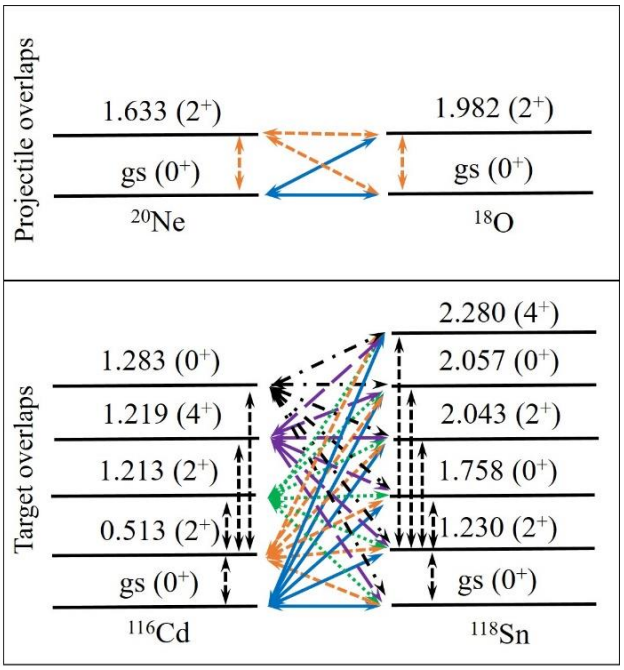

Figure 5.6: Coupling schemes for the projectile and target overlaps considered in the two-proton simultaneous CRC transfer calculation

The sequential transfer calculation was performed via two-step CCBA, including in the initial and final partitions the same target-residual and

projectile-ejectile couplings considered for the IC scheme. Due to the ^{117}In high level density, the number of possible states in the energy range up to the one-proton separation energy (S_{1p} = 7.52 MeV) is too high and it is impracticable to include all of them in the calculation. Therefore, only the levels up to 2.4 MeV were included. The same energy interval was considered for the ^{19}F excited states. The corresponding coupling scheme is shown in Fig. 5.7.

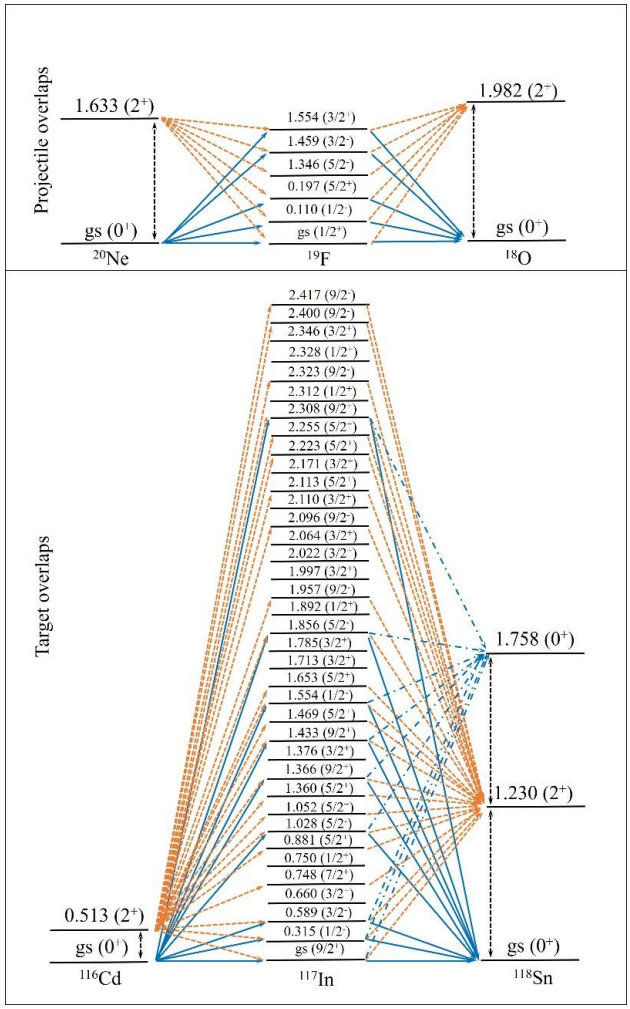

Figure 5.7: Partial coupling schemes for the projectile and target overlaps considered in the two-proton sequential CCBA transfer calculation

Table 5.4: Comparison between experimental (second column) and theoretical (third and fourth columns) cross sections of the ground state and first excited transitions for the ^{116}Cd(^{20}Ne, ^{18}O)^{118}Sn 2p-stripping reaction.

Final channel	Experimental cross section (nb)	ZBM + 88Sr45 int. cross section (nb)	
		Direct	Sequential
$^{18}O_{g.s.}$ (0+) + $^{118}Sn_{g.s.}$ (0+)	34±20	41.1	53.8
$^{18}O_{g.s.}$ (0+) + $^{118}Sn_{1.229}$ (2+)	120±50	53.5	167.2

Both simultaneous and sequential transfer calculations were carried out considering the SPP potential. In particular, the strength coefficient N_I = 0.5 was considered for the imaginary part of the entrance and final partitions since the couplings with relevant excited states were explicitly taken into account. The spectroscopic amplitudes for both projectile-ejectile and target-residual systems were obtained within the microscopic SM running the NushellX code, adopting the ZBM and 88Sr45 interactions, respectively.
The predicted two-proton cross sections for the $^{18}O_{g.s.}$ (0^+) + $^{118}Sn_{g.s.}$ (0^+) and $^{18}O_{g.s.}$ (0^+) + $^{118}Sn_{1.229}$ (2^+) transitions, integrated in the angular range $3^\circ < \theta_{lab} < 14^\circ$, are given in Tab. 5.4. By comparing the theoretical results with the corresponding experimental cross section values - also reported in Tab. 5.4 - one can conclude that a quite satisfactory description of the two-proton stripping reaction is achieved.

5.2.4 Multi-Nucleon Transfer processes and Competition with Double Charge Exchange reaction

From the the cross sections comparison of the two-proton transfer channel with the DCE and the one-proton transfer ones (see Tab. 4.6, 4.1 and 4.5, respectively), it is interesting to notice that the former is comparable with the DCE value and about two orders of magnitude smaller than the

Table 5.5: Comparison between experimental (second column) and theoretical (third and fourth columns) cross sections for the g.s. and first excited transitions for the ^{116}Cd(^{20}Ne, ^{22}Ne)^{114}Cd 2n-pickup reaction at 306 MeV.

Final channel	Experimental cross section (nb)	Theoretical cross section (nb)	
		Direct	Sequential
$^{22}Ne_{g.s.}$ (0+) + $^{114}Cd_{g.s.}$ (0+)	450±200	209	427
$^{22}Ne_{g.s.}$ (0+) + $^{114}Cd_{0.558}$ (2+)	420±190	314	636

single transfer one. Being the two-proton transfer reaction, in particular, very suppressed, one could expect that the 2p-stripping plus 2n-pickup could contribute in small amount to the DCE channel cross section. This achievement would be crucial since two-particle transfer reactions represent the first - in case of the direct transfer - or the two first steps - in the case of sequential processes - of the multi-nucleon transfer reactions that might compete with the DCE reaction. To quantitatively investigate such hypothesis, an in-depth analysis was performed. In particular, the ^{116}Cd(^{20}Ne, ^{22}Ne)^{114}Cd two-neutron pickup reaction channel was also measured in a specific run performed at the same colliding energy and in a similar angular range ($4^\circ < \theta_{lab} < 15^\circ$). The ground and the $^{114}Cd_{0.558}$ first excited states integrated cross sections were experimental extracted[3] resulting also quite suppressed, see Tab. 5.5. Such values were theoretically investigated[4] within the CRC and CCBA frameworks for the direct and sequential mechanisms, respectively, in complete analogy to the described two-proton transfer channel analysis [131]. The obtained results are reported in Tab. 5.5.

The agreement between experimental and theoretical results is reasonable considering the sizable errors affecting the experimental values, due to the limited statistics. The interference effect between the two - direct

[3]Data reduction performed by Dr. A. Hacisalihoglu

[4]Calculations performed by Dr. J. Ferreira.

and sequential - mechanisms has not yet been included in the calculation and will complete the reaction theoretical analysis.
The satisfying theoretical description of the different transfer reaction channels reported in the present Thesis - single and double proton stripping as well as the two-neutron pickup just discussed - has paved the way to a systematic investigation of the complete transfer paths which could contribute to the DCE cross section[5]. The many considered multi-nucleon transfer processes, including also those reaction channels for which there are no experimental data, are shown in Fig. 5.8. The calculations have been performed along the line of those here described, thus distinguishing between simultaneous (2p, 2n) and sequential (p-p, n-n) mechanisms. More details about them can be found in Ref. [132].

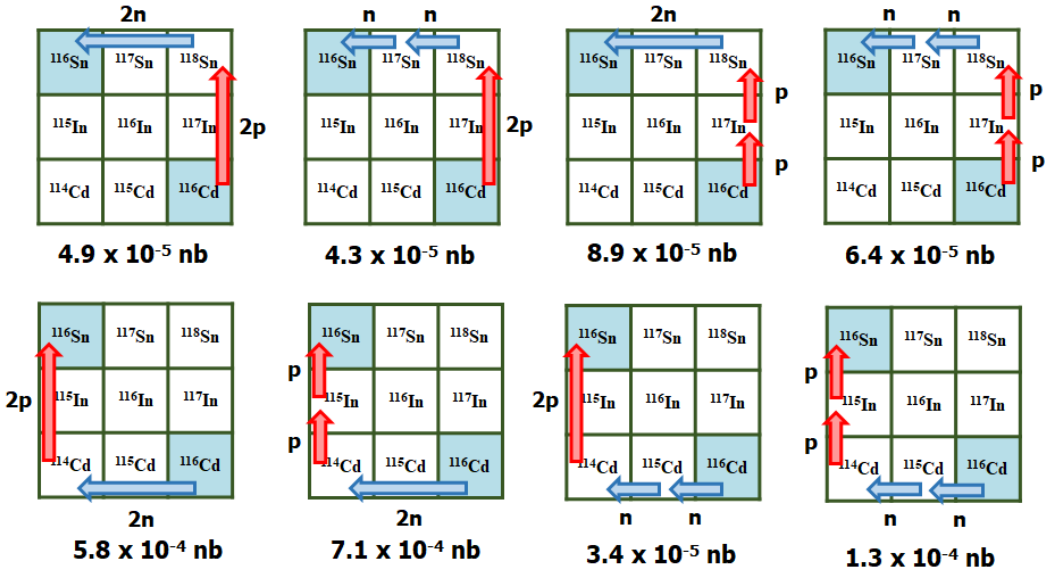

Figure 5.8: Multi-nucleon transfer processes in competition with DCE reaction channel. The values express the calculated cross sections for the g.s. to g.s. transitions integrated in the angular range $3° < \theta_{lab} < 14°$.

[5]Calculations performed by Dr. J. Ferreira.

The values reported in Fig. 5.8 express the integrated ($3^\circ < \theta_{lab} < 14^\circ$) cross sections for the ground state-to-ground state transitions of the different reaction paths. They all are many order of magnitude smaller than the experimental one of the DCE channel, 12.73$\pm$2.37 nb. Thus, even considering the contributions from all the different processes, the DCE cross section value cannot be justified in terms of multi-nucleon transfer mechanisms. As a consequence, one can conclude that DCE reaction between heavy-ions at the investigated energy are sensitive to the genuine direct mechanism dominated by isovector meson exchange. Such clear proof, achieved for the first time in the NUMEN project experimental conditions, represents a milestone on the way of the investigation about the connection between the Double Charge Exchange nuclear reactions and the weak $\beta\beta$ processes.

Conclusions

The ^{20}Ne+^{116}Cd reaction system, investigated in the present Thesis, represents the first case study of heavy-ion Double Charge Exchange (DCE) reaction and its competitive processes for a neutrinoless double beta decay candidate nucleus.
Experimentally, the set of interesting nuclear reactions have been studied for the first time including Double and Single Charge Exchange as well as one- and two-nucleon transfer channels. All the reactions have been measured in the same experimental conditions, thus promoting a comparative approach. The adoption of specific experimental solutions combined with the high performance guaranteed by the MAGNEX spectrometer have proven to be effective in addressing those challenging measurements characterized by very low - down to tens nbarn - absolute cross section values. In particular, the rare and poorly known DCE and two-proton transfer reactions have been measured with enough energy resolution to separate the ground state from the first excited transitions. A sensitivity analysis of the experimental set-up was conceived and applied to the DCE data. The estimated corresponding cross section lower limit confirms the high significance of the extracted experimental values.
Conclusive results on the competition between multi-nucleon Transfer processes and Charge Exchange reactions have been achieved, testing state-of-the-art calculations on the experimental data presented in the Thesis. In particular, from the one-proton transfer process, nicely described in the Coupled Reaction Channels framework adopting shell model spectroscopic amplitudes, the sequential single-proton stripping and single-

neutron pick-up mechanisms have been considered. Comparing their results with the Single Charge Exchange experimental cross section value, a contribution due to the sequential-nucleon transfer mechanism to the SCE cross section of the order of 10% was estimated. Such result, combined with the recently introduced SCE theoretical model, demonstrates that they can be used to extract nuclear structure information, testing in particular the transitions characterized by high momentum transferred.
The very suppressed two-proton transfer data were analyzed considering both the direct and the sequential mechanisms. Combining its result with the two-neutron transfer one and considering several possible transfer paths, the multi-nucleon transfer contribution to the Double Charge Exchange cross section has been extensively evaluated. It has been shown that, under the NUMEN project experimental conditions, transfer cross section contributions to DCE one are expected to be several order of magnitude smaller than the measured values, resulting negligible. As a consequence, the experimental extracted Double Charge Exchange cross section values are due to the genuine meson induced Charge Exchange mechanism whose investigation and possible connection to the weak $\beta\beta$ processes represents the NUMEN project final goal.

Bibliography

[1] M. Goeppert-Mayer, Phys. Rev. **48**, 512 (1935).

[2] A. S. Barabash, Nucl. Phys. **A935**, 52 (2015).

[3] J. Kotila and F. Iachello, Phys. Rev. **C85**, 034316 (2012).

[4] M. F. Kidd, J. H. Esterline, S. W. Finch, and W. Tornow, Phys. Rev. **C90**, 055501 (2014).

[5] W. H. Furry, Phys. Rev. **56**, 1184 (1939).

[6] A. S. Barabash, Front.in Phys. **6**, 160 (2019).

[7] I. Takashi, in *Proceedings of Neutrino 2018 - XXVIII International Conference on Neutrino Physics and Astrophysics* (Zenodo, 2018).

[8] M. Agostini et al., Phys. Rev. Lett. **120**, 132503 (2018).

[9] O. Azzolini et al., Phys. Rev. Lett. **120**, 232502 (2018).

[10] J. Argyriades et al., Nucl. Phys. **A847**, 168 (2010).

[11] R. Arnold et al., Phys. Rev. **D92**, 072011 (2015).

[12] A. S. Barabash et al., Phys. Rev. **D98**, 092007 (2018).

[13] C. Alduino et al., Phys. Rev. Lett. **120**, 132501 (2018).

[14] A. Gando et al., Phys. Rev. Lett. **117**, 082503 (2016), [Addendum: Phys. Rev. Lett.117,no.10,109903(2016)].

[15] R. Arnold et al., Phys. Rev. **D94**, 072003 (2016).

[16] J. D. Vergados, H. Ejiri, and F. Simkovic, Rept. Prog. Phys. **75**, 106301 (2012).

[17] J. Schechter and J. W. F. Valle, Phys. Rev. **D25**, 2951 (1982), [289 (1981)].

[18] P. F. De Salas, S. Gariazzo, O. Mena, C. A. Ternes, and M. Tórtola, Front. Astron. Space Sci. **5**, 36 (2018).

[19] J. Barea, J. Kotila, and F. Iachello, Phys. Rev. **C87**, 014315 (2013).

[20] J. Engel and J. Menéndez, Rept. Prog. Phys. **80**, 046301 (2017).

[21] M. J. Dolinski, A. W. P. Poon, and W. Rodejohann, Annual Review of Nuclear and Particle Science **69**, 219 (2019).

[22] P. Gysbers et al., Nature Phys. **15**, 428 (2019).

[23] S. Dell'Oro, S. Marcocci, M. Viel, and F. Vissani, Adv. High Energy Phys. **2016**, 2162659 (2016).

[24] J. Menendez, A. Poves, E. Caurier, and F. Nowacki, Nucl. Phys. **A818**, 139 (2009).

[25] A. S. Barabash, AIP Conf. Proc. **1894**, 020002 (2017).

[26] F. Šimkovic, V. Rodin, A. Faessler, and P. Vogel, Phys. Rev. C **87**, 045501 (2013).

[27] Y. Iwata, N. Shimizu, T. Otsuka, Y. Utsuno, J. Menéndez, M. Honma, and T. Abe, Phys. Rev. Lett. **116**, 112502 (2016), [Erratum: Phys. Rev. Lett. 117, no. 17, 179902(2016)].

[28] P. K. Rath, Ramesh Chandra, K. Chaturvedi, and P. K. Raina, Frontiers in Physics **7**, 64 (2019).

[29] J. M. Yao, L. S. Song, K. Hagino, P. Ring, and J. Meng, Phys. Rev. C **91**, 024316 (2015).

[30] J. Menéndez, D. Gazit, and A. Schwenk, Phys. Rev. Lett. **107**, 062501 (2011).

[31] F. Šimkovic, G. Pantis, J. D. Vergados, and A. Faessler, Phys. Rev. C **60**, 055502 (1999).

[32] R. A. Sen'kov and M. Horoi, Phys. Rev. **C88**, 064312 (2013).

[33] K. Zuber, in *Consensus report, IPPP Workshop on Matrix Elements for Neutrinoless Double Beta Decay, Durham, England, 23-24 May, 2005* .

[34] V. Rodin, in *Proceedings, International Conference on Nuclear Structure and Related Topics (NSRT), Dubna, Russia, 30 June - 4 July 2009*, edited by A. I. Vdovin, V. V. Voronov, and R. V. Jolos (JINR, Moscow, 2010).

[35] F. Simkovic, M. Nowak, W. A. Kaminski, A. A. Raduta, and Amand Faessler, Phys. Rev. **C64**, 035501 (2001).

[36] J. Suhonen, S.B. Khadkikar, and Amand Faessler, Physics Letters B **237**, 8 (1990).

[37] J. Engel, Journal of Physics G: Nuclear and Particle Physics **42**, 034017 (2015).

[38] D. Navas-Nicolas and P. Sarriguren, Phys. Rev. **C91**, 024317 (2015).

[39] S.J. Freeman and J. P. Schiffer, Journal of Physics G: Nuclear and Particle Physics **39**, 124004 (2012).

[40] J. P. Schiffer et al., Phys. Rev. Lett. **100**, 112501 (2008).

[41] B. P. Kay, AIP Conference Proceedings **1894**, 020013 (2017).

[42] J. Menéndez, A. Poves, E. Caurier, and F. Nowacki, Phys. Rev. C **80**, 048501 (2009).

[43] H. Ejiri, Physics Reports **338**, 265 (2000).

[44] S. D. Bloom, N. K. Glendenning, and S. A. Moszkowski, Phys. Rev. Lett. **3**, 98 (1959).

[45] C. D. Goodman, C. A. Goulding, M. B. Greenfield, J. Rapaport, D. E. Bainum, C. C. Foster, W. G. Love, and F. Petrovich, Phys. Rev. Lett. **44**, 1755 (1980).

[46] T.N. Taddeucci, C.A. Goulding, T.A. Carey, R.C. Byrd, C.D. Goodman, C. Gaarde, J. Larsen, D. Horen, J. Rapaport, and E. Sugarbaker, Nuclear Physics A **469**, 125 (1987).

[47] J. Suhonen and O. Civitarese, Physics Reports **300**, 123 (1998).

[48] V. Rodin, A. Faessler, F. Šimkovic, and P. Vogel, Nuclear Physics A **766**, 107 (2006).

[49] H. Lenske, J. I. Bellone, M. Colonna, and J. A. Lay, Phys. Rev. C **98**, 044620 (2018).

[50] J. Barea, J. Kotila, and F. Iachello, Phys. Rev. Lett. **109**, 042501 (2012).

[51] P. Puppe, D. Frekers, T. Adachi, H. Akimune, N. Aoi, B. Bilgier, H. Ejiri, H. Fujita, Y. Fujita, M. Fujiwara, E. Ganioğlu, M. N. Harakeh, K. Hatanaka, M. Holl, H. C. Kozer, J. Lee, A. Lennarz, H. Matsubara, K. Miki, S. E. A. Orrigo, T. Suzuki, A. Tamii, and J. H. Thies, Phys. Rev. C **84**, 051305 (2011).

[52] I. Navon, M. J. Leitch, D. A. Bryman, T. Numao, P. Schlatter, G. Azuelos, R. Poutissou, R. A. Burnham, M. Hasinoff, J. M. Poutissou, J. A. Macdonald, J. E. Spuller, C. K. Hargrove, H. Mes, M. Blecher, K. Gotow, M. Moinester, and H. Baer, Phys. Rev. Lett. **52**, 105 (1984).

[53] J. N. Knudson, J. R. Comfort, R. A. Gianelli, B. G. Ritchie, D. Rothenberger, D. Poanić, S. S. Hanna, J. D. Bowman, H. W. Baer, A. G. Bergmann, P. A. Heusi, F. Irom, C. J. Seftor, S. Hoibräten, R. A. Loveman, S. H. Rokni, H. Crannell, D. I. Sober, W. J. Fickinger, and H. Marshak, Phys. Rev. C **35**, 1382 (1987).

[54] S. Mordechai, H. T. Fortune, J. M. O'Donnell, G. Liu, M. Burlein, A. H. Wuosmaa, S. Greene, C. L. Morris, N. Auerbach, S. H. Yoo, and C. Fred Moore, Phys. Rev. C **41**, 202 (1990).

[55] N. Auerbach, Nuclear Physics A **527**, 443 (1991).

[56] M. Bleszynski and R. J. Glauber, Phys. Rev. C **36**, 681 (1987).

[57] H. Lenske, F. Cappuzzello, M. Cavallaro, and M. Colonna, Progress in Particle and Nuclear Physics **109**, 103716 (2019).

[58] H. Lenske, J. Phys.: Conf. Ser. **1056**, 012030 (2018).

[59] M. Colonna, J. I. Bellone, S. Burrello, J-A Lay, and H. Lenske, in *Proceedings, 15th International Conference on Nuclear Reaction Mechanisms: Varenna, Italy, June 11-15, 2018*, edited by F. Cerutti, A. Ferrari, T. Kawano, F. Salvat-Pujol, and P. Talou (CERN, Geneva, 2019), Vol. 1, pp. 77–82.

[60] H. Lenske, in *Proceedings, 15th International Conference on Nuclear Reaction Mechanisms: Varenna, Italy, June 11-15, 2018*, edited by F. Cerutti, A. Ferrari, T. Kawano, F. Salvat-Pujol, and P. Talou (CERN, Geneva, 2019), Vol. 1, pp. 49–56.

[61] J. Blomgren, K. Lindh, N. Anantaraman, Sam M. Austin, G.P.A. Berg, B.A. Brown, J.-M. Casandjian, M. Chartier, M.D. Cortina-Gil, S. Fortier, M. Hellström, J.R. Jongman, J.H. Kelley, A. Lepine-Szily, I. Lhenry, M. Mac Cormick, W. Mittig, J. Nilsson, N. Olsson, N.A. Orr, E. Ramakrishman, P. Roussel-Chomaz, B.M. Sherrill, P.-E. Tegnér, J.S. Winfield, and J.A. Winger, Physics Letters B **362**, 34 (1995).

[62] H. Matsubara, M. Takaki, T. Uesaka, S. Shimoura, N. Aoi, M. Dozono, T. Fujii, K. Hatanaka, T. Hashimoto, T. Kawabata, S. Kawase, K. Kisamori, Y. Kikuch, Y. Kubota, C. S. Lee, H. C. Lee, Y. Maeda, S. Michimasa, K. Miki, H. Miya, S. Noji, S. Ota, Satoshi Sakaguchi, Y. Sasamoto, T. Suzuki, L. T. Tang, K. Takahisa, H. Tokieda, A. Tamii, K. Yako, Y. Yasuda, N. Yokota, R. Yokoyama, and J. Zenihiro, Few-Body Systems **54**, 1433 (2013).

[63] M. Takaki et al., in *Proceedings of the Conference on Advances in Radioactive Isotope Science (ARIS2014)*, JPS Conf. Proc. **6**, 020038 (2015).

[64] D. M. Drake, J. D. Moses, J. C. Peng, Nelson Stein, and J. W. Sunier, Phys. Rev. Lett. **45**, 1765 (1980).

[65] C. H. Dasso and A. Vitturi, Phys. Rev. C **34**, 743 (1986).

[66] F. Cappuzzello, M. Cavallaro, C. Agodi, M. Bondí, D. Carbone, A. Cunsolo, and A. Foti, Eur. Phys. J. **A51**, 145 (2015).

[67] D.M. Brink, Physics Letters B **40**, 37 (1972).

[68] T.N. Taddeucci, C.A. Goulding, T.A. Carey, R.C. Byrd, C.D. Goodman, C. Gaarde, J. Larsen, D. Horen, J. Rapaport, and E. Sugarbaker, Nuclear Physics A **469**, 125 (1987).

[69] N. L. Vaquero, T. R. Rodríguez, and J. L. Egido, Phys. Rev. Lett. **111**, 142501 (2013).

[70] N. Shimizu, J. Menéndez, and K. Yako, Phys. Rev. Lett. **120**, 142502 (2018).

[71] E. Santopinto, H. García-Tecocoatzi, R. I. Magaña Vsevolodovna, and J. Ferretti, Phys. Rev. C **98**, 061601 (2018).

[72] D. Rifuggiato, L. Calabretta, and G. Cuttone, in *Proceedings of the XVII internatinal conference on cyclotrons and their applications*, edited by G. Akira and Yasushige Y. (Part. Accel. Soc. Japan, Tokyo, 2004).

[73] D. G. Bongiovanni et al., J. Phys. Conf. Ser. **1056**, 012007 (2018).

[74] D. Lo Presti et al., J. Phys. Conf. Ser. **1056**, 012034 (2018).

[75] D. Bonanno, D. Lo Presti, D. Bongiovanni, G. Gallo, F. Longhitano, S. Reito, and Reito, J. Phys. Conf. Ser. **1056**, 012006 (2018).

[76] A. D. Russo, L. Calabretta, A. Calanna, G. D'Agostino, D. Rifuggiato, and Rifuggiato, J. Phys. Conf. Ser. **1056**, 012051 (2018).

[77] F. Pinna, F. Iazzi, R. Introzzi, D. Calvo, M. Fisichella, and Fisichella, J. Phys. Conf. Ser. **1056**, 012046 (2018).

[78] F. Iazzi, S. Ferrero, R. Introzzi, F. Pinna, L. Scaltrito, D. Calvo, M. Fisichella, C. Agodi, F. Cappuzzello, D. Carbone, and M. Cavallaro, WIT Transactions on Engineering Sciences **116**, 61 (2017).

[79] F. Cappuzzello et al., Eur. Phys. J. A **54**, 72 (2018).

[80] D.R. Tilley, C.M. Cheves, J.H. Kelley, S. Raman, and H.R. Weller, Nuclear Physics A **636**, 1 (1998).

[81] B. W. Pointon, O. Häusser, R. Henderson, A. Celler, K. Hicks, K. P. Jackson, R. Jeppesen, B. Larson, J. Mildenberger, A. Trudel, M. Vetterli, and S. Yen, Phys. Rev. C **44**, 2430 (1991).

[82] A. Spatafora, F. Cappuzzello, D. Carbone, M. Cavallaro, J. A. Lay, L. Acosta, C. Agodi, D. Bonanno, D. Bongiovanni, I. Boztosun, G. A. Brischetto, S. Burrello, S. Calabrese, D. Calvo, E. R. Chávez Lomelí, I. Ciraldo, M. Colonna, F. Delaunay, N. Deshmukh, J. L. Ferreira, P. Finocchiaro, M. Fisichella, A. Foti, G. Gallo, A. Hacisalihoglu, F. Iazzi, G. Lanzalone, H. Lenske, R. Linares, D. Lo Presti, J. Lubian, M. Moralles, A. Muoio, J. R. B. Oliveira, A. Pakou, L. Pandola, H. Petrascu, F. Pinna, S. Reito, G. Russo, G. Santagati, O. Sgouros, S. O. Solakci, V. Soukeras, G. Souliotis, D. Torresi, S. Tudisco, A. Yildirim, and V. A. B. Zagatto, Phys. Rev. C **100**, 034620 (2019).

[83] H. Akimune, H. Ejiri, M. Fujiwara, I. Daito, T. Inomata, R. Hazama, A. Tamii, H. Toyokawa, and M. Yosoi, Physics Letters B **394**, 23 (1997).

[84] J. H. Thies, D. Frekers, T. Adachi, M. Dozono, H. Ejiri, H. Fujita, Y. Fujita, M. Fujiwara, E.-W. Grewe, K. Hatanaka, P. Heinrichs, D. Ishikawa, N. T. Khai, A. Lennarz, H. Matsubara, H. Okamura, Y. Y. Oo, P. Puppe, T. Ruhe, K. Suda, A. Tamii, H. P. Yoshida, and R. G. T. Zegers, Phys. Rev. C **86**, 014304 (2012).

[85] S. Rakers, C. Bäumer, A. M. van den Berg, B. Davids, D. Frekers, D. De Frenne, E.-W. Grewe, P. Haefner, M. N. Harakeh, S. Hollstein,

M. Hunyadi, E. Jacobs, B. C. Junk, A. Korff, A. Negret, L. Popescu, and H. J. Wörtche, Phys. Rev. C **71**, 054313 (2005).

[86] M. Sasano, H. Sakai, K. Yako, T. Wakasa, M. Dozono, V. Rodin, A. Faessler, K. Fujita, M. B. Greenfield, K. Hatanaka, K. Itoh, T. Kawabata, H. Kuboki, Y. Maeda, K. Miki, K. Muto, S. Noji, H. Okamura, Y. Sakemi, K. Sekiguchi, Y. Shimizu, Y. Sasamoto, Y. Tameshige, A. Tamii, and T. Uesaka, Phys. Rev. C **85**, 061301 (2012).

[87] P. Sarriguren, O. Moreno, and E. Moya De Guerra, Adv. High Energy Phys. **2016**, 6391052 (2016).

[88] F. Cappuzzello, C. Agodi, M. Bondì, D. Carbone, M. Cavallaro, A. Cunsolo, M. De Napoli, A. Foti, D. Nicolosi, S. Tropea, P.N. de Faria, R. Linares, J.R.B. Oliveira, and M.R.D. Rodrigues, Nuclear Instruments and Methods in Physics Research Section A: Accelerators, Spectrometers, Detectors and Associated Equipment **763**, 314 (2014).

[89] D. Rifuggiato, L. Calabretta, L. Cosentino, and G. Cuttone, in *20th International Conference on Cyclotrons and their Applications (CYCLOTRONS 2013): Vancouver, Canada, 16-20 September 2013*, edited by V. Schaa, S. Waller, and J. Chrin (Curran Associates, Red Hook, 2014).

[90] K. Shima, N. Kuno, M. Yamanouchi, and H. Tawara, Atomic Data and Nuclear Data Tables **51**, 173 (1992).

[91] M. Cavallaro et al., Res. in Phys. **13**, 102191 (2019).

[92] F. Cappuzzello, C. Agodi, D. Carbone, and M. Cavallaro, Eur. Phys. J. **A52**, 167 (2016).

[93] D. Pereira, J. Lubian, J. R. B. Oliveira, D. P. de Sousa, and L. C. Chamon, Phys. Lett. B **670**, 330 (2009).

[94] M. Cavallaro et al., Phys. Rev. **C93**, 064323 (2016).

[95] D. Carbone, J. L. Ferreira, F. Cappuzzello, J. Lubian, C. Agodi, M. Cavallaro, A. Foti, A. Gargano, S. M. Lenzi, R. Linares, and G. Santagati, Phys. Rev. C **95**, 034603 (2017).

[96] B. Paes, G. Santagati, R. Magana Vsevolodovna, F. Cappuzzello, D. Carbone, E. N. Cardozo, M. Cavallaro, H. García-Tecocoatzi, A. Gargano, J. L. Ferreira, S. M. Lenzi, R. Linares, E. Santopinto, A. Vitturi, and J. Lubian, Phys. Rev. C **96**, 044612 (2017).

[97] V. Soukeras, A. Pakou, F. Cappuzzello, L. Acosta, C. Agodi, N. Alamanos, M. Bondi, D. Carbone, M. Cavallaro, A. Cunsolo, M. De Napoli, A. Di Pietro, J. P. Fernández-García, P. Figuera, M. Fisichella, A. Foti, N. Keeley, G. Marquinez-Duran, I. Martel, M. Mazzocco, D. Nicolosi, D. Pierroutsakou, K. Rusek, O. Sgouros, E. Stiliaris, E. Strano, and D. Torresi, Phys. Rev. C **91**, 057601 (2015).

[98] F. Cappuzzello, D. Carbone, M. Cavallaro, M. Bondì, C. Agodi, F. Azaiez, A. Bonaccorso, A. Cunsolo, L. Fortunato, A. Foti, S. Franchoo, E. Khan, R. Linares, J. Lubian, J. A. Scarpaci, and A. Vitturi, Nature Communications **6**, 6743 (2015).

[99] A. Cunsolo, F. Cappuzzello, A. Foti, A. Lazzaro, A.L. Melita, C. Nociforo, V. Shchepunov, and J.S. Winfield, Nuclear Instruments and Methods in Physics Research Section A: Accelerators, Spectrometers, Detectors and Associated Equipment **484**, 56 (2002).

[100] K. Makino and M. Berz, COSY INFINITY Version 8.1, 2001, `http://cosy.pa.msu.edu`.

[101] F. Cappuzzello, D. Carbone, and M. Cavallaro, Nucl. Instrum. Methods Phys. Res. A **638**, 74 (2011).

[102] A. Lazzaro, F. Cappuzzello, A. Cunsolo, M. Cavallaro, A. Foti, A. Khouaja, S.E.A. Orrigo, and J.S. Winfield, Nuclear Instruments and Methods in Physics Research Section A: Accelerators, Spectrometers, Detectors and Associated Equipment **570**, 192 (2007).

[103] A. Lazzaro, F. Cappuzzello, A. Cunsolo, M. Cavallaro, A. Foti, S.E.A. Orrigo, M.R.D. Rodrigues, and J.S. Winfield, Nuclear In-

struments and Methods in Physics Research Section A: Accelerators, Spectrometers, Detectors and Associated Equipment **585**, 136 (2008).

[104] A. Lazzaro, F. Cappuzzello, A. Cunsolo, M. Cavallaro, A. Foti, S.E.A. Orrigo, M.R.D. Rodrigues, and J.S. Winfield, Nuclear Instruments and Methods in Physics Research Section A: Accelerators, Spectrometers, Detectors and Associated Equipment **591**, 394 (2008).

[105] A. Lazzaro, F. Cappuzzello, A. Cunsolo, M. Cavallaro, A. Foti, S.E.A. Orrigo, M.R.D. Rodrigues, J.S. Winfield, and M. Berz, Nuclear Instruments and Methods in Physics Research Section A: Accelerators, Spectrometers, Detectors and Associated Equipment **602**, 494 (2009).

[106] K. Makino and M. Berz, Nuclear Instruments and Methods in Physics Research Section A: Accelerators, Spectrometers, Detectors and Associated Equipment **427**, 338 (1999).

[107] C. Boiano, R. Bassini, A. Pullia, and A. Pagano, IEEE Transactions on Nuclear Science **51**, 1931 (2004).

[108] M. Bordessoule, F. Bartol, M. Lemonnier, and J.-C. Santiard, Nuclear Instruments and Methods in Physics Research Section A: Accelerators, Spectrometers, Detectors and Associated Equipment **390**, 79 (1997).

[109] C. Boiano, F. Cappuzzello, M. Cavallaro, A. Cunsolo, A. Foti, P. Guazzoni, S. Moser, S. E. A. Orrigo, F. Riccio, M. R. D. Rodrigues, J. S. Winfield, and L. Zetta, IEEE Transactions on Nuclear Science **55**, 3563 (2008).

[110] D. Carbone, F. Cappuzzello, and M. Cavallaro, Eur. Phys. J. **A48**, 60 (2012).

[111] F. Cappuzzello et al., Nucl. Instrum. Methods Phys. Res. A **621**, 419 (2010).

[112] D. Carbone, Eur. Phys. J. Plus **130**, 143 (2015).

[113] O.B. Tarasov and D. Bazin, Nuclear Instruments and Methods in Physics Research Section B: Beam Interactions with Materials and Atoms **266**, 4657 (2008), http://lise.nscl.msu.edu/lise.html.

[114] J. F. Ziegler, M. D. Ziegler, and J. P. Biersack, Nuclear Instruments and Methods in Physics Research B **268**, 1818 (2010).

[115] M. Cavallaro et al., Nucl. Instrum. Methods Phys. Res. A **637**, 77 (2011).

[116] R.O. Akyuz and A. Winther, in *Proc. Enrico Fermi Int. School of Physics*, edited by R.A. Broglia, Dasso C.H., and R. Ricci (North-Holland, Amsterdam, 1979).

[117] G.R. Satchler and W.G. Love, Phys. Rep. **55**, 183 (1979).

[118] M.E. Brandan and G.R. Satchler, Physics Reports **285**, 143 (1997).

[119] L.C. Chamon, Nuclear Physics A **787**, 198 (2007).

[120] Brown A., NuShellX for Windows and Linux, http:/www.garsington.eclipse.co.uk.

[121] A. P. Zuker, B. Buck, and J. B. McGrory, Phys. Rev. Lett. **21**, 39 (1968).

[122] L. Coraggio, A. Gargano, and N. Itaco, Phys. Rev. C **93**, 064328 (2016).

[123] W. R. Wharton and P. T. Debevec, Phys. Rev. C **11**, 1963 (1975).

[124] H. Lenske, H. H. Wolter, and H. G. Bohlen, Phys. Rev. Lett. **62**, 1457 (1989).

[125] J. S. Winfield, N. Anantaraman, Sam M. Austin, L. H. Harwood, J. van der Plicht, H.-L. Wu, and A. F. Zeller, Phys. Rev. C **33**, 1333 (1986).

[126] S. Nakayama, T. Yamagata, K. Yuasa, M. Tanaka, M. Inoue, T. Itahashi, and H. Ogata, Physics Letters B **246**, 342 (1990).

[127] L.K. Fifield, W.N. Catford, N.A. Orr, T.R. Ophel, A. Etchegoyen, and M.C. Etchegoyen, Nuclear Physics A **552**, 125 (1993).

[128] S. Burrello, S. Calabrese, et al., In preparation .

[129] M. Hjorth-Jensen, T.T.S. Kuo, and E. Osnes, Physics Reports **261**, 125 (1995).

[130] R. Machleidt, Phys. Rev. C **63**, 024001 (2001).

[131] J. Ferreira et al., In preparation .

[132] J. Ferreira, PhD Thesis, Instituto de Física, Universidade Federal Fluminense (2019).

Acknowledgements

My first thanks go to Prof. Francesco Cappuzzello, for having introduced me, with confidence, into the intriguing world of Nuclear Physics and for having represented a true and tangible example of passionate professionalism and fairness.
To Dr. Diana Carbone and Dr. Manuela Cavallaro, for having assisted me with great care, patience and generosity, supporting me and constantly encouraging me to improve.
To Dr. Titti Agodi, Dr. Domenico Torresi and Dr. Alessandro Spatafora for the always stimulating and amusing discussions.
To all the members of the NUMEN collaboration and in particular to Dr. Akis Sgouros, Dr. Vasilis Soukeras, Dr. Paolo Finocchiaro, Dr. Stefano Burrello, Dr. Jessica Bellone and Dr. Jonas Ferreira for the pleasant time spent working together.
To all the colleagues of the PhD course and in particular to Daniele Lanteri and Leonard Re for having shared successes and frustrations together.
To the Laboratori Nazionali del Sud, for the excellent and concrete effort made in research in Physics and for having made me part of it.
To the Department of Physics and Astronomy "Ettore Majorana" and in particular to the Vice-Director Prof. Giuseppe Angilella, for the commendable commitment to support new generations of Physicists.